

UNIVERSITY OF CALGARY

Investigation On A Hertzian Dipole Antenna Above An Artificial Impedance
Surface

by

Mi Zhou

A THESIS

SUBMITTED TO THE FACULTY OF GRADUATE STUDIES
IN PARTIAL FULFILLMENT OF THE REQUIREMENTS FOR THE
DEGREE OF MASTER OF SCIENCE

DEPARTMENT OF ELECTRICAL AND COMPUTER ENGINEERING

CALGARY, ALBERTA

March, 2008

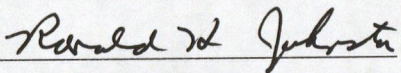
© Mi Zhou 2008

UNIVERSITY OF CALGARY
FACULTY OF GRADUATE STUDIES

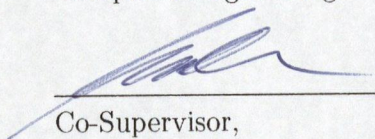
The undersigned certify that they have read, and recommend to the Faculty of Graduate Studies for acceptance, a thesis entitled "Investigation On A Hertzian Dipole Antenna Above An Artificial Impedance Surface" submitted by Mi Zhou in partial fulfillment of the requirements for the degree of MASTER OF SCIENCE.



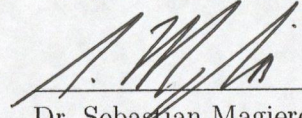
Supervisor, Dr. Michael Potter
Department of Electrical and
Computer Engineering



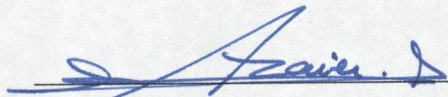
Dr. Ronald Johnston
Department of Electrical and
Computer Engineering



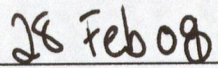
Co-Supervisor,
Dr. Michal Okoniewski
Department of Electrical and
Computer Engineering



Dr. Sebastian Magierowski
Department of Electrical and
Computer Engineering



Dr. Jalel Azaiez
Department of Chemical and
Petroleum Engineering



Date

Abstract

Artificial Impedance Surfaces (AIS) are attractive because they allow antennas to be placed much closer to them than to traditional electric conductors. Plane wave reflection coefficients of the AIS were used extensively to aid with antenna designs above them. However, it was not well-understood how these reflection coefficients translate to antenna radiation properties above them. In this thesis, a far-field model is developed for a Hertzian dipole above an AIS. This model makes a simple but clear connection between the far-field patterns of the dipole and the AIS reflection coefficients. It is shown that, with accurate reflection coefficients, the far-field patterns can be computed accurately and efficiently. In order to shorten computation time more, a constant grid impedance model is used to compute the AIS plane wave reflection coefficients. It is shown that the reflection coefficients can be computed accurately using this model. Errors of this model are also analyzed.

Acknowledgements

I would like to express my sincere gratitude and acknowledgement to my supervisors, Dr. Mike Potter and Dr. Michal Okoniewski, for providing guidance and advice. Throughout the course of my graduate studies, I have learned a great deal from them. Without their lead and patience, the project could not have been completed this smoothly.

I would also like to thank Adrian Sutinjo. As my research colleague, he has offered me a great deal of knowledge and instructions for this project.

I thank the members of my examining committee including Dr. Ronald Johnston, Dr. Sebastian Magierowski and Dr. Jalel Azaiez.

In addition, I extend my appreciation to Rob Salmond and Qiao Wei for their suggestions on this thesis. I would also like to thank all my friends for their generous support.

Finally and most importantly, I would like to thank my mom and grandma for their constant support and encouragement. Without their help, I would not have achieved where I am today.

Table of Contents

Approval Page	ii
Abstract	iii
Acknowledgements	iv
Table of Contents	v
List of Tables	vii
List of Figures	xii
List of Acronyms and Symbols	xiii
1 Introduction	1
1.1 Motivation	1
1.2 Objectives	3
1.3 Thesis Outline	4
2 Background and Literature Review	6
2.1 Electric Conductors as Antenna Reflectors	6
2.2 Mushroom Structures as Antenna Reflectors	8
2.3 Artificial Impedance Surfaces	9
2.3.1 Antenna Designs over AIS Structures	11
2.3.2 Far-Field Models for Antennas above an AIS	13
2.3.3 Circuit Models for AIS	14
2.4 Summary	16
3 Far-Field Modeling of a Dipole Antenna above an Artificial Impedance Surface	18
3.1 The Method of Modal Expansion	18
3.2 The Transmitting Method	22
3.2.1 H-Plane Pattern	23
3.2.2 E-Plane Pattern	27
3.2.3 Far-field Pattern Equations Summary	31
3.3 Receiving Method	31
3.3.1 Reciprocity for Antennas	32
3.3.2 H-Plane Pattern	33
3.3.3 E-Plane Pattern	35
3.3.4 Far-field Model	37
3.4 Pattern Comparison	38
3.4.1 AIS Selection	38
3.4.2 Obtaining Reflection Coefficients for the Far-field Computation	39

3.4.3	Full-wave Simulation Setup	40
3.4.4	Pattern Comparison Results	42
3.4.5	Model Error Analysis	51
3.5	Summary	53
4	Grid Impedance Modeling	56
4.1	The Constant Grid Impedance Model	57
4.1.1	Grid Impedance Test	59
4.1.2	Reflection Coefficient Test	64
4.1.3	Constant Grid Impedance Model Summary	67
4.2	Reflection Phase Error Analysis	70
4.2.1	Error Analysis for the Constant Grid Impedance Model	70
4.2.2	Circuit Model Sensitivity Analysis	72
4.2.3	Reflection Phase Error Analysis Summary	75
4.3	Circuit Model Analysis	76
4.3.1	Frequency Location of the Maximum $\angle\Gamma$ Error	76
4.3.2	$\angle\Gamma$ Error Characteristic for TE and TM Incidence	78
4.3.3	Decreasing $\Gamma^{TE}(\theta)$ Error at AIS Resonance	79
4.3.4	Circuit Model Analysis Summary	81
4.4	Modified Constant Z_g Model for Patch AIS	81
4.4.1	Model Description	81
4.4.2	Model Verification	83
4.4.3	Model Application	84
4.5	Summary	91
5	Conclusion and Future Work	93
5.1	Conclusion and Thesis Contribution	93
5.2	Future Work	95
	Bibliography	97
A	The Steepest Decent Method	102

List of Tables

0.1	Acronyms Used in This Thesis	xiii
0.2	Common Symbols Used in This Thesis	xiii
3.1	HPBW comparison between model and simulation for the patch AIS with 10 X 10 patch array.	45
3.2	HPBW comparison between model and simulation for the Jerusalem cross AIS with 12 X 12 array.	45
3.3	HPBW comparison for the H-plane between model and simulation for the patch AIS with different array size.	52
4.1	Maximum Z_g^{Error} over Incident Angles for the Patch AIS	71
4.2	Maximum Z_g^{Error} over Incident Angles for the Jerusalem Cross AIS	71
4.3	Comparing the Constant Z_g Model and the modified Z_g Model (Maximum Z_g^{Error} over incident angles for the Patch AIS)	84
4.4	Comparing the Modified Z_g Model and the HFSS simulation results (Maximum Z_g^{Error} over incident angles for the Patch AIS with 6.3 mm patch size)	88
4.5	Comparing the Modified Z_g Model and the HFSS simulation results (Maximum Z_g^{Error} over incident angles for the Patch AIS with 6.6 mm patch size)	89
4.6	Comparing the Modified Z_g Model and the HFSS simulation results (Maximum Z_g^{Error} over incident angles for the Patch AIS with 6.9 mm patch size)	90

List of Figures

2.1	An antenna is placed close to an electric conductor. The image current cancels the antenna current out. λ is the wavelength.	7
2.2	An antenna lying $\lambda/4$ away from an electric conductor. The image current adds constructively to the antenna current. λ is the wavelength.	7
2.3	Surface waves propagate along the surface of an electric conductor and radiate at its edge.	8
2.4	Top view and side view of the mushroom structure.	8
2.5	Plane wave reflection phase of a mushroom structure at normal incidence as a function of frequency.	10
2.6	Top and side view of a patch AIS.	10
2.7	Top and side view of a Jerusalem cross AIS.	11
2.8	0° reflection phase of an AIS structure shifts in frequency at different incident angles [1].	12
2.9	Reflection phase of a stable AIS at different incident angles [1].	13
2.10	Equivalent LC parallel circuit model for the mushroom structure.	15
2.11	Equivalent LC parallel circuit model for the AIS structure.	15
2.12	Equivalent transmission line circuit for Z_{in} computation. Z_d and k_d are the characteristic impedance and wave number of the equivalent transmission line. d is the thickness of the AIS dielectric slab. 'Short' represents the electric conductor on the bottom of the AIS structure.	15
3.1	A cylindrical waveguide consisting of a homogeneous isotropic dielectric material bounded by a perfect electric conductor. S is the cross section surface area. C is the boundary curve of the cross section. n is the direction normal to the boundary curve C . σ is the conductivity.	19
3.2	Cylindrical waveguide equivalence for a Hertzian dipole above an AIS.	20
3.3	An Hertzian dipole above an AIS.	23
3.4	Equivalent network for H-plane of a Hertzian dipole over an AIS surface which is modeled as an impedance surface. i_1^{TE} is an electric current source at $z = h$. Z_s is the impedance of the AIS surface. Z_{0l}^{TE} is the characteristic impedance of the equivalent transmission line of TE modes. $k_{zl} = \sqrt{k_0^2 - k_{xl}^2}$	25
3.5	Equivalent modal network for the E-plane of the Hertzian dipole above an AIS surface. Z_s is the equivalent impedance of the AIS; $Z_{0l}^{TM} = k_{zl}/\omega\epsilon_0$ is the characteristic impedance of the equivalent transmission line of TM mode, and $k_{zl} = \sqrt{k_0^2 - k_{yl}^2}$	29
3.6	Illustration of the principle of reciprocity for antennas.	32
3.7	Applying reciprocity to Hertzian dipole above an AIS surface.	33
3.8	The H-plane pattern can be calculated from the transverse electric field near the AIS when the surface is incident by a TE plane wave.	34

3.9	Equivalent transmission line network for the H-plane of the Hertzian dipole over an AIS. Z_s is the equivalent impedance of the AIS. The characteristic impedance of the transmission line is $Z_0^{TE} = Z_0 \cos \theta$. $Z_0 = \sqrt{\mu_0/\epsilon_0}$ is the intrinsic impedance of free space. $k_z = k_0 \cos \theta$ is the wave number in z direction.	35
3.10	The E-plane pattern can be calculated from the transverse electric field near the AIS when the surface is incident by a TM plane wave.	36
3.11	Equivalent network for the E-plane of the Hertzian dipole over an AIS. . .	36
3.12	The dimensions of the Patch and Jerusalem cross unit cell. (a) $a = 7$ mm, $b = 6$ mm. (b) $a = 5.8$ mm, $b = 5.4$ mm, $h = 0.4$ mm, $w = 0.4$ mm, $d = 2.6$ mm. For both AIS, the dielectric thickness is $d = 3$ mm, and the relative permittivity is $\epsilon = 2.2$. [2]	39
3.13	Simulation setup in Ansoft HFSS for $\Gamma(\theta)$ calculation of the AIS surfaces. .	40
3.14	Top view of the FEKO simulation setup for a patch AIS with 10 X 10 patch array.	41
3.15	Far-field pattern comparison between the far-field model and FEKO simulation of a Hertzian dipole over a Patch AIS (10 X 10 array) at 4 GHz. . . .	43
3.16	Far-field pattern comparison between the far-field model and FEKO simulation of a Hertzian dipole over a Patch AIS (10 X 10 array) at 5.5 GHz. . .	43
3.17	Far-field pattern comparison between the far-field model and FEKO simulation of a Hertzian dipole over a Patch AIS (10 X 10 array) at 7.7 GHz. . .	43
3.18	Far-field pattern comparison between the far-field model and FEKO simulation of a Hertzian dipole over a Jerusalem cross AIS (12 X 12 array) at 4 GHz.	44
3.19	Far-field pattern comparison between the far-field model and FEKO simulation of a Hertzian dipole over a Jerusalem cross AIS (12 X 12 array) at 5.5 GHz.	44
3.20	Far-field pattern comparison between the far-field model and FEKO simulation of a Hertzian dipole over a Jerusalem cross AIS (12 X 12 array) at 7.7 GHz.	45
3.21	Comparison of the far-field patterns computed from our far-field model and the constant Γ model with FEKO simulation results for a Hertzian dipole above a patch AIS (10 X 10 array) at 4 GHz.	46
3.22	Comparison of the far-field patterns computed from our far-field model and the constant Γ model with FEKO simulation results for a Hertzian dipole above a patch AIS (10 X 10 array) at 5.5 GHz.	46
3.23	Comparison of the far-field patterns computed from our far-field model and the constant Γ model with FEKO simulation results for a Hertzian dipole above a patch AIS (10 X 10 array) at 7.7 GHz.	47
3.24	Comparison of the far-field patterns computed from our far-field model and the constant Γ model with FEKO simulation results for a Hertzian dipole above a Jerusalem cross AIS (12 X 12 array) at 4 GHz.	47
3.25	Comparison of the far-field patterns computed from our far-field model and the constant Γ model with FEKO simulation results for a Hertzian dipole above a Jerusalem cross AIS (12 X 12 array) at 5.5 GHz.	48

3.26	Comparison of the far-field patterns computed from our far-field model and the constant Γ model with FEKO simulation results for a Hertzian dipole above a Jerusalem cross AIS (12 X 12 array) at 7.7 GHz.	48
3.27	Comparison of the H-plane far-field patterns computed from our far-field model and the constant Z_s model [3] with FEKO simulation results for a Hertzian dipole above a patch AIS (10 X 10 array) and above a Jerusalem cross AIS (12 X 12 array) at 4 GHz.	49
3.28	Comparison of the H-plane far-field patterns computed from our far-field model and the constant Z_s model [3] with FEKO simulation results for a Hertzian dipole above a patch AIS (10 X 10 array) and above a Jerusalem cross AIS (12 X 12 array) at 5.5 GHz.	50
3.29	Comparison of the H-plane far-field patterns computed from our far-field model and the constant Z_s model [3] with FEKO simulation results for a Hertzian dipole above a patch AIS (10 X 10 array) and above a Jerusalem cross AIS (12 X 12 array) at 7.7 GHz.	50
3.30	Far-field pattern comparison between the far-field model and FEKO simulation of a Hertzian dipole over a Patch AIS (10 X 10 array) at 7.7 GHz. . .	53
3.31	Far-field pattern comparison between the far-field model and FEKO simulation of a Hertzian dipole over a patch AIS (14 X 14 patch array) at 7.7 GHz.	53
3.32	Far-field pattern comparison between the far-field model and FEKO simulation of a Hertzian dipole over a patch AIS (18 X 18 patch array) at 7.7 GHz.	54
3.33	Far-field pattern comparison between the far-field model and FEKO simulation of a Hertzian dipole over a patch AIS (20 X 20 patch array) at 7.7 GHz.	54
4.1	The circuit model for an AIS structure.	58
4.2	The dimensions of a single patch and Jerusalem cross unit cell. (a) patch: $a = 7$ mm, $b = 6$ mm. (b) Jerusalem cross: $a = 5.8$ mm, $b = 5.4$ mm, $h = 0.4$ mm, $w = 0.4$ mm, $d = 2.6$ mm.	60
4.3	HFSS simulation setup for grid impedance calculation at normal incidence.	61
4.4	HFSS simulation setup for grid impedance calculation at oblique incidence.	63
4.5	$Z_g(\theta)$ comparison of the constant grid impedance model, the $\cos^2 \theta$ model with HFSS simulation results as benchmark for the patch AIS at 4 GHz. .	64
4.6	$Z_g(\theta)$ comparison of the constant grid impedance model, the $\cos^2 \theta$ model with HFSS simulation results as benchmark for the patch AIS at 5.5 GHz.	64
4.7	$Z_g(\theta)$ comparison of the constant grid impedance model, the $\cos^2 \theta$ model with HFSS simulation results as benchmark for the patch AIS at 7.7 GHz.	65
4.8	$Z_g(\theta)$ comparison of the constant grid impedance model, the $\cos^2 \theta$ model with HFSS simulation results as benchmark for the Jerusalem cross AIS at 4 GHz.	65
4.9	$Z_g(\theta)$ comparison of the constant grid impedance model, the $\cos^2 \theta$ model with HFSS simulation results as benchmark for the Jerusalem cross AIS at 5.5 GHz.	65
4.10	$Z_g(\theta)$ comparison of the constant grid impedance model, the $\cos^2 \theta$ model with HFSS simulation results as benchmark for the Jerusalem cross AIS at 7.7 GHz.	66

4.11 Comparison of reflection phase, $\angle\Gamma(\theta)$, calculated with the constant grid impedance model and simulated in HFSS for the patch AIS at 4 GHz. . .	66
4.12 Comparison of reflection phase, $\angle\Gamma(\theta)$, calculated with the constant grid impedance model and simulated in HFSS for the patch AIS at 5.5 GHz. .	67
4.13 Comparison of reflection phase, $\angle\Gamma(\theta)$, calculated with the constant grid impedance model and simulated in HFSS for the patch AIS at 7.7 GHz. .	68
4.14 Comparison of reflection phase, $\angle\Gamma(\theta)$, calculated with the constant grid impedance model and simulated in HFSS for the Jerusalem cross AIS at 4 GHz.	68
4.15 Comparison of reflection phase, $\angle\Gamma(\theta)$, calculated with the constant grid impedance model and simulated in HFSS for the Jerusalem cross AIS at 5.5 GHz.	69
4.16 Comparison of reflection phase, $\angle\Gamma(\theta)$, calculated with the constant grid impedance model and simulated in HFSS for the Jerusalem cross AIS at 7.7 GHz.	69
4.17 Reflection phase error caused by grid impedance error for the patch AIS with incident angle $\theta = 0^\circ$ and grid impedance error $\Delta Z_g(\theta) = 30\%Z_g^{HFSS, Patch}(0)$.	72
4.18 Reflection phase error caused by grid impedance error for the patch AIS with incident angle $\theta = 40^\circ$ and grid impedance error $\Delta Z_g(\theta) = 30\%Z_g^{HFSS, Patch}(0)$.	73
4.19 Reflection phase error caused by grid impedance error for the patch AIS with incident angle $\theta = 70^\circ$ and grid impedance error $\Delta Z_g(\theta) = 30\%Z_g^{HFSS, Patch}(0)$.	73
4.20 H-plane far-field Pattern comparisons for a Hertzian dipole over two Patch AIS at 7.7GHz. (a) Original patch AIS: dielectric thickness, 3 mm; patch size, 6 mm. (b) New patch AIS: dielectric thickness, 6 mm; patch size, 3 mm. Both AIS resonate at 7.7GHz.	80
4.21 Patch AIS grid Impedance comparison between the HFSS simulation, the constant grid impedance model, and the modified grid impedance model at 7.7 GHz for the TE incidence.	82
4.22 Patch AIS reflection phase comparison between the HFSS simulation, the constant grid impedance model, and the modified grid impedance model at 7.7 GHz for the TE incidence.	83
4.23 Patch AIS grid impedance comparison between the HFSS simulation, the constant grid impedance model, and the modified grid impedance model at 4 GHz for the TE incidence.	84
4.24 Patch AIS reflection phase comparison between the HFSS simulation, the constant grid impedance model, and the modified grid impedance model at 4 GHz for the TE incidence.	85
4.25 Patch AIS grid impedance comparison between the HFSS simulation, the constant grid impedance model, and the modified grid impedance model at 5.5 GHz for the TE incidence.	85
4.26 Patch AIS reflection phase comparison between the HFSS simulation, the constant grid impedance model, and the modified grid impedance model at 5.5 GHz for the TE incidence.	86

4.27	$Z_g(\theta)$ comparison of modified constant grid impedance model with HFSS simulation results as benchmark for a patch AIS at 4 GHz. The dimensions of the single patch is 6.3 mm X 6.3 mm.	87
4.28	$Z_g(\theta)$ comparison of modified constant grid impedance model with HFSS simulation results as benchmark for a patch AIS at 5.5 GHz. The dimensions of the single patch is 6.3 mm X 6.3 mm.	87
4.29	$Z_g(\theta)$ comparison of modified constant grid impedance model with HFSS simulation results as benchmark for a patch AIS at 7.7 GHz. The dimensions of the single patch is 6.3 mm X 6.3 mm.	88
4.30	$Z_g(\theta)$ comparison of modified constant grid impedance model with HFSS simulation results as benchmark for a patch AIS at 4 GHz. The dimensions of the single patch is 6.6 mm X 6.6 mm.	88
4.31	$Z_g(\theta)$ comparison of modified constant grid impedance model with HFSS simulation results as benchmark for a patch AIS at 5.5 GHz. The dimensions of the single patch is 6.6 mm X 6.6 mm.	89
4.32	$Z_g(\theta)$ comparison of modified constant grid impedance model with HFSS simulation results as benchmark for a patch AIS at 7.7 GHz. The dimensions of the single patch is 6.6 mm X 6.6 mm.	89
4.33	$Z_g(\theta)$ comparison of modified constant grid impedance model with HFSS simulation results as benchmark for a patch AIS at 4 GHz. The dimensions of the single patch is 6.9 mm X 6.9 mm.	90
4.34	$Z_g(\theta)$ comparison of modified constant grid impedance model with HFSS simulation results as benchmark for a patch AIS at 5.5 GHz. The dimensions of the single patch is 6.9 mm X 6.9 mm.	90
4.35	$Z_g(\theta)$ comparison of modified constant grid impedance model with HFSS simulation results as benchmark for a patch AIS at 7.7 GHz. The dimensions of the single patch is 6.9 mm X 6.9 mm.	91
A.1	The original path (P) and steepest decent path (SDP).	103

List of Acronyms and Symbols

Table 0.1: Acronyms Used in This Thesis

Acronym	Definition
AIS	Artificial Impedance Surface
AMC	Artificial Magnetic Conductor
EBG	Electromagnetic Bandgap Structure
FSS	Frequency Selective Surface
HIS	High Impedance Surface
HPBW	Half-power Bandwidth
PBC	Periodic Boundary Condition
PEC	Perfect Electric Conductor
PMC	Perfect Magnetic Conductor
PML	Perfect Matching Layer
TE	Transverse Electric to the direction of propagation
TM	Transverse Magnetic to the direction of propagation

Table 0.2: Common Symbols Used in This Thesis

Symbol	Defintion
Γ	plane wave reflection coefficient
λ_0	free space wavelength
λ	wavelength
θ	the incident angle or the spherical coorinate
η_0	intrinsic impedance of free space
μ_0	permeability of free space
μ	permeability
ϵ_0	permittivity of free space

(Continued on next page)

Table 0.2 – continued from previous page

Symbol	Defintion
ϵ_r	relative permittivity of a dielectric
ϵ	permittivity
ω	angular frequency
σ	conductivity
α	transmitted angle in the dielectric
ϕ	spherical coordinates
δ	Dirac delta function
C	Capacitor
E	Symbols in boldface represents a vector
E	Electric field
H	Magnetic field
I	Electric current
J	Electric current density
L	Inductor
M	Magnetic current density
V	Voltage
Y	Admidance
Z	Impedance
e	electric mode vector used in the method of modal expansion
h	magnetic mode vector used in the method of modal expansion
f	frequency
i	modal current source used in the method of modal expansion
j	$j^2 = -1$
k_0	free space wave number
k	wave number
k_t	transverse wave number
l	mode number used in the method of modal expansion
p	mode number used in the method of modal expansion
q	mode number used in the method of modal expansion
r	spherical coordinates
v	modal voltage source used in the method of modal expansion
\hat{x}	unit vector of rectangular coordinates
\hat{y}	unit vector of rectangular coordinates
\hat{z}	unit vector of rectangular coordinates
x	x direction in the rectangular coordinates
y	x direction in the rectangular coordinates
z	x direction in the rectangular coordinates

Chapter 1

Introduction

1.1 Motivation

With the development of telecommunication systems that use wireless wearable devices, small and low-profile antennas become more desirable for medical or entertainment purposes [4]. However, the design of antennas that operate near the human body can be quite challenging. When antennas are placed close to the body without proper shielding, a significant part of radiated energy can be absorbed by the body, which leads to poor antenna radiation efficiency. Moreover, the performance of these antennas is quite sensitive to their locations on the body, which is also undesirable in antenna designs.

A common solution to the above problems is shielding the antennas from the body using a metal backing (e.g. an electric conductor or ground plane). The electric conductor can prevent antenna radiated energy from being absorbed by the body. Unfortunately, some antennas, such as a horizontally-oriented dipole, can not radiate efficiently over a practical bandwidth if they are placed too close to the electric conductor, (e.g. less than one tenth wavelength). For these antennas to radiate efficiently, these antennas can be placed one quarter wavelength away from the electric conductor, but the antenna profiles usually become too thick for wearable applications.

For low-profile antenna designs, it is common to use a thin dielectric slab on top of an electric conductor. We refer to this configuration as the grounded dielectric in this thesis. The problem with this configuration is that it can support surface waves [5, 6]. Surface waves radiate at the edge of a finite grounded dielectric and can result in undesired antenna radiation patterns.

To solve the problems of the electric conductor, a structure called the mushroom structure was introduced in [7]. This structure has two interesting characteristics. Firstly, at a certain frequency (e.g. the resonant frequency), it exhibits a plane wave reflection coefficient of +1 at normal incidence, therefore behaving like a magnetic conductor for normally illuminated plane waves. This way, an antenna may be placed close to the mushroom structure, such as less than one tenth wavelength, and have reasonably good radiation efficiency. Secondly, the mushroom structure has a surface wave stop band where no surface waves can propagate. Because of these characteristics, the mushroom structure is quite attractive and has been used extensively in antenna designs to reduce the antenna profiles and improve antenna radiation performance [8–14].

Originally, vias were used in the mushroom structure design. However, since it is difficult and expensive to build these vias, people stopped using them and the resulting structure is called the Artificial Impedance Surface (AIS) in this thesis. As with the mushroom structure, the plane wave reflection coefficient of the AIS structure at normal incidence is +1 at the resonant frequency. Thus, they are also widely used in antenna designs [15–19].

Although a lot of antennas were designed above various AIS structures, it was not well-understood how antenna radiation properties are related to the properties of the AIS structures. As a result, antenna designs involving AIS structures mostly depend on full-wave simulations, which are quite time-consuming due to the complexity of the AIS. In [7], evaluation of the phase of plane wave reflection coefficients at normal incidence was used to find the resonant frequency of the mushroom structure and a few types of antennas were designed at this frequency. In this manner, the most common design methodology in literature was: - find the resonant frequency of the mushroom or the AIS structure, - designing an antenna to resonate at this frequency, - directly mount the antenna above the mushroom or the AIS. However, this method usually leads to unexpected results because plane wave reflection coefficient only at normal incidence is inadequate to

characterize the interaction between the antenna and AIS when they are close to each other. Therefore, people start to include reflection coefficients at oblique incidence in the AIS characterization. A topic of interest was designing a stable AIS, with reflection coefficient of +1 for all incident angles at the AIS resonant frequency [1, 20, 21].

Although the AIS plane wave reflection coefficients were used extensively to aid in the designs of an antenna above an AIS surface, the relationship between the AIS plane wave reflection coefficients and antenna radiation properties, such as far-field patterns, has been rarely discussed. In [22] and [23], the far-field patterns of a half-wavelength dipole and an infinite line current above an AIS structure were given. However, the reflection coefficients and the equivalent impedance of the AIS were assumed to be a constant over the incident angle in [22] and [23], respectively. These assumptions are only valid for some AIS, and thus the far-field models in [22] and [23] were not accurate for most AIS structures.

To better understand the mushroom structure and the AIS, a circuit consisting of an inductor in parallel with a capacitor was used in [7, 24, 25] to model these structures. This circuit is only valid at plane wave normal incidence. In [23, 26], a similar circuit model was proposed for all incident angles. This circuit model consists of so-called a grid impedance in parallel with the equivalent impedance of a grounded dielectric. In [26], a few grid impedance models were given for some popular AIS, including two called the patch AIS and the Jerusalem cross AIS. However, it is shown in Chapter 4 that the grid impedance models of the patch and Jerusalem cross AIS were not accurate. Examples of a patch AIS and a Jerusalem cross AIS are shown in Chapter 2.

1.2 Objectives

The objectives of this thesis are summarized as follows.

- To develop a far-field model which makes a clear connection between the far-field patterns of a Hertzian dipole above an AIS and the plane wave reflection coefficients of

the AIS. This model should allow direct and accurate far-field pattern computation using reflection coefficients of the AIS at all incident angles. No assumption should be made about the reflection coefficients and the equivalent impedance of the AIS surface so that the far-field model can be used for a wide range of AIS structures.

- To investigate if the circuit model used in [23,26] and another grid impedance model, called the constant grid impedance model [27], can compute the plane wave reflection coefficients and the grid impedance accurately for a patch AIS and a Jerusalem cross AIS at all incident angles.

1.3 Thesis Outline

In Chapter 2, the motivation of using the mushroom structure and the AIS are introduced. The characteristics of the mushroom structure and the AIS are discussed. The state-of-art research is also reviewed.

In Chapter 3, a far-field model of a Hertzian dipole antenna above an AIS structure is derived from two methods. They are referred to as the transmitting method and the receiving method. Although approached differently, both methods result in far-field equations of the same form. These far-field equations are called our far-field model in this thesis. With this model, it is clear that the far-field patterns of the Hertzian dipole can be directly calculated from the plane wave reflection coefficients of the AIS. The accuracy of our far-field model is tested using a patch and a Jerusalem cross AIS. It is shown that, with accurate AIS reflection coefficients, the far-field patterns of the Hertzian dipole can be calculated quite accurately. Moreover, our far-field model is compared with far-field models introduced in [22] and [3], and it is shown that our model provides more accurate results.

In Chapter 4, the circuit model given in [23,26] and the constant grid impedance model [27] are used to calculate the plane wave reflection coefficients of the patch and

Jerusalem cross AIS used in Chapter 3. It is shown that the constant grid impedance model, although simple, computes the grid impedance and the reflection coefficients of the patch and Jerusalem cross AIS quite well. However, at the resonant frequency of the patch AIS, there is an error in the computed reflection coefficients. By analyzing the constant grid impedance model and the circuit model, it is found that the circuit model requires an extremely accurate grid impedance model at the AIS resonant frequency for accurate reflection coefficient computation. Therefore, the constant grid impedance model is modified for the patch AIS using a curve fitting technique. It is shown that this modified constant grid impedance model is quite accurate for various patch AIS at and below the AIS resonant frequency.

In Chapter 5, this thesis is concluded. The thesis contributions are summarized and future work is suggested.

Chapter 2

Background and Literature Review

In this chapter, the background and literature review are provided. The disadvantages of electrical conductors as antenna reflectors are discussed. This leads to a discussion of the characteristics of the mushroom structure and AIS structures, which make them superior to electric conductors. Then, a review of recent designs and analyses of antennas above an AIS structure is presented.

2.1 Electric Conductors as Antenna Reflectors

Electric conductors are commonly used as a part of antennas (e.g. antenna reflectors) to improve antenna gain and to partially shield objects on the other side [28]. However, they have two undesirable features which limit their applications. The first problem of the electric conductors is that some antennas, such as a horizontally-oriented dipole antenna, can not radiate efficiently in a practical bandwidth when placed close to an electric conductor. The second problem is that, when used with a dielectric slab, electric conductors can support surface waves.

Based on image theory [29], an equivalent image current can be used to model the influence of an electric conductor on a horizontally-oriented antenna. The equivalent image current that models an electric conductor is 180° out of phase with the antenna current. As shown in Figure 2.1, when the antenna is placed too close to an electric conductor, its current is canceled by the image current. This results in quite a small antenna radiation resistance; thus matching the antenna becomes difficult. A common solution to this problem is to place the antenna one quarter wavelength away from the electric conductor, as shown in Figure 2.2. This way, the radiated energy of the image current and the antenna current

add constructively, resulting in a more reasonable radiation resistance for matching. The drawback, however, is that the optimal distance between the antenna and the electric conductor is a quarter wavelength ($\lambda/4$), so the whole radiating structure can be quite thick.

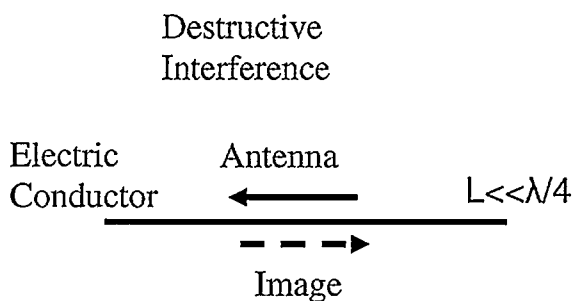


Figure 2.1: An antenna is placed close to an electric conductor. The image current cancels the antenna current out. λ is the wavelength.

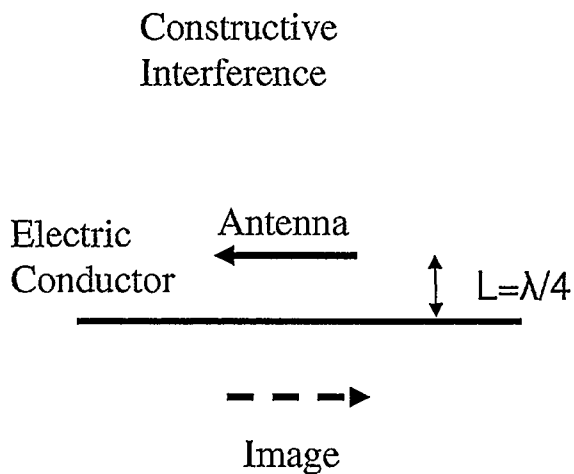


Figure 2.2: An antenna lying $\lambda/4$ away from an electric conductor. The image current adds constructively to the antenna current. λ is the wavelength.

The second undesirable feature of an electric conductor is that, when used with a dielectric slab, surface waves [5, 6] can be supported. Surface waves propagate along the surface of the grounded dielectric (e.g. the dielectric on top of the electric conductor) and decay exponentially in directions perpendicular to the surface. These waves do not radiate until they reach discontinuities. On a finite grounded dielectric, surface waves radiate at

the edge of the conductor, resulting in undesired antenna radiation patterns, as shown in Figure 2.3.

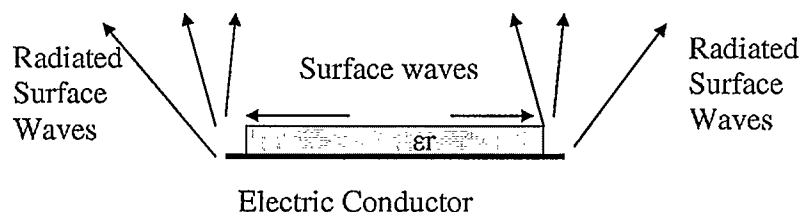


Figure 2.3: Surface waves propagate along the surface of an electric conductor and radiate at its edge.

2.2 Mushroom Structures as Antenna Reflectors

In 1999, Sievenpiper et al. introduced the mushroom structure as an attempt to solve the problems of the electric conductor [7]. This structure is composed of a layer of periodically arranged metal plates over an electric ground plane conductor, connected to the ground plane through vias. The top and side view of this structure is shown in Figure 2.4. The periodicity of the metal plates is typically much smaller than the free space wavelength.

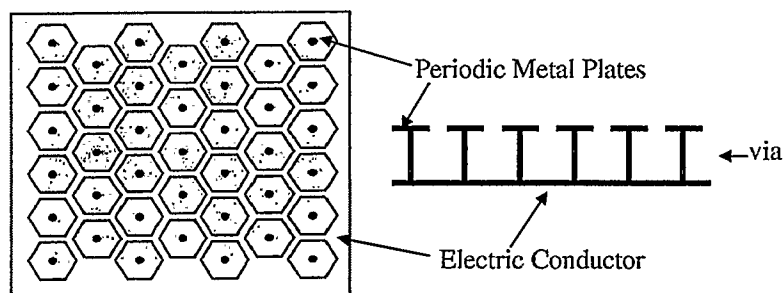


Figure 2.4: Top view and side view of the mushroom structure.

The mushroom structure, also referred to as a High Impedance Surface (HIS), has two interesting characteristics. Firstly, it has a frequency range over which no surface waves can propagate. This frequency range is known as the bandgap and for this reason the structure is also known as Electromagnetic Bandgap Structure (EBG) [8–10, 30]. Secondly, there is

a frequency at which the phase of the reflection coefficient of the mushroom structure is equal to 0° . This frequency is usually referred to as the resonant frequency of the structure. In Figure 2.5, the plane wave reflection phase of a mushroom structure at normal incidence is shown. As seen, the reflection phase varies from about 150° to -140° as the frequency increases. At the resonant frequency, the reflection phase is equal to 0° . Note that the resonant frequency is only defined at normal incidence. Due to the electric conductor at the bottom, waves incident on the mushroom structures are completely reflected. Therefore, the magnitude of the reflection coefficient is always 1. With the reflection coefficient being +1 at its resonant frequency, the mushroom structure works as a magnetic conductor for normally incident plane waves.

A magnetic conductor can provide a closely placed antenna, such as a horizontally-oriented dipole, a larger S11 bandwidth than an electric conductor. This is because the equivalent image current of a magnetic conductor is in-phase with the antenna current; thus constructively influences the antenna when antenna is close to the magnetic conductor [29]. Since magnetic conductors do not exist in nature, the mushroom structures become attractive for their ability to mimic magnetic conductors. Operated in this way, the mushroom structure is an Artificial Magnetic Conductor (AMC) [11, 12, 18, 31].

Because of the above properties, the mushroom structure solves both problems of the electric conductor, and is suggested to replace the electric conductor as antenna reflectors in [7]. As a result, they have been widely used in recent antenna designs [8–14].

2.3 Artificial Impedance Surfaces

The vias used in the mushroom structure are expensive to build, so people start to use one dielectric slab only in between the periodic layer and the electric conductor. The modified structure is referred to as an Artificial Impedance Surface (AIS). Sometimes, it is also referred to as a Frequency Selective Surface (FSS) [32]. Figure 2.6 shows a portion of an

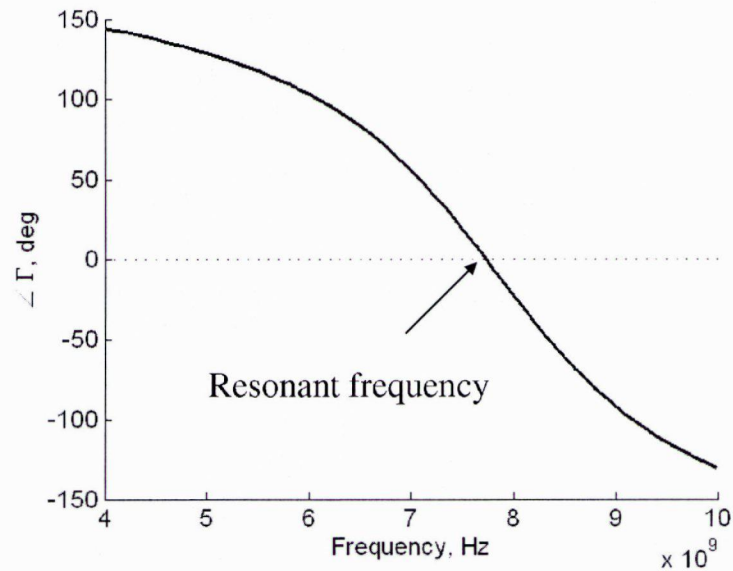


Figure 2.5: Plane wave reflection phase of a mushroom structure at normal incidence as a function of frequency.

infinite patch AIS [17], whose top layer is composed of periodically arranged patches. The top and side view of another popular AIS is shown in Figure 2.7. Due to its periodically arranged Jerusalem cross metal plate surface, this AIS is named as the Jerusalem cross AIS [2]. Other AIS designs, such as Uniplanar-Compact Periodic Bandgap Structures (UC-PBG), can be found in [12,31–34].

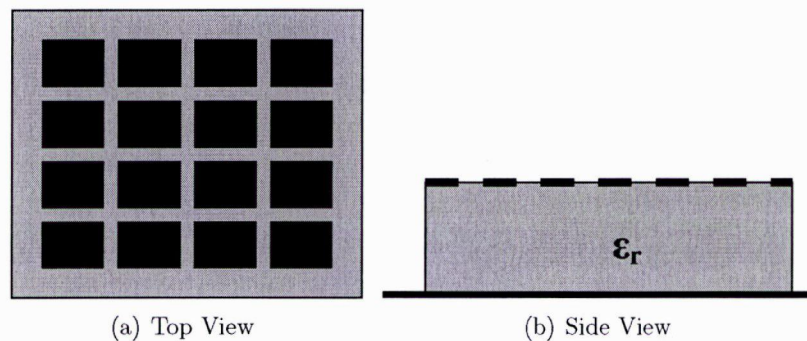


Figure 2.6: Top and side view of a patch AIS.

Sievenpiper et al. suggested that the 0° reflection phase property and the surface wave bandgap of mushroom structures occupy the same frequency range [7]. However, this

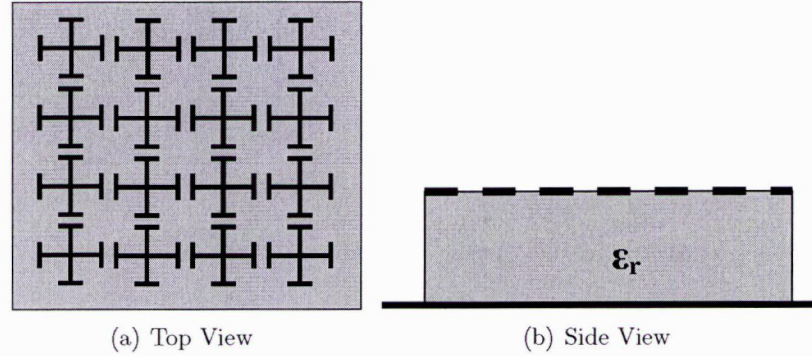


Figure 2.7: Top and side view of a Jerusalem cross AIS.

characteristic does not apply to AIS structures. Luckily, the 0° reflection coefficient can still be found at the resonant frequency of the AIS structure, which is also defined at normal incidence. By using AIS structures with capacitive periodic top surfaces, such as the patch AIS, Jerusalem cross AIS and the Uniplanar-Compact Periodic Bandgap Structure, the 0° reflection phase property can be achieved at microwave frequencies with a thin dielectric slab.

2.3.1 Antenna Designs over AIS Structures

Due to their 0° reflection phase property at normal incidence, the AIS structures are used extensively in literature as reflectors for all kinds of antenna applications [15–19]. The most common practice has been designing antennas that resonate at the resonant frequency of an AIS and directly mounting the antennas above the AIS. However, since the resonant frequency of an AIS is defined only for plane wave normal incidence, this procedure usually leads to unexpected antenna S11 and radiation patterns.

Recently, it was realized that using only reflection coefficients at normal incidence is inadequate to describe antenna's interaction with the AIS structure, indicating the importance of including reflection coefficients at oblique incidence. The reflection phase (e.g. Γ phase) of an AIS structure at oblique incidence is shown in Figure 2.8. It is seen that at different incident angle θ , the 0° reflection phase locates at different frequencies.

This means that the AIS only behaves as a magnetic conductor for parts of the antenna radiated energy while it might be an electric conductor for the other parts of radiation. Therefore, it was suggested in [1,20,21] to design an AIS that behaves as a real magnetic conductor at its resonant frequency. This requires the 0° reflection phase of all incident angles to locate at the resonant frequency, as shown in Figure 2.9. This AIS was referred to as a stable AIS.

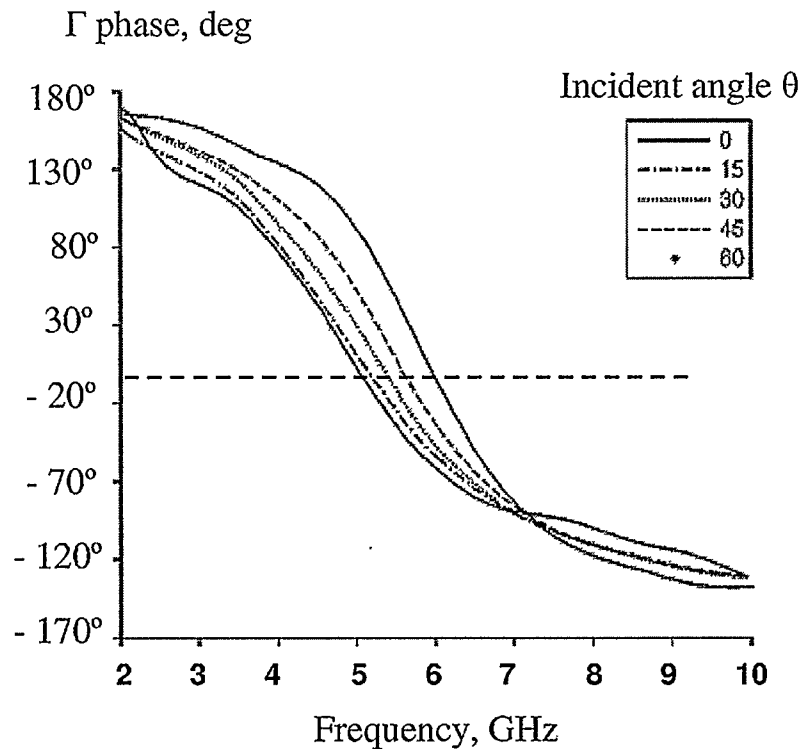


Figure 2.8: 0° reflection phase of an AIS structure shifts in frequency at different incident angles [1].

However, it was suggested that it is more desirable for some antennas to operate away from the AIS resonant frequency. For example, Sarabandi et al. [25] suggested that the largest S11 bandwidth of a horizontally-oriented dipole antenna above an AIS can be found when the mutual coupling between the dipole and its image under the AIS is minimized. When the distance between the dipole and the AIS is small (approximately 0.02λ), the least mutual coupling is achieved at the frequency where the reflection phase at normal

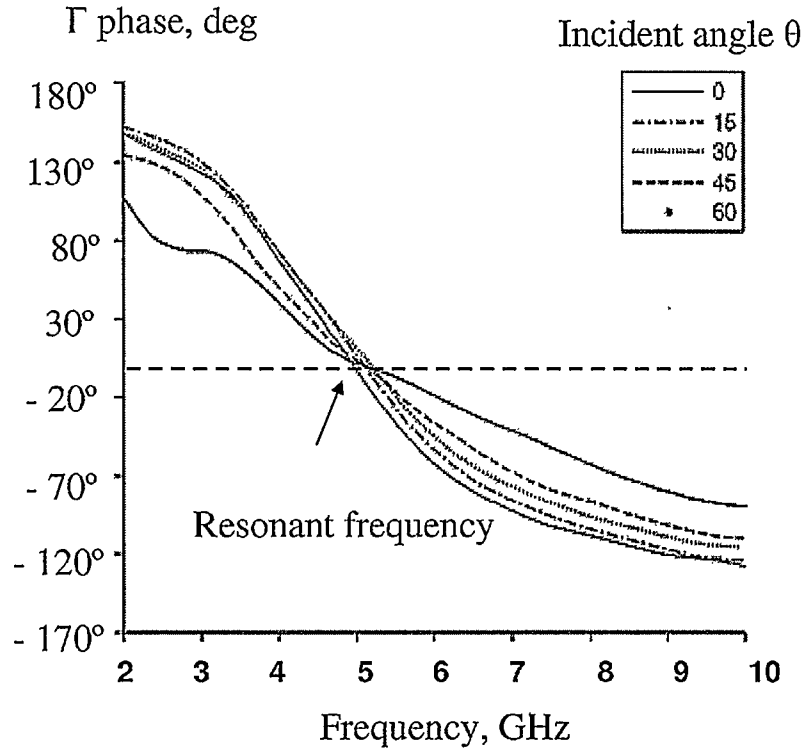


Figure 2.9: Reflection phase of a stable AIS at different incident angles [1].

incidence is about 145° . Dipoles operating at this frequency have higher gain and wider S11 bandwidth than at the AIS resonant frequency. This suggests that it is not critical for the dipole to operate above a stable AIS.

2.3.2 Far-Field Models for Antennas above an AIS

Although a lot of information about the plane wave reflection coefficient of an AIS is available, the relationship between this information and antenna radiation properties, such as far-field patterns, was rarely discussed. In [22], it was suggested that far-field patterns of a half-wavelength ($\lambda/2$) dipole antenna over an AIS was the product of the dipole free space patterns and the so-called AIS screen pattern, defined as [22],

$$E(\theta) = \exp(-jk_0h \cos \theta) + \exp(j\zeta + jk_0h \cos \theta), \quad (2.1)$$

where ζ is AIS reflection coefficient phase (e.g. Γ phase) at normal incidence; k_0 is the free space wave number; h is the distance between the antenna and the AIS; θ is the polar angle away from the AIS surface normal. This screen pattern was obtained by modeling the effect of the AIS surface as a dipole image, where a phase shift, ζ , was applied. Thus, the screen pattern can be viewed as the array pattern of two isotropic sources with a phase shift of ζ . In [22], ζ was assumed to be a constant when θ changes, so we refer to Equation (2.1) as the constant Γ model in this thesis. However, since the AIS reflection phase usually varies with incident angle, the constant Γ model is not accurate for most AIS.

Unlike [22], Tretyakov et al. [3] suggested that the H-plane far-field pattern of an infinite line current can be calculated by integrating the fields of the line current and its image current. With the help of exact image theory [35], the H-plane far-field pattern of the infinite line source was obtained as [3],

$$E(\theta) = \left| 1 + \frac{\cos \theta - Y_s}{\cos \theta + Y_s} \exp(-2jk_0h \cos \theta) \right|. \quad (2.2)$$

Again, k_0 is the free space wave number; h is the distance between the antenna and the AIS; θ is the polar angle away from the AIS surface normal; and Y_s is the normalized equivalent admittance of the AIS to the intrinsic impedance of free space ($\eta_0 = \sqrt{\mu_0/\epsilon_0}$). In [3], the equivalent impedance of the AIS, Y_s , was assumed to be a constant when θ changes. This assumption is not valid for all AIS surfaces because the equivalent AIS impedance usually varies with the incident angle and plane wave polarizations (e.g. transverse electric field to the direction of propagation, TE plane wave, or transverse magnetic field to the direction of propagation, TM plane wave). As a result, a constant impedance of the AIS for all incident angles can only be achieved for some AIS.

2.3.3 Circuit Models for AIS

To explain the electromagnetic characteristics of the mushroom structure, Sievenpiper et al. [7] used a parallel circuit of an inductor, L , and a capacitor, C , to model the mushroom

structure. This circuit model is shown in Figure 2.10. With this circuit model, the equivalent impedance and the reflection coefficient of the mushroom structure can be obtained at plane wave normal incidence. In [25], the same parallel circuit was used to model a patch AIS structure. It was suggested that the capacitance, C , can be obtained by solving the equivalent capacitance between two coplanar strips and the inductance, L , is the equivalent impedance of the grounded dielectric [25]. This parallel circuit, however, is only valid at plane wave normal incidence, and can not be used for other angles of incidence.

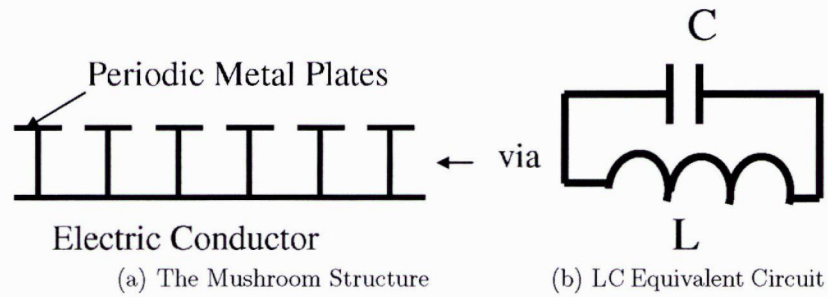


Figure 2.10: Equivalent LC parallel circuit model for the mushroom structure.

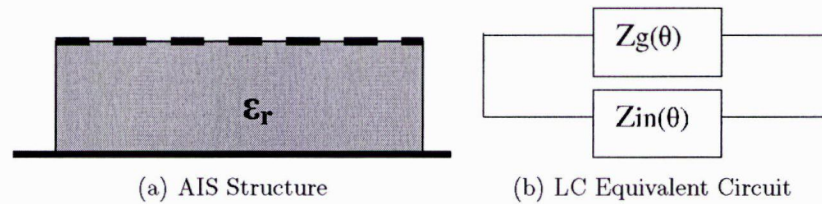


Figure 2.11: Equivalent LC parallel circuit model for the AIS structure.

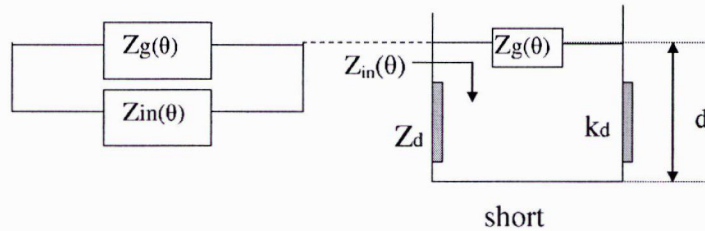


Figure 2.12: Equivalent transmission line circuit for Z_{in} computation. Z_d and k_d are the characteristic impedance and wave number of the equivalent transmission line. d is the thickness of the AIS dielectric slab. 'Short' represents the electric conductor on the bottom of the AIS structure.

In order to compute the plane wave reflection coefficients at all incident angles, a more general circuit model was proposed in [23, 26]. This circuit consists of a so-called grid impedance, $Z_g(\theta)$, which models the impedance of the periodic surface of the AIS, in parallel with the equivalent impedance of the grounded dielectric, $Z_{in}(\theta)$. This circuit model is shown in Figure 2.11(b). In this circuit, $Z_{in}(\theta)$ can be computed from a shorted transmission line equivalent circuit as shown in Figure 2.3.3. The grid impedance $Z_g(\theta)$ can be obtained from full-wave simulations or some circuit modeling. Usually, the grid impedance is different for different AIS. In [26], the grid impedance of the Jerusalem cross AIS is given as,

$$Z_g^{TE}(\theta) = Z_g(0), \quad Z_g^{TM}(\theta) = Z_g(0) \cos^2(\theta), \quad (2.3)$$

and that of the patch AIS as,

$$Z_g^{TE}(\theta) = \frac{Z_g(0)}{\cos^2 \theta}, \quad Z_g^{TM}(\theta) = Z_g(0), \quad (2.4)$$

for TE and TM incident plane waves. $Z_g(0)$ is the grid impedance at normal incidence. Equation (2.3) and (2.4) were obtained by solving the grid impedance of an infinite array of infinite long wires. It will be shown in Chapter 4 that Equations (2.3) and (2.4) can not model the grid impedance of the patch AIS and the Jerusalem cross AIS very well.

2.4 Summary

In this chapter, the disadvantages of electric conductors as antenna reflectors were discussed. Due to its abilities to overcome the problems of electric conductors, the Artificial Impedance Surfaces (AIS) is quite attractive, and have been used in several antenna designs. Even so, the relationship between antenna properties and the AIS properties was not well-understood. Therefore, antenna designs mostly depend on time-consuming full-wave simulations. Two far-field models have been proposed in literature to relate the AIS properties with antenna far-field patterns. However, both models made some assumptions

about the AIS properties so they can not be used for most AIS structures. In the next chapter, a new far-field model is derived using two different methods and it is shown that this far-field model can be used for a wide range of AIS structures.

Chapter 3

Far-Field Modeling of a Dipole Antenna above an Artificial Impedance Surface

In this chapter, H-plane and E-plane far-field patterns of a Hertzian dipole antenna above an infinite AIS surface are derived. In section 3.1, the method of modal expansion is briefly introduced to aid with the derivation. In sections 3.2 and 3.3, the far-field patterns of the Hertzian dipole are derived using two different methods, respectively. The first method, referred to as the transmitting method, uses the method of modal expansion to calculate the fields of the transmitting dipole. The second method first invokes the principle of reciprocity and then evaluates the terminal voltage of a receiving dipole using the method of modal expansion. Thus, this method is referred to as the receiving method. It is shown that these two methods result in the same normalized far-field pattern equations. These equations form our far-field model with which H- and E-plane patterns of the dipole above an AIS can be directly calculated using the plane wave reflection coefficients of the AIS structure. The accuracy of this model is tested in section 3.4, where far-field patterns computed using our model are compared with full-wave simulation results and two other far-field models. In the end, this chapter is summarized in section 3.5.

3.1 The Method of Modal Expansion

The method of modal expansion [29,36,37] is a useful tool to analyze cylindrical waveguides that consist of a homogeneous isotropic dielectric (with permittivity ϵ and permeability μ) and are bounded by a perfect electric conductor. Such a cylindrical waveguide is shown in Figure 3.1, where z is the direction of propagation, and the cross sections of the cylindrical

waveguides are independent of z . In this method, the transverse electromagnetic fields (\mathbf{E}_t and \mathbf{H}_t) on a cylindrical waveguide cross section are mathematically represented as a summation of infinite numbers of modes. Each mode is expressed as a mode vector, $\mathbf{e}(x, y)$ or $\mathbf{h}(x, y)$, which depends on the waveguide cross section, and its amplitude, $V(z)$ or $I(z)$, which satisfies the transmission line equations. In this manner, a complicated waveguide problem can be reduced to a set of transmission line with well-known characteristics.

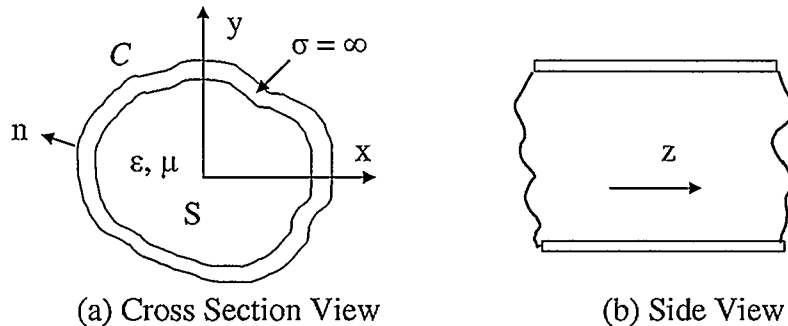


Figure 3.1: A cylindrical waveguide consisting of a homogeneous isotropic dielectric material bounded by a perfect electric conductor. S is the cross section surface area. C is the boundary curve of the cross section. n is the direction normal to the boundary curve C . σ is the conductivity.

By considering the AIS as the waveguide load, solving the far-fields of a Hertzian dipole above an AIS surface can be viewed as solving fields in a cylindrical waveguide that consists of a dielectric with free space permittivity and permeability (ϵ_0, μ_0) , and has infinite cross sections. This equivalence is shown in Figure 3.2. Therefore, it is convenient to apply the method of modal expansion to analyze the Hertzian dipole's far-fields above an AIS surface. Before doing so, we first introduce some important equations used in this method. These equations can be also found in [29, 36, 37].

As discussed, the transverse electric and magnetic fields (to the direction of propagation, z), \mathbf{E}_t and \mathbf{H}_t , in a homogeneous source-free region in a cylindrical waveguide (shown in Figure 3.1) can be mathematically expressed as a summation of infinite modes. Moreover, it is well-known that any arbitrary fields in a homogeneous source-free region can be expressed

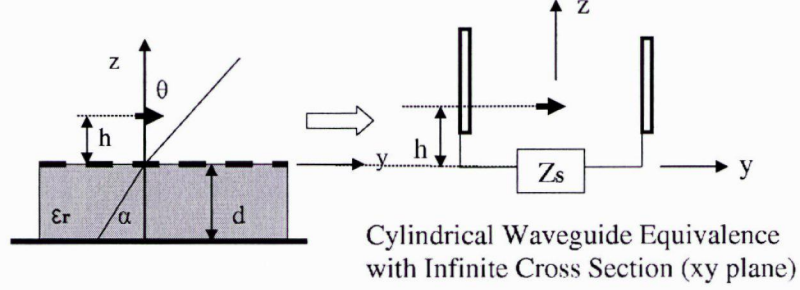


Figure 3.2: Cylindrical waveguide equivalence for a Hertzian dipole above an AIS.

as the sum of TE (e.g. transverse electric to z) fields and TM (e.g. transverse magnetic to z) fields [29]. In the same way, we can construct \mathbf{E}_t and \mathbf{H}_t in the cylindrical waveguide as [36],

$$\mathbf{E}_t(x, y, z) = \sum_{p=0}^{\infty} V_p^{TE}(z) \mathbf{e}_p^{TE}(x, y) + \sum_{q=0}^{\infty} V_q^{TM}(z) \mathbf{e}_q^{TM}(x, y), \quad (3.1)$$

$$\mathbf{H}_t(x, y, z) = \sum_{p=0}^{\infty} I_p^{TE}(z) \mathbf{h}_p^{TE}(x, y) + \sum_{q=0}^{\infty} I_q^{TM}(z) \mathbf{h}_q^{TM}(x, y). \quad (3.2)$$

Here, p and q are mode numbers. $\mathbf{e}^{TE}(x, y)$, $\mathbf{h}^{TE}(x, y)$ and $\mathbf{e}^{TM}(x, y)$, $\mathbf{h}^{TM}(x, y)$ are called the mode vectors of TE and TM type, respectively. Their amplitudes, $V^{TE}(z)$, $I^{TE}(z)$ and $V^{TM}(z)$, $I^{TM}(z)$ are called the modal voltage and current.

For Equations (3.1) and (3.2) to satisfy the Maxwell's equations in the waveguide of Figure 3.1, we obtain for TE modes [29, 37],

$$\mathbf{h}_l^{TE}(x, y) = -\nabla_t \Phi_l^{TE}(x, y), \quad (3.3)$$

$$\mathbf{e}_l^{TE}(x, y) = \mathbf{h}_l^{TE}(x, y) \times \hat{\mathbf{z}}. \quad (3.4)$$

where $l = p$ or $l = q$; $\nabla_t = \hat{\mathbf{x}} \frac{\partial}{\partial x} + \hat{\mathbf{y}} \frac{\partial}{\partial y}$; and $\hat{\mathbf{z}}$ is the unit vector in z direction; and $\Phi_l^{TE}(x, y)$ is obtained from,

$$\nabla_t^2 \Phi_l^{TE}(x, y) + k_{tl}^2 \Phi_l^{TE}(x, y) = 0, \quad (3.5)$$

where $k_{tl}^2 + k_z^2 = k^2$ and $k = \omega \sqrt{\epsilon \mu}$; on the waveguide wall requires $\partial \Phi_l^{TE}(x, y) / \partial n = 0$ on C , where n is the direction normal to the waveguide boundary.

Similarly, for TM modes [29, 37],

$$\mathbf{e}_l^{TM}(x, y) = -\nabla_t \Phi_l^{TM}(x, y), \quad (3.6)$$

$$\mathbf{h}_l^{TM}(x, y) = \hat{\mathbf{z}} \times \mathbf{e}_l^{TM}(x, y), \quad (3.7)$$

where $\Phi_l^{TM}(x, y)$ satisfy,

$$\nabla_t^2 \Phi_l^{TM}(x, y) + k_{tl}^2 \Phi_l^{TM}(x, y) = 0, \quad (3.8)$$

subject to the boundary condition on the waveguide wall, $\Phi_l^{TM}(x, y) = 0$ on C .

With $\mathbf{E}_t(x, y, z)$ and $\mathbf{H}_t(x, y, z)$ defined as in Equations (3.1) and (3.2), the modal voltage and current, $V_l(z)$ and $I_l(z)$, satisfy the transmission line equations [29, 37],

$$\frac{dV_l(z)}{dz} = -jk_{zl} Z_{0l} I_l(z), \quad (3.9)$$

$$\frac{dI_l(z)}{dz} = -jk_{zl} Y_{0l} V_l(z), \quad (3.10)$$

where $k_{zl} = \sqrt{k^2 - k_{tl}^2}$ and,

$$Z_{0l}^{TE} = \frac{1}{Y_{0l}^{TE}} = \frac{\omega\mu}{k_{zl}}, \quad (3.11)$$

$$Z_{0l}^{TM} = \frac{1}{Y_{0l}^{TM}} = \frac{k_{zl}}{\omega\epsilon}, \quad (3.12)$$

are the characteristic impedances for TE and TM modes, respectively. Therefore, we can draw an equivalent transmission line network for each mode, where $V_l(z)$ and $I_l(z)$ are the voltage and current on the transmission line, Z_{0l} is the characteristic impedance of the transmission line and k_{zl} is the wave number.

When an transverse electric or magnetic current source, \mathbf{J}_t or \mathbf{M}_t , is applied in the cylindrical waveguide, Equations (3.9) and (3.10) are modified to as [37],

$$\frac{dV_l(z)}{dz} = -jk_{zl} Z_{0l} I_l(z) - v_l(z) \quad (3.13)$$

$$\frac{dI_l(z)}{dz} = -jk_{zl} Y_{0l} V_l(z) - i_l(z) \quad (3.14)$$

where

$$v_l(z) = \int_S \mathbf{M}_t \cdot \mathbf{h}_l^* dS, \quad (3.15)$$

$$i_l(z) = \int_S \mathbf{J}_t \cdot \mathbf{e}_l^* dS, \quad (3.16)$$

and $()^*$ denotes the complex conjugate.

It is shown, by using the method of modal expansion, solving the transverse electromagnetic fields in a complicated cylindrical waveguide can be reduced to solving the mode vectors using Equations (3.3) to (3.8), and the modal voltage and current on a set of equivalent transmission lines using Equations (3.9) to (3.16). Now, let us consider a cylindrical waveguide with infinite cross sections, as in the case of an infinite AIS structure. With an infinite cross section, $\Phi_l^{TE}(x, y)$ and $\Phi_l^{TM}(x, y)$ can be expressed as,

$$\Phi_l(x, y) = A e^{-j(k_x x + k_y y)}, \quad (3.17)$$

where A is the normalization factor and can be computed by ensuring,

$$\int_S \mathbf{e}_p^{TE} \cdot \mathbf{e}_q^{TE} = \int_S \mathbf{e}_p^{TM} \cdot \mathbf{e}_q^{TM} = 1, p = q, \quad (3.18)$$

and,

$$\int_S \mathbf{h}_p^{TE} \cdot \mathbf{h}_q^{TE} = \int_S \mathbf{h}_p^{TM} \cdot \mathbf{h}_q^{TM} = 1, p = q. \quad (3.19)$$

where p and q are the mode numbers.

3.2 The Transmitting Method

In this section, the H- and E-plane far-field patterns of a Hertzian dipole over an infinite AIS surface are derived using the transmitting method. This method is referred to as the transmitting method because it directly calculates the fields of a transmitting Hertzian dipole. This method was used to solve an infinite magnetic line source above an impedance surface in [37]. Although the AIS surface is not an impedance surface, on which the impedance is everywhere the same, it can be modeled as an impedance surface when its

periodicity is small compared to free space wavelength [32,37]. Therefore, we can apply the transmitting method to solve for the far-fields of an Hertzian dipole above an AIS surface. To our knowledge, this has not been done previously. In sections 3.2.1 and 3.2.2, H-plane and E-plane far-field pattern equations of the Hertzian dipole are derived, respectively. The far-field equations are summarized in section 3.2.3.

Before the derivation, a Hertzian dipole above an AIS surface is shown in Figure 3.3. The dipole is oriented in the y direction, and the distance between the dipole and the AIS is h . The current density of the dipole is

$$\mathbf{J} = \hat{\mathbf{y}}\delta(x)\delta(y)\delta(z - h)e^{j\omega t}, \quad (3.20)$$

where δ denotes the Dirac delta function. The periodicity of the AIS is small compared to the free space wavelength.

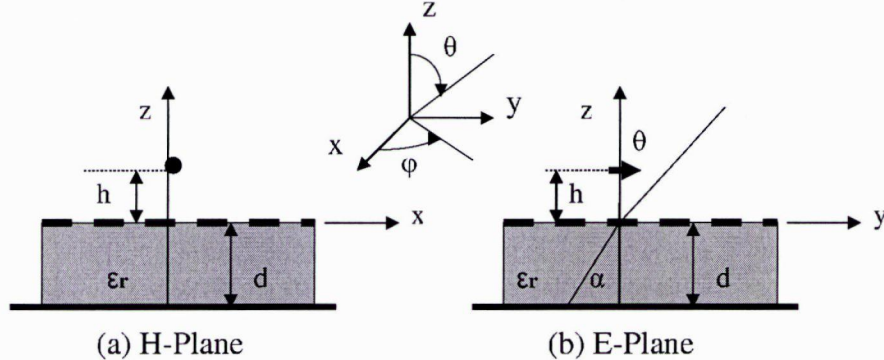


Figure 3.3: An Hertzian dipole above an AIS.

3.2.1 H-Plane Pattern

In this section, the principle H-plane far-field pattern is derived. On the principle H-plane (e.g. $y = 0$ plane in Figure 3.3(a)), the far-field pattern of the Hertzian dipole is, $|E_\phi(\theta)| = |E_y(\theta)|$. Therefore, the transverse electric field, $E_y(\theta)$, is first obtained using the method of modal expansion. Then, $E_y(\theta)$ is simplified for the far-fields using a method

called the steepest descent method. Finally, a simple pattern equation is obtained at the end of this section for the principle H-plane.

To obtain $E_y(\theta)$ using the method of modal expansion, the mode functions, $e_i^{TE}(x, y)$ and $e_i^{TM}(x, y)$, and their corresponding amplitude functions, $V_i^{TE}(z)$ and $V_i^{TM}(z)$, are needed for each mode. As discussed in the previous section, $\Phi_l(x, y)$ on an infinite cross section is,

$$\Phi_l^{TE}(x, y) = \Phi_l^{TM}(x, y) = Ae^{-j(k_{xl}x + k_{yl}y)}, \quad (3.21)$$

for all modes. Substituting Equation (3.21) into Equations (3.3) and (3.6), we obtain the TM electric mode function, $e_i^{TM}(x, y)$, and the TE magnetic mode function, $h_i^{TE}(x, y)$, as,

$$e_i^{TM}(x, y) = h_i^{TE}(x, y) = \hat{x} [Aj k_{xl} e^{-j(k_{xl}x + k_{yl}y)}] + \hat{y} [Aj k_{yl} e^{-j(k_{xl}x + k_{yl}y)}]. \quad (3.22)$$

With $k_{yl} = 0$ in the principle H-plane, Equation (3.22) is simplified to,

$$e_i^{TM}(x, y) = h_i^{TE}(x, y) = \hat{x} Aj k_{xl} e^{-jk_{xl}x}. \quad (3.23)$$

where $Aj k_{xl} = 1/2\pi$ is obtained by solving Equations (3.18) or (3.19). With Equations (3.4) and (3.7), mode functions, $e_i^{TE}(x, y)$ and $h_i^{TM}(x, y)$, are also obtained,

$$e_i^{TE}(x, y) = -\hat{y} \frac{1}{2\pi} e^{-jk_{xl}x}, \quad (3.24)$$

$$h_i^{TM}(x, y) = \hat{y} \frac{1}{2\pi} e^{-jk_{xl}x}. \quad (3.25)$$

Now that $e_i^{TE}(x, y)$ and $e_i^{TM}(x, y)$ are obtained, the next step is to calculate $V_i^{TE}(z)$ and $V_i^{TM}(z)$. To do this, it is convenient to draw an equivalent transmission line network for the H-plane of the Hertzian dipole above the AIS surface. This Equivalent network is shown in Figure 3.4. In this equivalent network, the AIS is represented as an equivalent impedance Z_s . $Z_{0l}^{TE} = \omega\mu_0/k_{zl}$ is the characteristic impedance of the equivalent transmission line of TE modes; and $k_{zl} = \sqrt{k_0^2 - k_{xl}^2}$. The source of the equivalent network is determined by,

$$i_l(z) = \iint \mathbf{J} \cdot (\mathbf{e}_l)^* dx dy, \quad (3.26)$$

with \mathbf{J} defined in Equation (3.20), and \mathbf{e}_i defined in Equations (3.23) and (3.24), respectively. Note that only $\mathbf{J} \cdot (\mathbf{e}_i^{TE}(x, y))^* \neq 0$. Therefore, the only source in Figure 3.4 is an electric current source that excites TE modes,

$$i_i^{TE}(z) = \iint \mathbf{J} \cdot (\mathbf{e}_i^{TE}(x, y))^* dx dy = -\frac{1}{2\pi} \delta(z - h). \quad (3.27)$$

This equation indicates that only TE modes are excited by the Hertzian dipole in the principle H-plane.

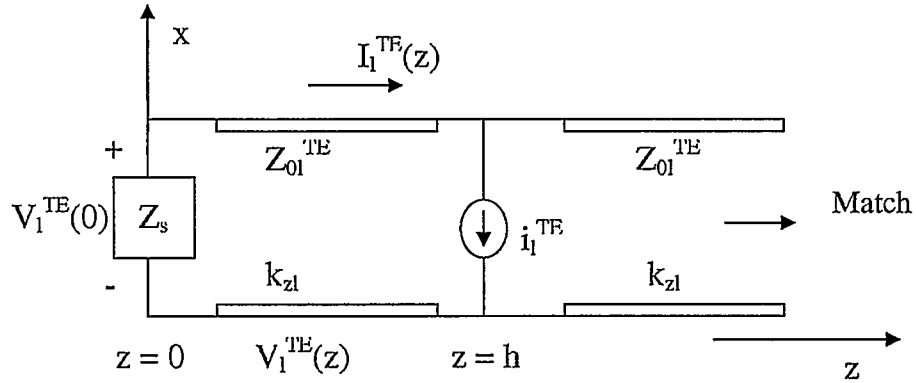


Figure 3.4: Equivalent network for H-plane of a Hertzian dipole over an AIS surface which is modeled as an impedance surface. i_i^{TE} is an electric current source at $z = h$. Z_s is the impedance of the AIS surface. Z_{0l}^{TE} is the characteristic impedance of the equivalent transmission line of TE modes. $k_{zl} = \sqrt{k_0^2 - k_{xl}^2}$.

By applying the basic circuit theory and transmission line theory, the modal voltage at any z on the transmission line can be calculated,

$$V_i^{TE}(z) = \frac{1}{4\pi} Z_{0l}^{TE} [e^{-jk_{zl}|z-h|} + \Gamma^{TE}(k_{xl}, k_{zl}) e^{-jk_{zl}(z+h)}]. \quad (3.28)$$

where $\Gamma^{TE}(k_{xl}, k_{zl})$ is the plane wave reflection coefficient of the AIS at $z = 0$, defined as,

$$\Gamma^{TE}(k_{xl}, k_{zl}) = \frac{Z_s(k_{xl}, k_{zl}) - Z_{0l}^{TE}(k_{zl})}{Z_s(k_{xl}, k_{zl}) + Z_{0l}^{TE}(k_{zl})}. \quad (3.29)$$

Substituting Equations (3.28) and (3.24) to Equation (3.1), the total transverse electrical field, E_y , above the AIS is obtained,

$$E_y(x, z) = \sum_{l=0}^{\infty} \left(-\frac{1}{4\pi} \right) Z_{0l}^{TE} [e^{-jk_{zl}|z-h|} + \Gamma^{TE}(k_{xl}, k_{zl}) e^{-jk_{zl}(z+h)}] \left(\frac{1}{2\pi} e^{-jk_{xl}x} \right), \quad (3.30)$$

for $z > 0$, with $\Gamma^{TE}(k_{xl}, k_{zl})$ defined in Equation (3.29). The first term in the above equation represents the contribution of the source, e.g. the Hertzian dipole, and the second term represents fields contributed by the AIS surface.

The summation can be replaced with an integral since k_{zl} of the dipole is continuous on an impedance surface, Equation (3.30) can be written as,

$$E_y(x, z) = -\frac{\omega\mu_0}{8\pi^2} \int_{-\infty}^{\infty} \frac{1}{k_z} [e^{-jk_z|z-h|} + \Gamma^{TE}(k_{xl}, k_{zl})e^{-jk_z(z+h)}] e^{-jk_x x} dk_x. \quad (3.31)$$

With the change of variables [37], Equation (3.31) can be written as,

$$E_y(x, z) = -\frac{\omega\mu_0}{8\pi^2} \int_{-\infty}^{\infty} [e^{jk_z h} + \Gamma^{TE}(k_x, k_z)e^{-jk_z h}] \frac{e^{-j(k_x x + k_z z)}}{k_z} dk_x, \quad (3.32)$$

with $k_z = \sqrt{k_0^2 - k_x^2}$. In order to evaluate the above integral, the following transformation is introduced [37],

$$k_z = k_0 \cos w, \quad k_x = k_0 \sin w, \quad (3.33)$$

where w is a complex value. Substituting Equation (3.33) to Equation (3.32) and introducing spherical coordinates,

$$E_y(r, \theta) = -\frac{\omega\mu_0}{8\pi^2} \int_P [e^{jk_0 h \cos w} + \Gamma^{TE}(w)e^{-jk_0 h \cos w}] e^{-jk_0 r \cos(w-\theta)} dw, \quad (3.34)$$

is obtained, where P is the appropriate path of integration.

To evaluate Equation (3.34), the fast converging steepest descent method [38] is employed so that a simple asymptotic expression can be obtained for the far-fields ($\beta = k_0 r \gg 1$). The methodology of the steepest descent method is finding a special path of the integral on which only a small part of this path contributes significantly to the integral. This path is called the steepest descent path. Since only a small part of this path is important to the integral, the integral in Equation (3.34) can be evaluated only around that region, and thus can be expressed as a simple function. A brief discussion of the steepest descent method is given in Appendix A.

By using this method, $E_y(r, \theta)$ in Equation (3.34) is simplified to the sum of two parts: a steepest descent part, E_{SDP} , and a residue part, $E_{residue}$,

$$\begin{aligned} E_y(r, \theta) &= E_{SDP} + E_{residue} \\ &\approx -\sqrt{\frac{2\pi}{k_0 r}} \frac{\omega \mu_0}{8\pi^2} \left[e^{jk_0 h \cos \theta} + \Gamma^{TE}(\theta) e^{-jk_0 h \cos \theta} \right] e^{-j(k_0 r - \frac{\pi}{4})} \\ &\quad + E_{residue}, \end{aligned} \quad (3.35) \quad \left(-\frac{\pi}{2} < \theta < \frac{\pi}{2}\right)$$

for $\beta = k_0 r \gg 1$. The residue term $E_{residue}$ represents surface waves propagating along the AIS surface [37]. On an infinite AIS, no surface wave can radiate and affect far-field patterns. Moreover, the frequency range of interest in this thesis is below the resonant frequency of the AIS. In this frequency range, all AIS exhibit inductive impedances, which only support TM surface waves. Since the Hertzian dipole excites TE waves in the H-plane, no surface waves are excited in the H-plane. As a result, $E_{residue}$ term can be dropped from Equation (3.35).

Hence, the total electric field above the AIS surface excited by the Hertzian dipole is,

$$E_y(r, \theta) \approx -\sqrt{\frac{2\pi}{k_0 r}} \frac{\omega \mu_0}{8\pi^2} \left[e^{jk_0 h \cos \theta} + \Gamma^{TE}(\theta) e^{-jk_0 h \cos \theta} \right] e^{-j(k_0 r - \frac{\pi}{4})}, \quad (3.36)$$

with the far-field approximation, and thus the normalized H-plane far-field pattern of the dipole above an AIS surface can be written as,

$$|E_\phi(\theta)| \approx \left| e^{jk_0 h \cos \theta} + \Gamma^{TE}(\theta) e^{-jk_0 h \cos \theta} \right|, \quad (3.37)$$

with $\Gamma^{TE}(\theta)$, the plane wave reflection coefficient at the AIS surface, defined in Equation (3.29) and $-\frac{\pi}{2} < \theta < \frac{\pi}{2}$. Equation (3.37) indicates that the principle H-plane far-field pattern of a Hertzian dipole above an AIS surface, $|E_\phi(\theta)|$, can be computed directly from the plane wave reflection coefficient of the AIS, $\Gamma^{TE}(\theta)$.

3.2.2 E-Plane Pattern

In this section, the principle E-plane far-field pattern of the Hertzian dipole is derived. In this plane (e.g. $x = 0$ plane shown in Figure 3.3(b)), the far-field pattern is, $|E_\theta(\theta)| =$

$|\cos\theta E_y(\theta) - \sin\theta E_z(\theta)|$. As the previous section, $E_y(\theta)$ and $E_z(\theta)$ are first obtained using the method of modal expansion. Then, they are simplified using the steepest descent method. Finally, a simple pattern equation is obtained for the principle E-plane.

To calculate the transverse electric field $E_y(\theta)$, the mode functions, $e_i^{TE}(x, y)$ and $e_i^{TM}(x, y)$, and their amplitude functions, $V_i^{TE}(z)$ and $V_i^{TM}(z)$, need to be computed. The normalized mode functions, $e_i^{TM}(x, y)$ and $h_i^{TE}(x, y)$, can be obtained by applying $k_{xl} = 0$ in Equation (3.22),

$$e_i^{TM}(x, y) = h_i^{TE}(x, y) = \hat{y} A j k_{yl} e^{-jk_{yl}y} = \hat{y} \frac{e^{-jk_{yl}y}}{2\pi}. \quad (3.38)$$

Substituting Equation (3.38) to Equations (3.4) and (3.7), we obtain,

$$h_i^{TM}(x, y) = -\hat{x} \frac{e^{-jk_{yl}y}}{2\pi}, \quad e_i^{TE}(x, y) = \hat{x} \frac{e^{-jk_{yl}y}}{2\pi}. \quad (3.39)$$

In order to calculate the amplitude functions, $V_i^{TE}(z)$ and $V_i^{TM}(z)$, we draw the equivalent transmission line network for the principle E-plane of the Hertzian dipole, shown in Figure 3.5. This time, the only non-zero source of this equivalent network is an electric current source that excites TM waves,

$$i_i^{TM}(z) = \iint \mathbf{J} \cdot (e_i^{TM}(x, y))^* dx dy = \frac{1}{2\pi} \delta(z - h), \quad (3.40)$$

since only $\mathbf{J} \cdot (e_i^{TM}(x, y))^* \neq 0$. Again, $\mathbf{J} = \hat{y} \delta(x) \delta(y) \delta(z - h) e^{j\omega t}$ is defined in Equation (3.20) and $e_i^{TM}(x, y)$ in Equation (3.38). This indicates that only TM modes are excited in the E-plane. In Figure 3.5, Z_s is the equivalent impedance of the AIS; $Z_{0l}^{TM} = k_{zl}/\omega\epsilon_0$ is the characteristic impedance of the equivalent transmission line of TM modes, and $k_{zl} = \sqrt{k_0^2 - k_{yl}^2}$.

With the help of the equivalent transmission line network, we can obtain the modal voltage at any z on the transmission line as before,

$$V_i^{TM}(z) = \frac{1}{4\pi} Z_{0l}^{TM} [e^{-jk_{zl}|z-h|} + \Gamma^{TM}(k_{yl}, k_{zl}) e^{-jk_{zl}(z+h)}], \quad (3.41)$$

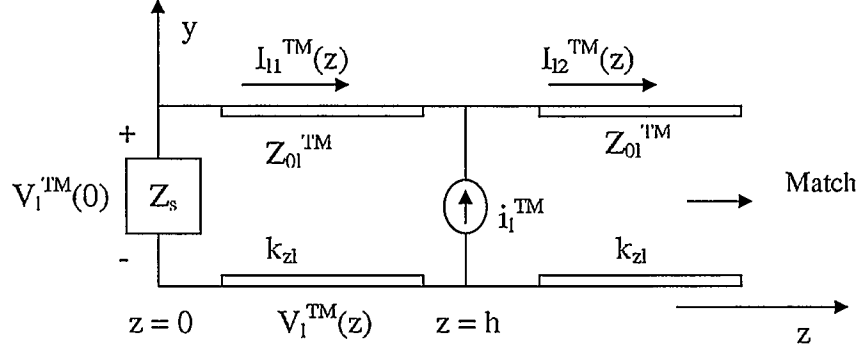


Figure 3.5: Equivalent modal network for the E-plane of the Hertzian dipole above an AIS surface. Z_s is the equivalent impedance of the AIS; $Z_{0l}^{TM} = k_{zl}/\omega\epsilon_0$ is the characteristic impedance of the equivalent transmission line of TM mode, and $k_{zl} = \sqrt{k_0^2 - k_{yl}^2}$.

where the plane wave reflection coefficient $\Gamma^{TM}(k_{yl}, k_{zl})$, measured at $z = 0$ is defined as,

$$\Gamma_l^{TM}(k_{yl}, k_{zl}) = \frac{Z_s(k_{yl}, k_{zl}) - Z_{0l}^{TM}(k_{zl})}{Z_s(k_{yl}, k_{zl}) + Z_{0l}^{TM}(k_{zl})}. \quad (3.42)$$

Following the same procedure as in the H-plane derivation, the transverse electric field, E_y , can be approximated as,

$$E_y(r, \theta) \approx \cos^2 \theta \sqrt{\frac{2\pi}{k_0 r} \frac{\omega \mu_0}{8\pi^2}} [e^{jk_0 h \cos \theta} + \Gamma^{TM}(\theta) e^{-jk_0 h \cos \theta}] e^{-j(k_0 r - \frac{\pi}{4})} + E_{residue}, \quad \left(-\frac{\pi}{2} < \theta < \frac{\pi}{2}\right) \quad (3.43)$$

for far-fields ($k_0 r \gg 1$). $\Gamma^{TM}(\theta)$ is the reflection coefficient measured at the AIS top surface and is defined in Equation (3.42).

As discussed before, in our frequency range of interest, (e.g. below the AIS resonant frequency), the AIS surface is inductive, so TM surface waves can be supported. In the E-plane, TM waves are excited by the dipole. Therefore, TM surface waves can propagate on the AIS surfaces in the frequency range of interest in this plane. On an infinite AIS, $E_{residue}$ term can be dropped because surface waves can not radiate and affect the far-field patterns. However, on a finite AIS, TM type surface waves can radiate at the edges of the AIS and thus $E_{residue}$ has to be included in Equation (3.43). With the assumption of an

infinite AIS, we can drop the $E_{r\text{residue}}$ term in Equation (3.43) and obtain,

$$E_y(r, \theta) \approx \cos^2 \theta \sqrt{\frac{2\pi}{k_0 r} \frac{\omega \mu_0}{8\pi^2}} [e^{jk_0 h \cos \theta} + \Gamma^{TM}(\theta) e^{-jk_0 h \cos \theta}] e^{-j(k_0 r - \frac{1}{4}\pi)}. \quad (3.44)$$

To compute $E_\theta(\theta)$, the axial electric field, $E_z(\theta)$ is also needed. From the Maxwell's equations [29],

$$E_z = \sum_{l=0}^{\infty} \frac{k_{zl}^2}{j\omega\epsilon} \Phi_l^{TM}(x, y) I_l^{TM}(z) \quad (3.45)$$

is obtained for TM modes. Here, $k_{zl}^2 = k_{yl}^2$ and $\Phi_l^{TM}(x, y) = e^{-jk_{yl}y} / (2\pi)(jk_{yl})$ since $k_{xl} = 0$ on the principle E-plane. With the help of Figure 3.5 and transmission line theory, we obtain,

$$I_{l1}(z) = -\frac{1}{4\pi} [e^{jk_{zl}(z-h)} - \Gamma^{TM}(k_{yl}, k_{zl}) e^{-jk_{zl}(z+h)}], \quad (3.46)$$

for $z \leq h$ and,

$$I_{l2}(z) = \frac{1}{4\pi} [e^{-jk_{zl}(z-h)} + \Gamma^{TM}(k_{yl}, k_{zl}) e^{-jk_{zl}(z+h)}], \quad (3.47)$$

for $z \geq h$ while $\Gamma^{TM}(k_{yl}, k_{zl})$ is defined in Equation (3.42). Substituting Equation (3.46) and (3.47) into Equation (3.45) and employing the transformation as before,

$$E_z(r, \theta) = -\frac{\omega \mu_0}{8\pi^2} \int_P \sin w \cos w [e^{jk_0 h \cos w} + \Gamma^{TM}(w) e^{-jk_0 h \cos w}] e^{-jk_0 r \cos(w-\theta)} dw. \quad (3.48)$$

is obtained for all z . Using the steepest descent method [38], Equation (3.48) becomes,

$$E_z(r, \theta) \approx -\sin \theta \cos \theta \sqrt{\frac{2\pi}{k_0 r} \frac{\omega \mu_0}{8\pi^2}} [e^{jk_0 h \cos \theta} + \Gamma^{TM}(\theta) e^{-jk_0 h \cos \theta}] e^{-j(k_0 r - \frac{\pi}{4})}, \quad (3.49)$$

with $\Gamma^{TM}(\theta)$ defined in Equation (3.42) and for $-\frac{\pi}{2} < \theta < \frac{\pi}{2}$.

With $E_y(\theta)$ in Equation (3.44) and $E_z(\theta)$ in Equation (3.49), $|E_\theta|$ can be obtained as,

$$\begin{aligned} |E_\theta| &= |\cos \theta E_y(\theta) - \sin \theta E_z(\theta)| \\ &\approx \left| \cos \theta \sqrt{\frac{2\pi}{k_0 r} \frac{\omega \mu_0}{8\pi^2}} [e^{jk_0 h \cos \theta} + \Gamma^{TM}(\theta) e^{-jk_0 h \cos \theta}] e^{-j(k_0 r - \frac{\pi}{4})} \right|, \end{aligned} \quad (3.50)$$

and the normalized E-plane far-field pattern is,

$$|E_\theta(r, \theta)| \approx |\cos \theta (e^{jk_0 h \cos \theta} + \Gamma^{TM}(\theta) e^{-jk_0 h \cos \theta})|, \quad (3.51)$$

with $\Gamma^{TM}(\theta)$ defined in Equation (3.42) and for $-\frac{\pi}{2} < \theta < \frac{\pi}{2}$. As before, it is seen from Equation(3.51) that the principle E-plane far-field pattern of the Hertzian dipole, $|E_\theta(r, \theta)|$, can be computed directly from the plane wave reflection coefficient of the AIS, $\Gamma^{TM}(\theta)$.

3.2.3 Far-field Pattern Equations Summary

As shown in the previous two sections, the H- and E-plane patterns of a Hertzian dipole above an AIS surface are derived using the transmitting method. The pattern equations are summarized below,

$$|E_\phi(r, \theta)| \approx |e^{jk_0 h \cos \theta} + \Gamma^{TE}(\theta)e^{-jk_0 h \cos \theta}|. \quad (3.52)$$

for the principle H-plane and,

$$|E_\theta(r, \theta)| \approx |\cos \theta(e^{jk_0 h \cos \theta} + \Gamma^{TM}(\theta)e^{-jk_0 h \cos \theta})|. \quad (3.53)$$

for the principle E-plane. $\Gamma^{TE}(\theta)$ and $\Gamma^{TM}(\theta)$ are plane wave reflection coefficients measured at the AIS surface and can be obtained from Equations (3.29) and (3.42).

3.3 Receiving Method

Although the transmitting method can be used for deriving the far-fields for the Hertzian dipole above an AIS surface, it involves a lot of complicated computations. In this section, the far-field patterns of the dipole are derived using a much simpler method, the receiving method, and it is shown that the far-field patterns derived using the receiving method are the same as those derived using the transmitting method. By invoking the principle of reciprocity, the receiving method changes the problem of solving the far-field patterns of a Hertzian dipole into solving the transverse electric fields on the dipole terminal as the dipole is illuminated by plane waves. The transverse electric fields on the dipole terminal are then calculated using the method of modal expansion. The receiving method was used for analyzing leaky wave antennas [27], but to our knowledge, this is the first time that

it is being used for analyzing AIS surfaces. In section 3.3.1, the principle of reciprocity is reviewed. H- and E-plane pattern equations of the dipole are derived in sections 3.3.2 and 3.3.3, respectively. Finally, the pattern equations are summarized and our far-field model is described in section 3.3.4.

3.3.1 Reciprocity for Antennas

The principle of reciprocity is illustrated in Figure 3.6. Assuming the medium between two antennas is isotropic and linear, the reciprocity [39] states that if a current, I_a , is applied to the terminal of the transmitting antenna A, and energy flows from it producing a voltage, V_b , at the terminal of the receiving antenna B; then when I_a is applied to antenna B as a transmitting antenna, the voltage produced on antenna A is equal to V_b . Essentially, reciprocity indicates that the transmitting far-field pattern of antenna A, (e.g. the far-field pattern of the transmitting antenna A, as shown in Figure 3.6(a)), is the same as its receiving far-field pattern, (e.g. the voltage induced on the receiving antenna A's terminal due to the transmitting antenna B, as shown in Figure 3.6(b)).

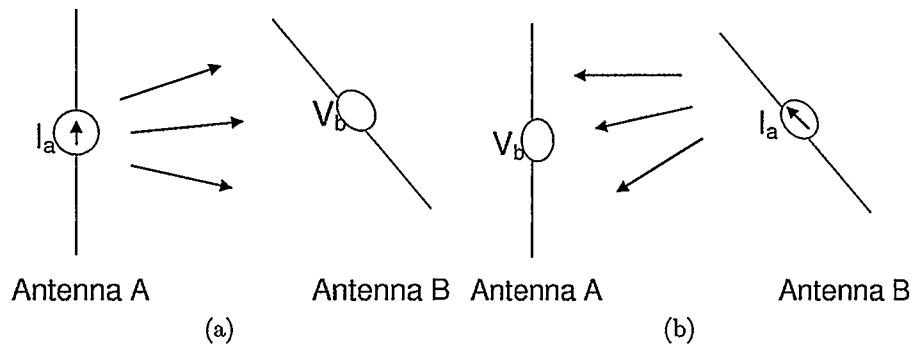


Figure 3.6: Illustration of the principle of reciprocity for antennas.

Let both antenna A and B be Hertzian dipoles, and bring an infinite AIS structure close to the Hertzian dipole A (antenna A), as shown in Figure 3.7. According to reciprocity, when the Hertzian dipole A is transmitting, its far-field pattern, ($|E_\phi(\theta)|$ or $|E_\theta(\theta)|$ in Figure 3.7(a)), is equal to the absolute value of the transverse electric field, ($|E_y|$ in

Figure 3.7(b)), produced at its terminal when the Hertzian dipole B is transmitting. Observing Figure 3.7(b) in which the Hertzian dipole B is transmitting, the dipole B is in the far-field of dipole A, so its radiated waves can be viewed as plane waves in the vicinity of the dipole A. Therefore, the computation of far-field patterns of a transmitting Hertzian dipole near an infinite AIS is equivalent to calculating the transverse electric fields at the terminal of the dipole when illuminated by plane waves.

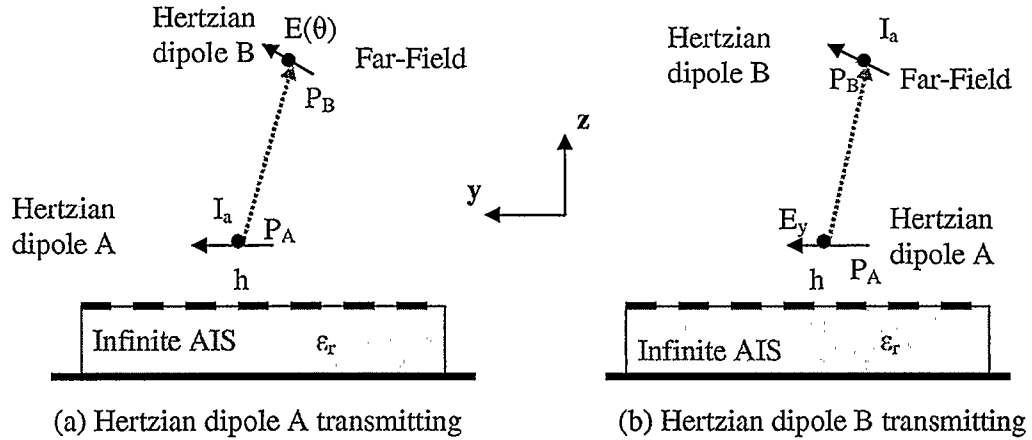


Figure 3.7: Applying reciprocity to Hertzian dipole above an AIS surface.

3.3.2 H-Plane Pattern

The principle H-plane of the Hertzian dipole above an infinite AIS is shown in Figure 3.8(a). Applying reciprocity, the far-field pattern at a polar angle θ away from the z direction, ($|E_\phi(\theta)|$) as shown in Figure 3.8(a)), can be obtained by calculating the absolute value of transverse electric field, $|E_y|$ (see Figure 3.8(b)), when the AIS is incident by a TE plane wave with an incident angle of θ . As shown in Figure 3.8(b), the TE plane wave has only transverse electric fields to the direction of propagation. By changing the incident angle of the TE plane wave from -90° to 90° and computing $|E_y|$ at each incident angle, the whole H-plane far-field pattern can be obtained.

When a plane wave is incident on an AIS, more than one plane waves is reflected due to the periodicity of the AIS [32]. The fundamental reflected wave satisfies the law of

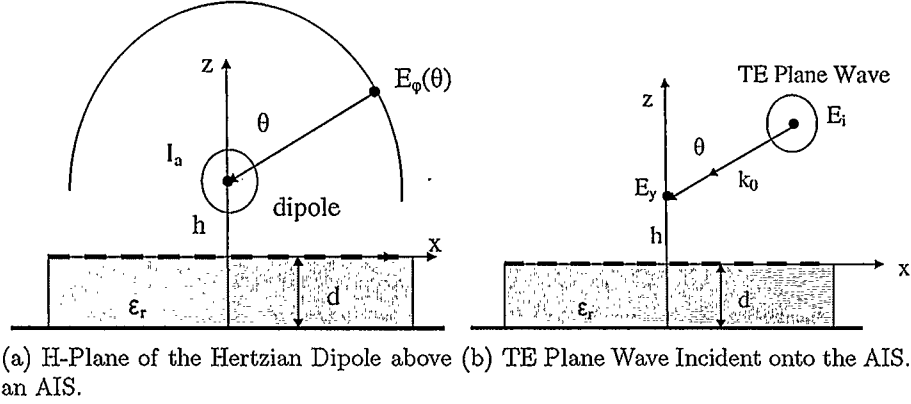


Figure 3.8: The H-plane pattern can be calculated from the transverse electric field near the AIS when the surface is incident by a TE plane wave.

reflection, that is, the angle of reflection is equal to the angle of incidence. The rest are evanescent waves when the periodicity of the AIS is smaller than a half-wavelength [32]. These evanescent waves die out very quickly away from the AIS top surface, so they can be ignored for field computations above the AIS top surface. Since the periodicity of the AIS considered in this thesis is small enough, we only need to consider the fundamental reflected waves. This is equivalent to assuming that the AIS surface acts as an impedance surface.

In order to compute the transverse electric field $|E_y|$ at the Hertzian dipole terminal, the method of modal expansion is used. An equivalent transmission line network is shown in Figure 3.9. In this equivalent network, Z_s is the equivalent impedance of the AIS. Using Equation (3.11) and noting $k_z = k_0 \cos \theta$, the characteristic impedance of the transmission line can be obtained as, $Z_0^{TE} = Z_0 \cos \theta$, where $Z_0 = \sqrt{\mu_0/\epsilon_0}$ is the intrinsic impedance of free space.

With Figure 3.9 and Equation (3.24), also keeping only the fundamental mode in Equation (3.1), the transverse electric field E_y at the dipole terminal ($z = h$) can be

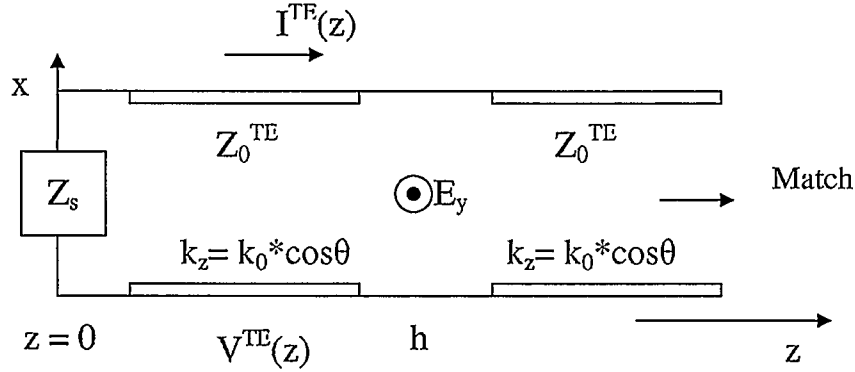


Figure 3.9: Equivalent transmission line network for the H-plane of the Hertzian dipole over an AIS. Z_s is the equivalent impedance of the AIS. The characteristic impedance of the transmission line is $Z_0^{TE} = Z_0 \cos \theta$. $Z_0 = \sqrt{\mu_0/\epsilon_0}$ is the intrinsic impedance of free space. $k_z = k_0 \cos \theta$ is the wave number in z direction.

calculated as,

$$\begin{aligned} E_y^{TE}(z=h) &= V(z=h)e^{TE}(x,y) \\ &= -V_0^+(0)(e^{jk_0 h \cos \theta} + \Gamma^{TE}(\theta)e^{-jk_0 h \cos \theta}) \frac{e^{-jk_z x}}{2\pi} \hat{y}, \end{aligned} \quad (3.54)$$

where, $V_0^+(0)$ is the voltage of the incident plane wave at $z=0$; $\Gamma^{TE}(\theta)$ is the reflection coefficient of TE incident wave measured at the AIS surface. Therefore, the normalized H-plane far-field pattern is,

$$|E_\phi(\theta)| = |E_y^{TE}(z=h)| = |e^{jk_0 h \cos \theta} + \Gamma^{TE}(\theta)e^{-jk_0 h \cos \theta}|, \quad (3.55)$$

with,

$$\Gamma^{TE}(\theta) = \frac{Z_s(\theta) - Z_0^{TE}(\theta)}{Z_s(\theta) + Z_0^{TE}(\theta)}. \quad (3.56)$$

3.3.3 E-Plane Pattern

Similarly, the principle E-plane far-field pattern, $|E_\theta(\theta)|$ as shown in Figure 3.10(a), can be obtained by solving the transverse electric fields, E_y as shown in Figure 3.10(b), with a TM plane wave illuminate on the AIS. The TM plane wave only has transverse magnetic fields. By changing the incident angle θ from -90° to 90° , the whole E-plane pattern is obtained.

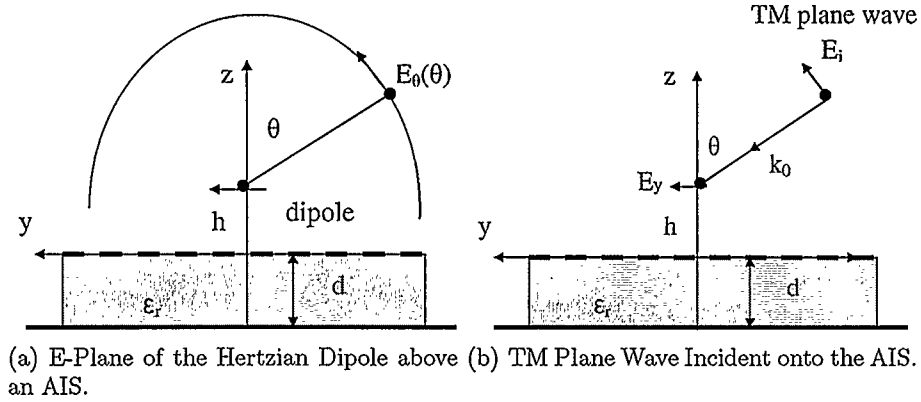


Figure 3.10: The E-plane pattern can be calculated from the transverse electric field near the AIS when the surface is incident by a TM plane wave.

As with the H-plane derivation, modal expansion is used here. The equivalent transmission line network is shown in Figure 3.11. Again, Z_s is the equivalent impedance of the AIS. With Equation (3.12) and $k_z = k_0 \cos \theta$, we can compute the characteristic impedance of the transmission line, $Z_0^{TM} = \omega \mu_0 / k_z = Z_0 \cos \theta$, where $Z_0 = \sqrt{\mu_0 / \epsilon_0}$ is the intrinsic impedance of free space.

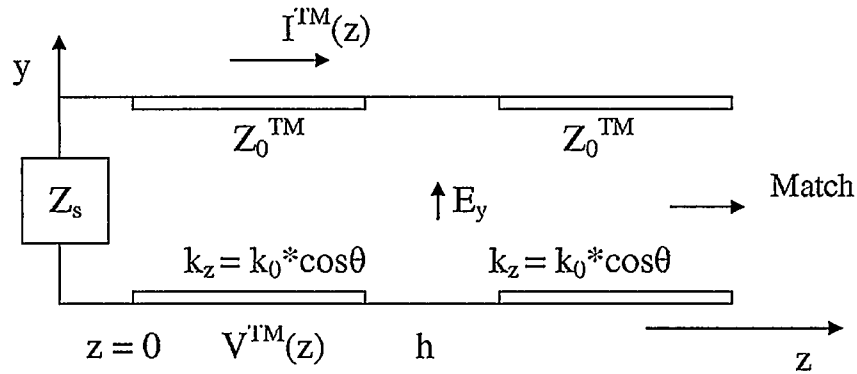


Figure 3.11: Equivalent network for the E-plane of the Hertzian dipole over an AIS.

With Equations (3.1) and (3.38), the transverse electric field, E_y at the dipole terminal, $z = h$, can be calculated,

$$\begin{aligned}
 \mathbf{E}_y^{TM}(z = h) &= V^{TM}(z = h) e^{TM}(x, y) \\
 &= V_0^+(0) \cos \theta (e^{jk_0 h \cos \theta} + \Gamma^{TM}(\theta) e^{-jk_0 h \cos \theta}) \frac{e^{-jk_y y}}{2\pi} \hat{\mathbf{y}}
 \end{aligned} \tag{3.57}$$

where $V_0^+(0)$ is the incident voltage at $z = 0$, and $\Gamma^{TM}(\theta)$ is the reflection coefficient of the TM incident wave measured at the AIS surface. Therefore, the normalized E-plane pattern is,

$$|E_\theta(\theta)| = |E_y^{TM}(z = h)| = |\cos \theta (e^{jk_0 h \cos \theta} + \Gamma^{TM}(\theta) e^{-jk_0 h \cos \theta})|, \quad (3.58)$$

with,

$$\Gamma^{TM}(\theta) = \frac{Z_s(\theta) - Z_0^{TM}(\theta)}{Z_s(\theta) + Z_0^{TM}(\theta)}. \quad (3.59)$$

3.3.4 Far-field Model

It is seen that Equation (3.55) and (3.58), derived using the receiving method, are the same as far-field Equations (3.52) and (3.53), calculated with the transmitting method. This is because both methods are analytical techniques and use the same assumption, (e.g. the AIS can be modeled as an impedance surface). We rewrite these pattern equations,

$$|E_\phi(\theta)| = |e^{jk_0 h \cos \theta} + \Gamma^{TE}(\theta) e^{-jk_0 h \cos \theta}|, \quad (3.60)$$

$$|E_\theta(\theta)| = |\cos \theta (e^{jk_0 h \cos \theta} + \Gamma^{TM}(\theta) e^{-jk_0 h \cos \theta})|, \quad (3.61)$$

and refer to them as our far-field model for the Hertzian dipole above an AIS surface. $\Gamma^{TE}(\theta)$ and $\Gamma^{TM}(\theta)$ are TE and TM plane wave reflection coefficients measured at the AIS surface.

As discussed in Chapter 2, the relationship between the far-field patterns of an antenna above an AIS surface and the plane wave reflection coefficients of the AIS were not clear. Now, with our far-field model, it is obvious that the far-field patterns of the Hertzian dipole above an AIS can be directly computed from the plane wave reflection coefficients using two simple equations. Since these far-field model equations, Equation (3.60) and (3.61), are derived analytically, they can be expected to be quite accurate for AIS with small periodicity compared to free space wavelength. In both the transmitting and receiving

methods, the AIS surface is modeled as an impedance surface. This means that all higher-order modes, including surface waves and evanescent waves excited or reflected near the AIS, are ignored. The effect of ignoring these higher-order modes is discussed in the next section (section 3.4.5).

3.4 Pattern Comparison

In this section, the accuracy of our far-field model is tested by comparing the far-field patterns calculated from Equations (3.60) and (3.61) with full-wave simulation results for two popular AIS, a patch AIS and a Jerusalem cross AIS. The dimensions of both AIS are given in section 3.4.1. In order to compute the far-field patterns using Equations (3.60) and (3.61), we need plane wave reflection coefficients, $\Gamma^{TE}(\theta)$ and $\Gamma^{TM}(\theta)$. Here, $\Gamma^{TE}(\theta)$ and $\Gamma^{TM}(\theta)$ are obtained from a full-wave simulator Ansoft HFSS. The HFSS simulation setup is described in section 3.4.2. To test our far-field model equations, the far-field patterns are also obtained from another full-wave simulator FEKO. These patterns from FEKO form the benchmark for the computed patterns. The FEKO simulation setup is discussed in section 3.4.3. Finally, in section 3.4.4, the far-field pattern obtained from our far-field model is compared with FEKO full-wave simulation results, and pattern results obtained from two other far-field models in [22] and [3]. Our far-field model computes the far-field patterns quite accurately except the H-plane patterns at the AIS resonant frequency. This error is analyzed in section 3.4.5.

3.4.1 AIS Selection

A patch AIS and a Jerusalem cross AIS designed by Akhoondzadeh-Asl et al. [2] are chosen for pattern comparison. Both AIS structures have the same dielectric thickness (3 mm) and dielectric constants ($\epsilon_r = 2.2$). The dimensions of each AIS are selected with a resonant frequency of 7.7 GHz in mind. As a result, the cell size of the patch AIS (7 mm) is

slightly larger than that of the Jerusalem cross AIS (5.8 mm). Dimensions of the patch and Jerusalem cross unit cell are shown in Figure 3.12. As was done in [2], a Hertzian dipole is placed 2 mm above each AIS surface.

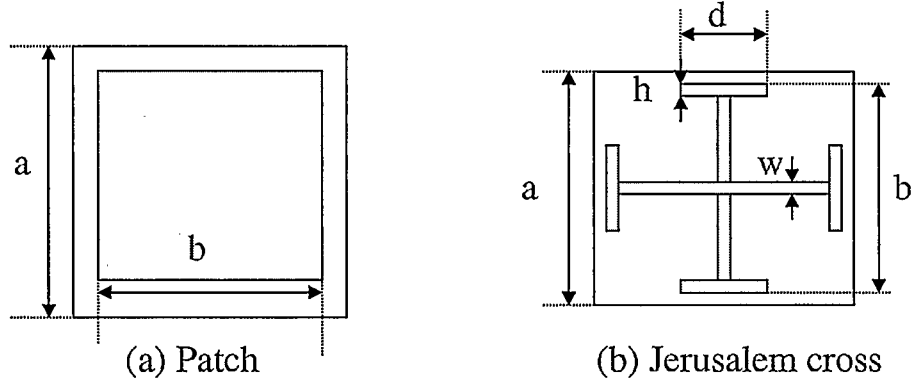


Figure 3.12: The dimensions of the Patch and Jerusalem cross unit cell. (a) $a = 7$ mm, $b = 6$ mm. (b) $a = 5.8$ mm, $b = 5.4$ mm, $h = 0.4$ mm, $w = 0.4$ mm, $d = 2.6$ mm. For both AIS, the dielectric thickness is $d = 3$ mm, and the relative permittivity is $\epsilon = 2.2$. [2]

3.4.2 Obtaining Reflection Coefficients for the Far-field Computation

In order to use our far-field model (Equations (3.60) and (3.61)), the plane wave reflection coefficients at the AIS top surface, $\Gamma^{TE}(\theta)$ and $\Gamma^{TM}(\theta)$, are required. These are obtained using the commercial full-wave simulator, Ansoft HFSS. Figure 3.13 shows the HFSS simulation setup. A unit cell of the patch or Jerusalem cross AIS is surrounded by periodic boundary conditions (PBC) which models an infinite AIS structure [40]. A perfect matching layer (PML) boundary is placed at the top of the simulation space to properly absorb reflections from the AIS [41, 42]. A TE or TM incident plane wave at an angle of θ is applied to the AIS. To obtain $\Gamma(\theta)$, the phase of the scattered electric fields at five testing points are measured (see Figure 3.13). From these we subtract reference phases to obtain the phase shift of $\Gamma(\theta)$. The reference phases are obtained in separate simulations, shown on the right hand side of Figure 3.13. The setup is exactly the same as that of the AIS simulation except that the unit cell is a Perfect Electric Conductor (PEC) placed at the

that they are both approximately one free space wavelength at the lowest test frequency, 4 GHz ($\lambda_0 = 75$ mm). The top view of the patch AIS in the FEKO simulation is shown in Figure 3.14. The plane on the bottom is an electric conductor (PEC); the middle area represents the dielectric slab, and the squares are the metal patch array. Note that both the electric conductor and the dielectric slab shown in Figure 3.14 are infinite in size. The dipole is placed in the center of the patch array. Since the patch array and Jerusalem cross array used in FEKO simulations are finite, we expect some difference between the computed patterns and the simulation results and this difference should decrease by increasing the array size. This is discussed in section 3.4.5.

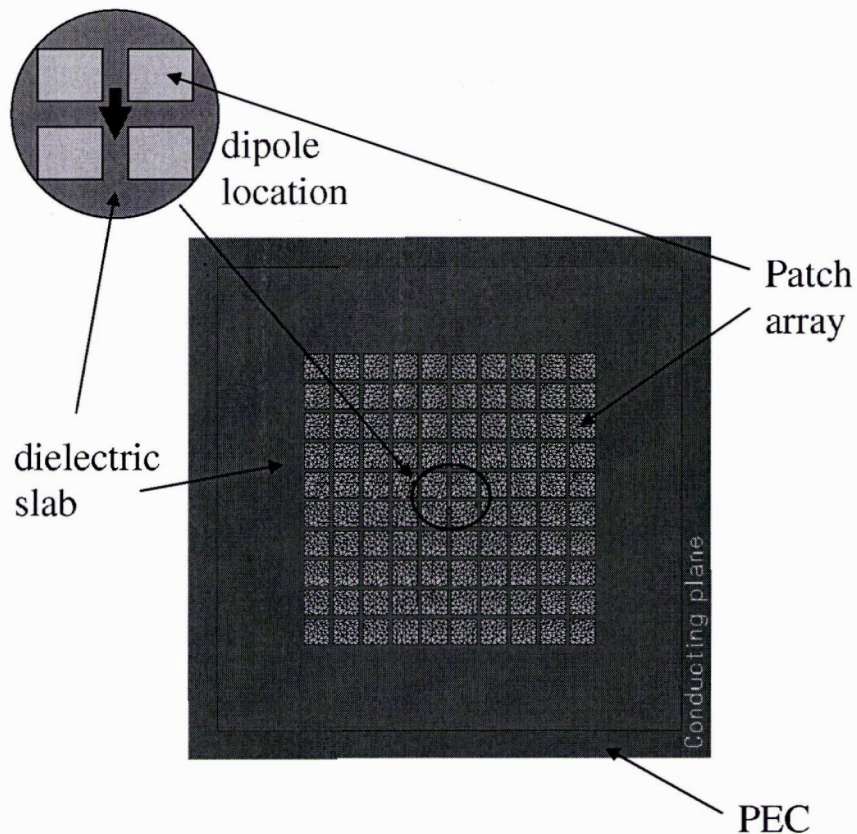


Figure 3.14: Top view of the FEKO simulation setup for a patch AIS with 10 X 10 patch array.

3.4.4 Pattern Comparison Results

Pattern comparison results are shown in this section. At first, the far-field patterns computed using our far-field model are compared with FEKO simulation results. Then, our far-field model is compared with the other two far-field models given in [22] and [3]. In the end, the error analysis is provided.

Comparing with FEKO Simulations

Comparisons are made at 4 GHz, 5.5 GHz, and 7.7 GHz. As mentioned before, 7.7 GHz is designed to be the resonant frequency of the patch AIS and the Jerusalem cross AIS. According to Sarabandi et al. [25], when a dipole is close to an AIS surface, it is beneficial for the dipole to operate at the frequency where the mutual coupling between the dipole and its image is minimum. This is because the dipole has the largest S11 bandwidth at this frequency. To find this frequency, it was suggested in [25] that the plane wave reflection phase at normal incidence of the AIS is about 145°. Following this rule, we found that this frequency is 4 GHz for the patch AIS and the Jerusalem cross AIS. Therefore, it is important to test the far-field model at 4 GHz for both AIS. Moreover, a middle frequency point, 5.5 GHz, is chosen to show any trends in the far-field model. Figure 3.15 to 3.17 and Figure 3.18 to 3.20 show the comparison results of the Patch AIS and the Jerusalem cross AIS respectively. Comparison of the Half-power Bandwidth (HPBW) between the calculated and simulation patterns of the patch and Jerusalem cross AIS are also shown in Tables 3.1 and 3.2. The error percentage is computed by $\frac{|Model-FEKO|}{FEKO} \times 100\%$, where *Model* and *FEKO* denotes HPBW obtained using our far-field model (given by Equations (3.60) and (3.61)) and obtained from FEKO full-wave simulation results, respectively.

It is clear from Figures 3.15 to 3.20 and Tables 3.1 and 3.2, that the H- and E-plane far-field patterns calculated by our far-field model match well with the full-wave simulation results for the patch AIS and the Jerusalem cross AIS, except for the H-plane at 7.7 GHz, the AIS resonant frequency. This indicates that with accurate reflection coefficients, $\Gamma(\theta)$,

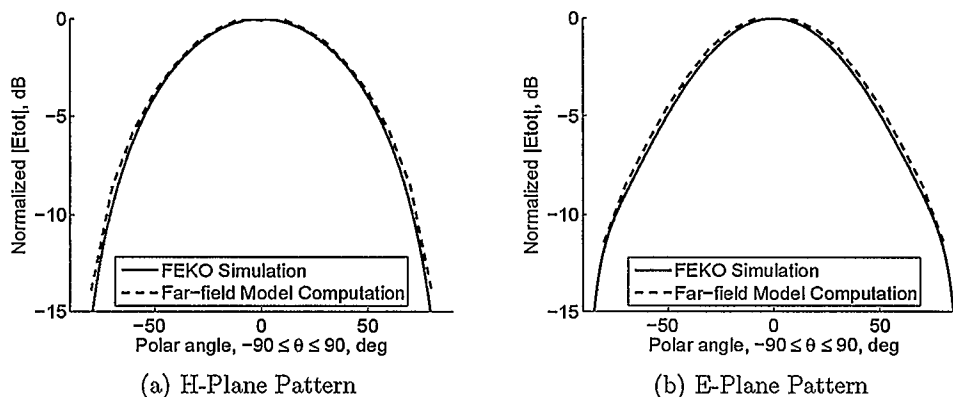


Figure 3.15: Far-field pattern comparison between the far-field model and FEKO simulation of a Hertzian dipole over a Patch AIS (10 X 10 array) at 4 GHz.

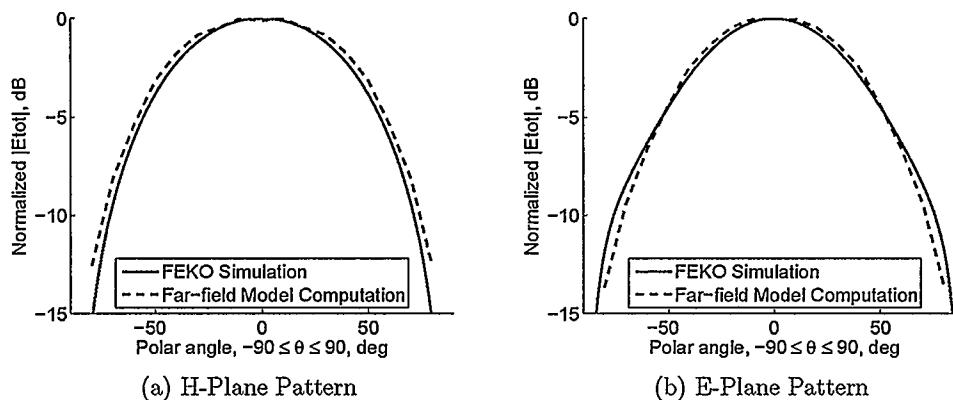


Figure 3.16: Far-field pattern comparison between the far-field model and FEKO simulation of a Hertzian dipole over a Patch AIS (10 X 10 array) at 5.5 GHz.

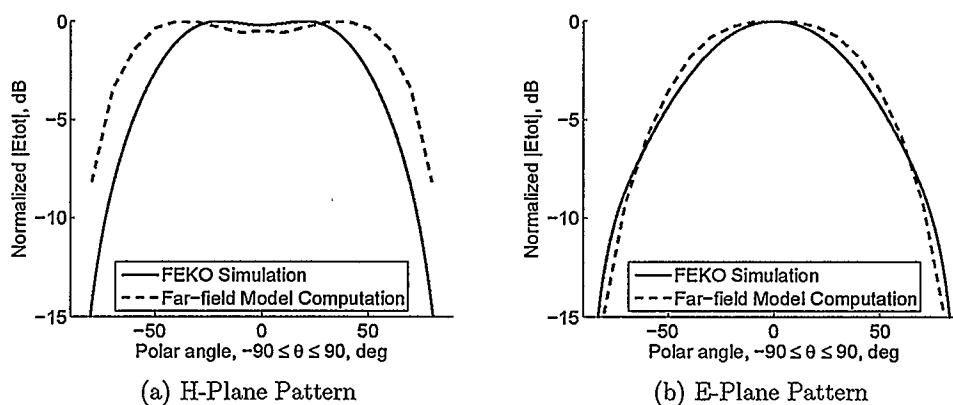


Figure 3.17: Far-field pattern comparison between the far-field model and FEKO simulation of a Hertzian dipole over a Patch AIS (10 X 10 array) at 7.7 GHz.

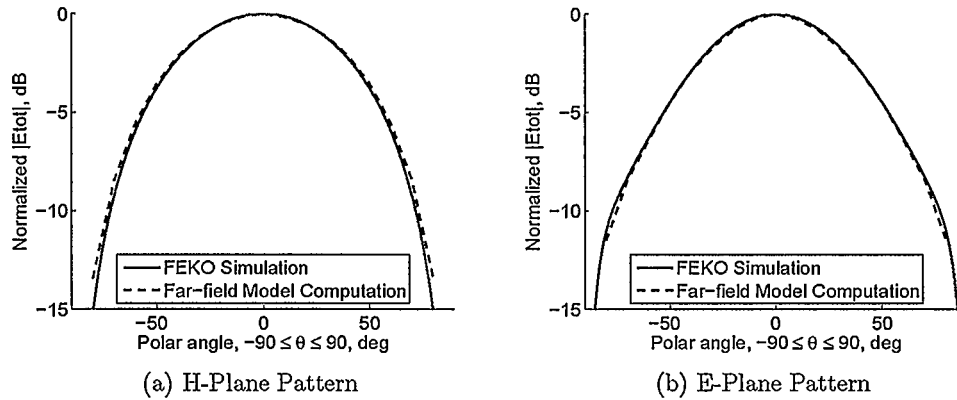


Figure 3.18: Far-field pattern comparison between the far-field model and FEKO simulation of a Hertzian dipole over a Jerusalem cross AIS (12 X 12 array) at 4 GHz.

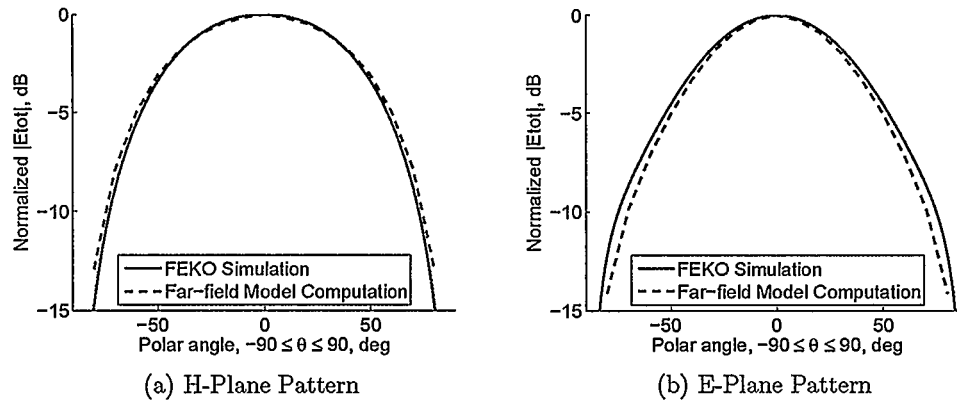


Figure 3.19: Far-field pattern comparison between the far-field model and FEKO simulation of a Hertzian dipole over a Jerusalem cross AIS (12 X 12 array) at 5.5 GHz.

our model can predict the far-field patterns of a Hertzian dipole above an AIS surface with good accuracy, especially at frequencies below the resonance. Due to the complexity of the AIS surfaces, using our far-field model greatly reduces computation time while still providing accurate results.

Comparing with the Constant Γ Far-field Model

Since our far-field model uses accurate reflection coefficients $\Gamma(\theta)$, it is more accurate than the models proposed in [22], which assumes a constant reflection coefficients over the incident angle. Here, we refer to this model in [22] as the constant Γ model. To show

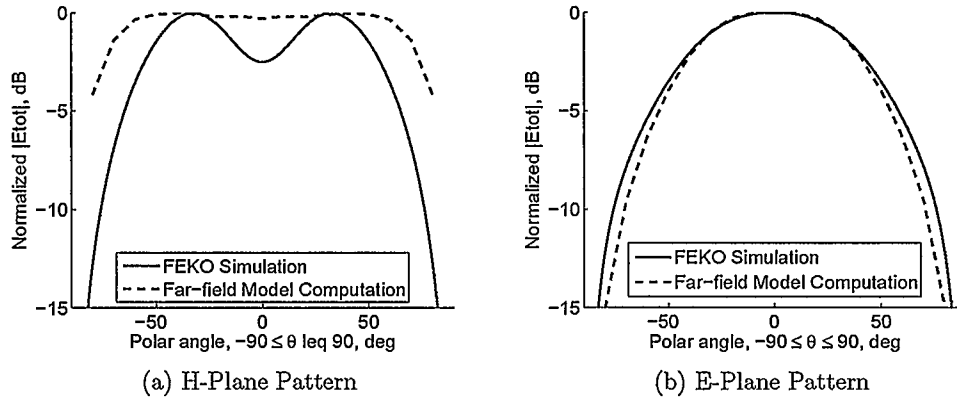


Figure 3.20: Far-field pattern comparison between the far-field model and FEKO simulation of a Hertzian dipole over a Jerusalem cross AIS (12 X 12 array) at 7.7 GHz.

Table 3.1: HPBW comparison between model and simulation for the patch AIS with 10 X 10 patch array.

HPBW (Degrees)	4 GHz		5.5 GHz		7.7 GHz	
	H	E	H	E	H	E
FEKO	88.2	77.2	90.2	81	104.54	83.58
Model	89.6	81.2	97.8	85.6	136	93.6
Error (%)	1.59	5.18	8.43	5.68	30.09	11.99

Table 3.2: HPBW comparison between model and simulation for the Jerusalem cross AIS with 12 X 12 array.

HPBW (Degrees)	4 GHz		5.5 GHz		7.7 GHz	
	H	E	H	E	H	E
FEKO	90.6	81.18	95.56	81.1	115.5	93.44
Model	92.2	80.98	98.76	76.1	151.6	89.1
Error (%)	1.77	0.25	3.35	6.17	31.26	4.64

this, the H- and E-plane far-field patterns computed from our far-field model and from the constant Γ model are compared with FEKO simulation results for the patch AIS with 10 X 10 array (Figures 3.21 to 3.23) and the Jerusalem cross AIS with 12 X 12 array (Figures 3.24 to 3.26).

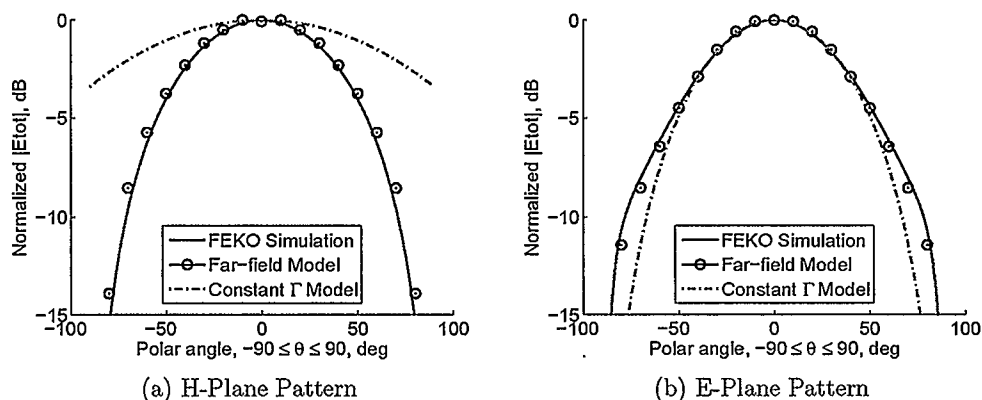


Figure 3.21: Comparison of the far-field patterns computed from our far-field model and the constant Γ model with FEKO simulation results for a Hertzian dipole above a patch AIS (10 X 10 array) at 4 GHz.

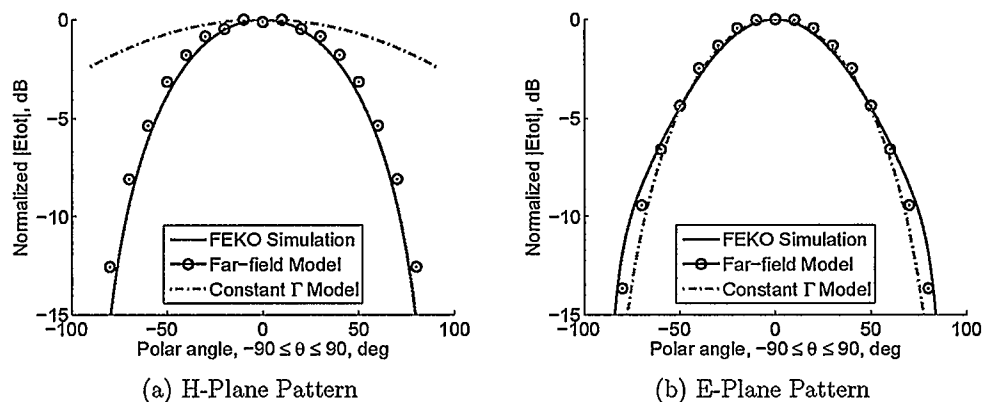


Figure 3.22: Comparison of the far-field patterns computed from our far-field model and the constant Γ model with FEKO simulation results for a Hertzian dipole above a patch AIS (10 X 10 array) at 5.5 GHz.

Clearly, our far-field model is much more accurate predicting the H-plane patterns of the Hertzian dipole than the constant Γ model at all test frequencies in the case of both the

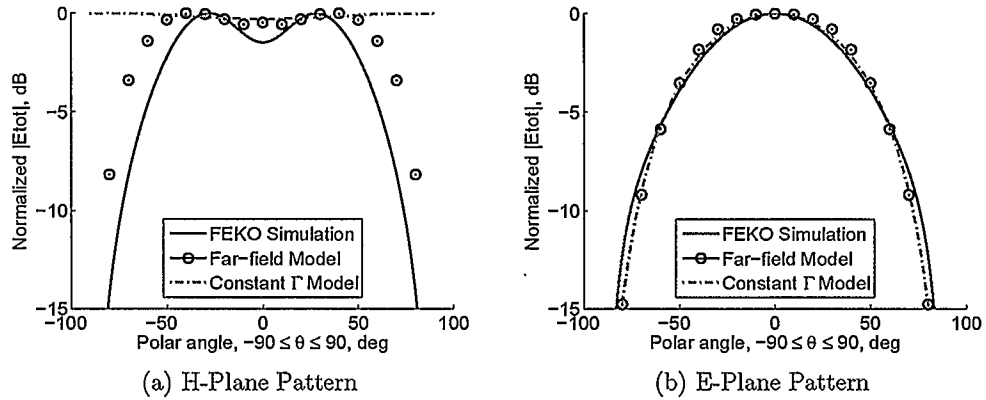


Figure 3.23: Comparison of the far-field patterns computed from our far-field model and the constant Γ model with FEKO simulation results for a Hertzian dipole above a patch AIS (10 X 10 array) at 7.7 GHz.

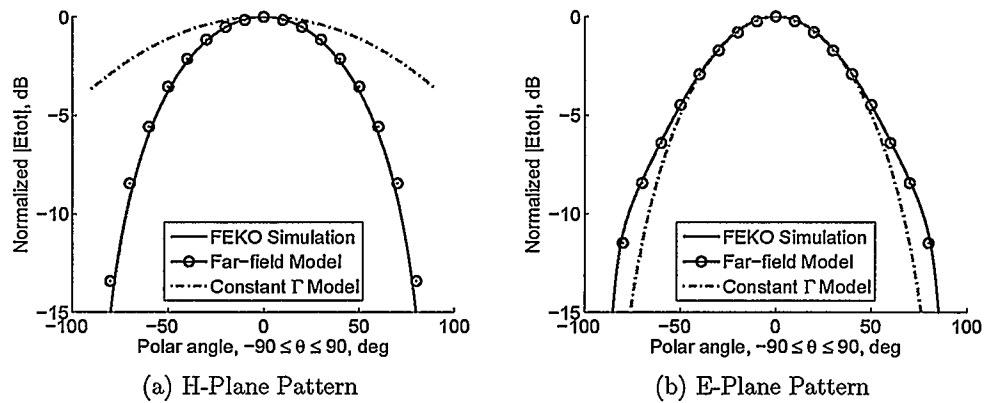


Figure 3.24: Comparison of the far-field patterns computed from our far-field model and the constant Γ model with FEKO simulation results for a Hertzian dipole above a Jerusalem cross AIS (12 X 12 array) at 4 GHz.

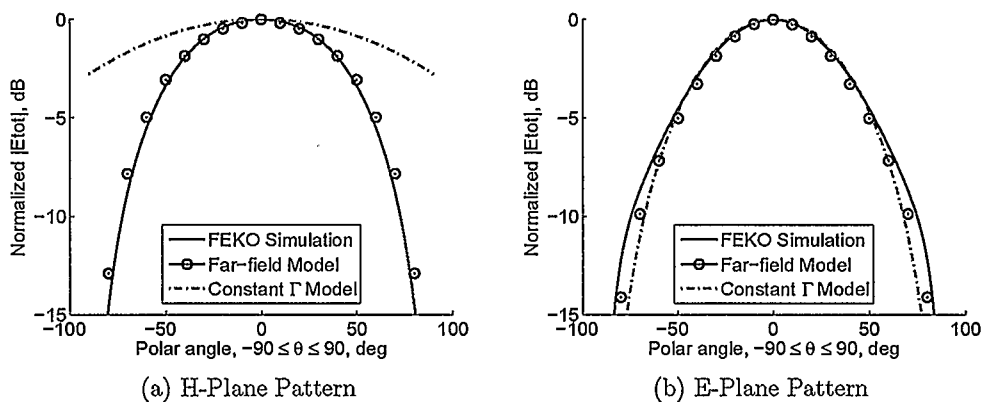


Figure 3.25: Comparison of the far-field patterns computed from our far-field model and the constant Γ model with FEKO simulation results for a Hertzian dipole above a Jerusalem cross AIS (12 X 12 array) at 5.5 GHz.

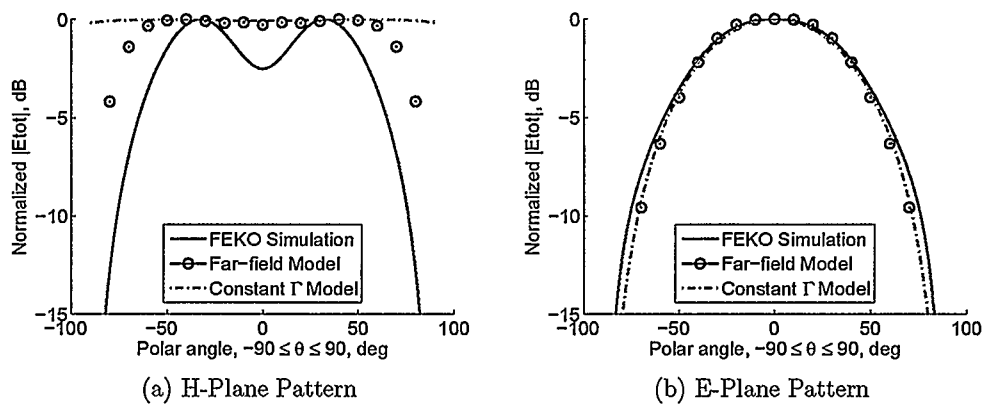


Figure 3.26: Comparison of the far-field patterns computed from our far-field model and the constant Γ model with FEKO simulation results for a Hertzian dipole above a Jerusalem cross AIS (12 X 12 array) at 7.7 GHz.

patch AIS and the Jerusalem cross AIS. This is because the reflection coefficients, $\Gamma^{TE}(\theta)$, of both AIS are not a constant over the incident angle. On the E-plane, the constant Γ model seems to be quite accurate. However, this is not because $\Gamma^{TM}(\theta)$ of both AIS are invariant over the incident angle. Instead, this is effect of the $\cos\theta$ term in the E-plane pattern equation of the Hertzian dipole (see Equation (3.61)). When the polar angle θ approaches 90° , the $\cos\theta$ term goes to 0. This forces the E-plane patterns to approach 0 no matter whether $\Gamma^{TM}(\theta)$ is accurate or not.

Comparing with the Constant Z_s Far-field Model

In [3], the H-plane pattern of an infinite line current was derived by assuming that the equivalent impedance of the AIS does not change with the incident angle. We refer to this model as the constant Z_s model, where Z_s denotes the equivalent impedance of the AIS. Using the transmitting method, we can obtain the normalized H-plane far-field pattern equation for an infinite line source, which is the same as Equation (3.60). Thus, we can compare our far-field model, the constant Z_s model with FEKO simulation results. The comparison results for the patch AIS are shown in Figures 3.27(a) to 3.29(a) and those for the Jerusalem cross AIS are shown in Figures 3.27(b) to 3.29(b).

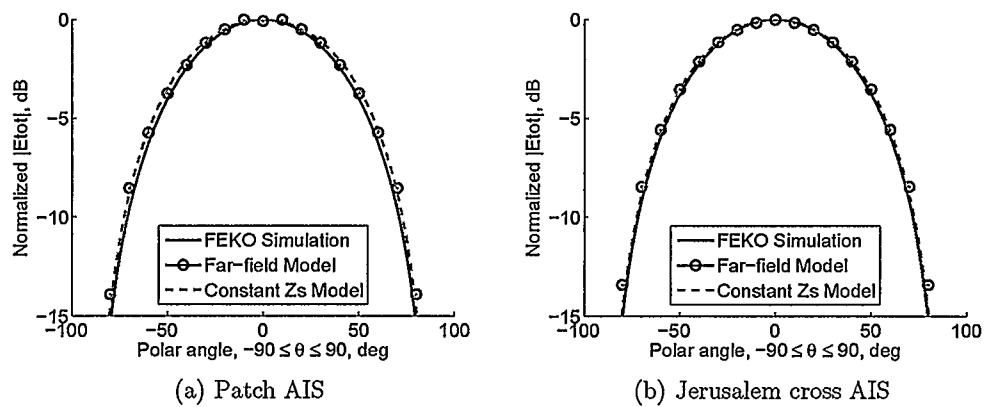


Figure 3.27: Comparison of the H-plane far-field patterns computed from our far-field model and the constant Z_s model [3] with FEKO simulation results for a Hertzian dipole above a patch AIS (10 X 10 array) and above a Jerusalem cross AIS (12 X 12 array) at 4 GHz.

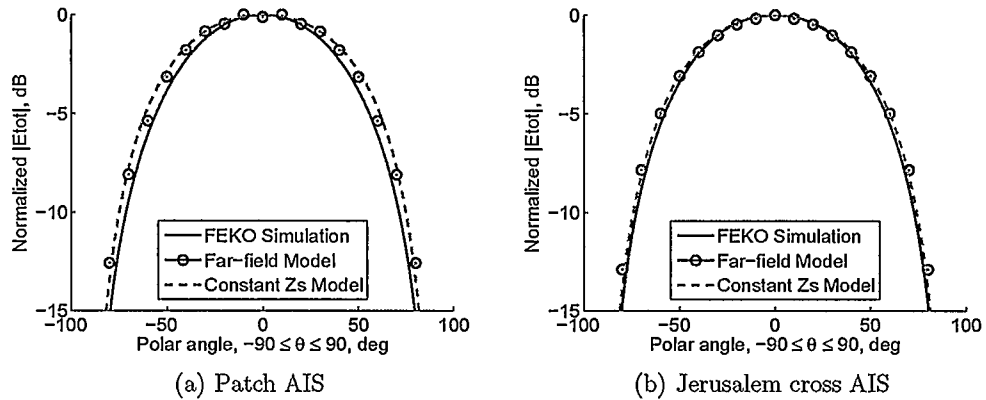


Figure 3.28: Comparison of the H-plane far-field patterns computed from our far-field model and the constant Z_s model [3] with FEKO simulation results for a Hertzian dipole above a patch AIS (10 X 10 array) and above a Jerusalem cross AIS (12 X 12 array) at 5.5 GHz.

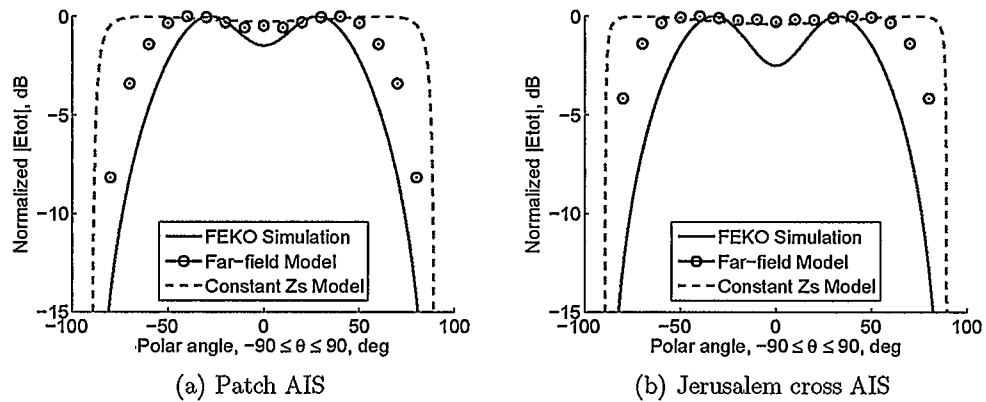


Figure 3.29: Comparison of the H-plane far-field patterns computed from our far-field model and the constant Z_s model [3] with FEKO simulation results for a Hertzian dipole above a patch AIS (10 X 10 array) and above a Jerusalem cross AIS (12 X 12 array) at 7.7 GHz.

It is seen that, at 4 GHz and 5.5 GHz, the constant Z_s model predicts the H-plane patterns of the Hertzian dipole as well as our far-field model. This is because the surface impedances of both the patch and Jerusalem cross AIS are almost invariant over the incident angle at these frequencies. However, at 7.7 GHz, it can be seen that our far-field model is much more accurate than the constant Z_s model, since the AIS surface impedances are no longer a constant over the incident angle.

3.4.5 Model Error Analysis

While the far-field patterns from our model were in close agreement with simulated results, there was some error, particularly in the H-plane at 7.7GHz, the resonant frequency of the AIS. There are two reasons for this error. First, the model assumes an infinite AIS while only a finite array on top of an infinite dielectric slab were simulated in FEKO. Second, the model ignores the higher-order modes excited on the AIS, while in FEKO all possible modes are captured. Interestingly, these higher-order modes, evanescent waves or surface waves, do not affect far-field patterns on an infinite structure, but due to the finite array size, some of these modes reach to the edge of the array and are able to influence far-field patterns by radiating into space. Therefore, by increasing array size in FEKO simulation, we expected that the computed H-plane pattern at 7.7 GHz match with FEKO simulation results better.

To verify this, the Hertzian dipole is simulated in FEKO at 7.7 GHz above a patch AIS with 14 X 14, 18 X 18, and 20 X 20 array, respectively. Then, we compare the computed H-plane far-field patterns at 7.7 GHz with these simulation results. The comparison results are shown in Figures 3.30 and 3.33, and the half-power bandwidth comparison is shown in Table 3.3.

Observing these comparison results, it is found that the error in the computed H-plane pattern at 7.7 GHz decreases when the array size is increased from 10 X 10 (70 mm) to 18 X 18 (126 mm). However, no benefit is gained by increasing the array from 18 X 18 (126 mm)

Table 3.3: HPBW comparison for the H-plane between model and simulation for the patch AIS with different array size.

HPBW (°)	10 X 10 array	14 X 14 array	18 X 18 array	20 X 20 array
FEKO	104.54	117.8	120	119.2
Model	136	136	136	136
Error (%)	30.09	15.45	13.33	14.09

to 20 X 20 (140 mm). This observation can be explained by analyzing the higher-order modes excited on the AIS surface at 7.7 GHz, the AIS resonant frequency.

As discussed before, the higher-order modes excited on the AIS surface are either evanescent waves or surface waves. Due to their different characteristics, we discuss them separately. Evanescent waves die out quickly away from Hertzian dipole. Therefore, when we increase the array size, less evanescent waves can reach to the edge of the array and affect far-field patterns. As a result, the computed far-field pattern using our model match better with simulation results. When the array is increased to a certain point that most evanescent modes die out, little or no benefit can be gained by continuing to increase the array size.

Unlike evanescent waves, surface waves propagate along the AIS top surface without attenuating. Therefore, no matter how large the array is, as long as it is finite, surface waves can radiate at the array edge and affect the far-field patterns. Below the AIS resonant frequency, only TM surface waves can be supported on the AIS, so no surface waves propagate on the H-plane of the Hertzian dipole (since only TE waves are excited). Above the AIS resonant frequency, however, TE surface waves can propagate on the H-plane of the Hertzian dipole. At 7.7 GHz, the resonant frequency of the patch AIS, the TE surface waves might have already started propagating, resulting in a gap between the computed and simulated H-plane pattern, which can not be removed simply by increasing the array size.

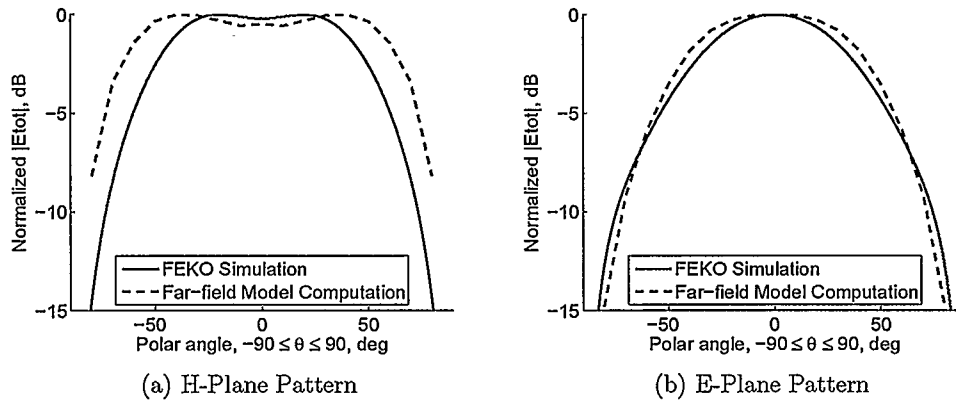


Figure 3.30: Far-field pattern comparison between the far-field model and FEKO simulation of a Hertzian dipole over a Patch AIS (10 X 10 array) at 7.7 GHz.

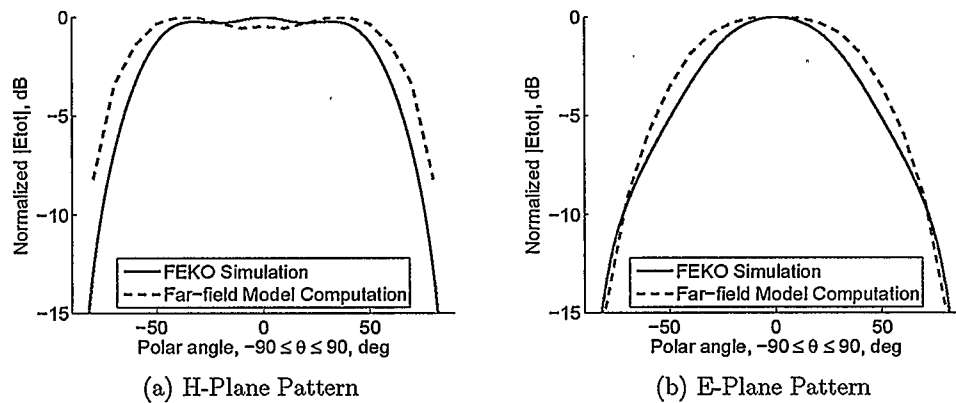


Figure 3.31: Far-field pattern comparison between the far-field model and FEKO simulation of a Hertzian dipole over a patch AIS (14 X 14 patch array) at 7.7 GHz.

3.5 Summary

In this chapter, H- and E-plane far-field patterns of a Hertzian dipole over an infinite AIS surface were derived using a transmitting and a receiving method, after modeling the AIS as an impedance surface and assuming that all higher order modes, (surface waves and evanescent waves), on the AIS can be ignored. Two simple equations were derived from both methods. These equations form the far-field model. With this model, the far-field patterns of the Hertzian dipole can be directly calculated from plane wave reflection

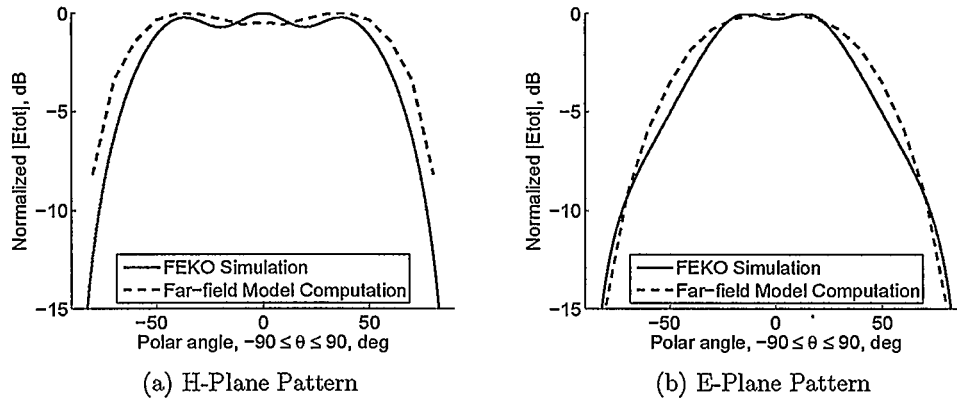


Figure 3.32: Far-field pattern comparison between the far-field model and FEKO simulation of a Hertzian dipole over a patch AIS (18 X 18 patch array) at 7.7 GHz.

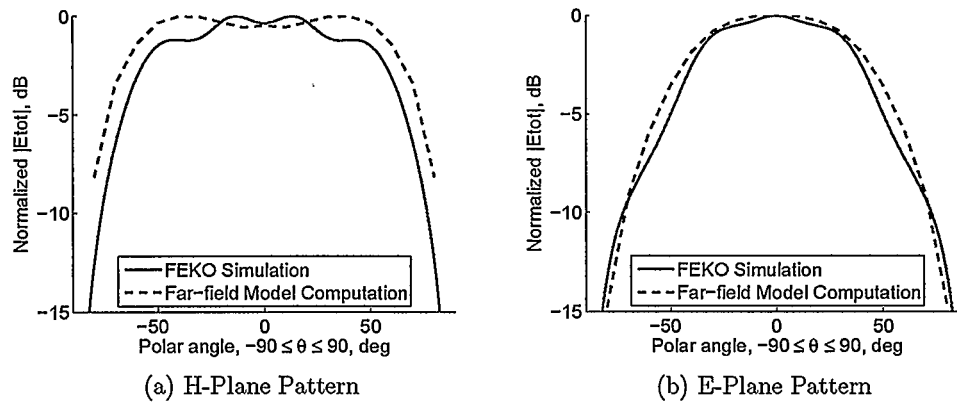


Figure 3.33: Far-field pattern comparison between the far-field model and FEKO simulation of a Hertzian dipole over a patch AIS (20 X 20 patch array) at 7.7 GHz.

coefficients measured at the AIS surface. This way, the connection between the far-field patterns of the dipole and plane wave reflection coefficients of a complicated AIS is clear.

To verify the far-field, H- and E-plane patterns of a patch AIS and a Jerusalem cross AIS were computed and compared with full-wave simulation results from FEKO. It was shown that, for AIS with small periodicity compared to free space wavelength, the model provides quite accurate far-field patterns of the dipole, except for H-plane patterns at the AIS resonant frequency. Compared to other far-field models in the literature, our far-field

model was shown to give more accurate pattern results. The errors in the H-plane patterns at the AIS resonance are also discussed.

Chapter 4

Grid Impedance Modeling

With the far-field model introduced in the previous chapter, the H- and E-plane far-field patterns of a Hertzian dipole antenna over an AIS surface can be directly calculated from the TE and TM plane wave reflection coefficients, $\Gamma(\theta)$. One way to obtain $\Gamma(\theta)$ is from full-wave simulations. This method provides accurate $\Gamma(\theta)$ results but is time-consuming. Alternatively, we can derive a model of the AIS and compute $\Gamma(\theta)$ directly. For example, in [22], it is assumed that $\Gamma(\theta)$ is a constant over the incident angle, while in [3, 7, 25], the AIS is assumed to have a constant surface impedance. Another method uses a simple parallel circuit [23, 26] of the so-called grid impedance and the equivalent impedance of the grounded dielectric slab for the calculation of $\Gamma(\theta)$. The grid impedance is obtained with a $\cos^2 \theta$ model in [26] (discussed in section 4.1). In this chapter, the same parallel circuit as in [23, 26] and a different grid impedance model, the constant grid impedance model, are used to calculate $\Gamma(\theta)$ of the patch and Jerusalem cross AIS.

This chapter is organized as follows. First, the circuit model and the constant grid impedance model are introduced in section 4.1. The constant grid impedance model is evaluated with respect to the accuracy of the grid impedance and the resulting reflection coefficients. It is shown that the constant grid impedance model, although simple, models the grid impedance and reflection coefficients of the patch and the Jerusalem cross AIS introduced in Chapter 3 reasonably well. However, the computed $\Gamma^{TE}(\theta)$ of the patch AIS have some errors at the AIS resonant frequencies. It is shown, in section 4.2, that this error is caused by a phenomenon referred to as circuit model sensitivity. To evaluate this phenomenon, the circuit model is analyzed in detail in section 4.3. Due to the circuit model sensitivity, a more accurate grid impedance model is required to calculate $\Gamma^{TE}(\theta)$ of the

patch AIS near its resonant frequency. For this reason, a modified constant grid impedance model is proposed for the patch AIS for the TE incidence in section 4.4. It is shown that this modified model computes both the grid impedances of a variety of patch AIS quite accurately. Section 4.5 summarizes this chapter.

4.1 The Constant Grid Impedance Model

The parallel circuit used in [26] to model the AIS and calculate the plane wave reflection coefficients, $\Gamma(\theta)$, is shown in Figure 4.1. In the circuit, a grid impedance, Z_g , models the periodic metal array, (e.g. the patch array or the Jerusalem array), of the AIS structure, and can be obtained from full-wave simulations or some circuit modeling [7, 25]. $Z_{in}(\theta)$ is the equivalent impedance of the grounded dielectric. $Z_0(\theta)$ and k_z are the characteristic impedance and wave number of the equivalent transmission line that models the free space above the AIS surface. As shown in Figure 4.1, this transmission line is in z direction.

Plane wave reflection coefficients, $\Gamma(\theta)$, of the AIS can be calculated with,

$$Z_s(\theta) = \frac{Z_{in}(\theta)Z_g(\theta)}{Z_{in}(\theta) + Z_g(\theta)}, \quad \Gamma(\theta) = \frac{Z_s(\theta) - Z_0(\theta)}{Z_s(\theta) + Z_0(\theta)}, \quad (4.1)$$

where $Z_s(\theta)$ is the surface impedance of the AIS. Since $Z_0(\theta)$ is the characteristic impedance of the free space equivalent transmission line, Equations (3.11) and (3.12) introduced in the method of modal expansion can be applied to obtain,

$$Z_0^{TE}(\theta) = Z_0 / \cos \theta, \quad Z_0^{TM}(\theta) = Z_0 \cos \theta, \quad (4.2)$$

for all incident angles. Here, $Z_0 = \sqrt{\mu_0/\epsilon_0}$ is the intrinsic impedance of free space; ϵ_0 and μ_0 are the free space permittivity and permeability, respectively. $Z_{in}(\theta)$, the equivalent impedance of the grounded dielectric, can be obtained in a similar way. By modeling the grounded dielectric as an equivalent transmission line that has a short load, a length of d , (e.g. the dielectric thickness), and a dielectric material with relative permittivity ϵ_r and

free space permeability μ_0 , it is easy to obtain,

$$Z_{in}^{TE}(\theta) = j \frac{Z_d}{\cos \alpha} \tan(k_d d \cos \alpha), \quad Z_{in}^{TM}(\theta) = j Z_d \cos \alpha \tan(k_d d \cos \alpha), \quad (4.3)$$

where,

$$Z_d = Z_0 / \sqrt{\epsilon_r}, \quad k_d = k_0 \sqrt{\epsilon_r}. \quad (4.4)$$

Here, $k_0 = \omega / \sqrt{\mu_0 \epsilon_0}$ is the wave number in free space. The incident angle, θ , and the transmitted angle in the dielectric, α , are measured from the AIS surface normal. According to Snell's law [43], θ and α , as indicated in Figure 4.1, are related by

$$\sin \theta = \sqrt{\epsilon_r} \sin \alpha. \quad (4.5)$$

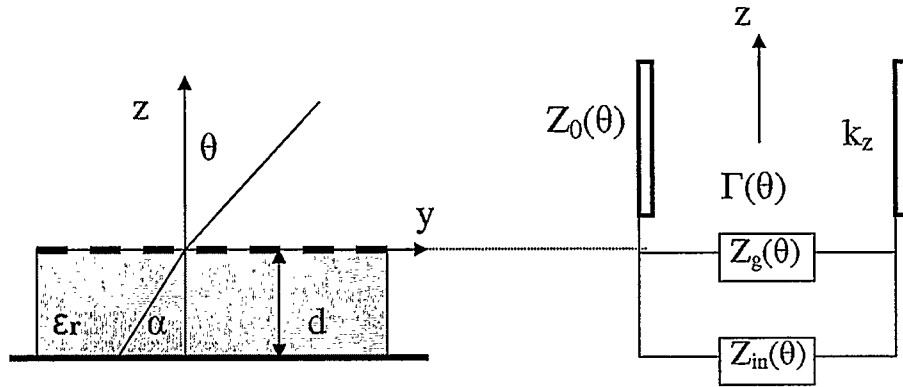


Figure 4.1: The circuit model for an AIS structure.

In general, the grid impedance of an AIS varies with the incident angle and plane wave polarization. In [27], however, the grid impedance was assumed to be a constant over the incident angle for the leaky wave antenna analysis. If this assumption can be applied to AIS structures, reflection coefficient computations of the AIS can be made much more efficient. In order to verify this first-order assumption, we use it in this thesis for the patch and Jerusalem cross AIS, and refer to it as the constant grid impedance model for the AIS. This assumption is described in Equation (4.6),

$$Z_g^{TE}(\theta) = Z_g(0), \quad Z_g^{TM}(\theta) = Z_g(0). \quad (4.6)$$

Another grid impedance model was proposed in [26], where the grid impedance was suggested to be proportional to the averaged current induced in the periodic metal array. The grid impedance of the patch AIS was given as [26],

$$Z_g^{TE}(\theta) = \frac{Z_g(0)}{\cos^2 \theta}, \quad Z_g^{TM}(\theta) = Z_g(0), \quad (4.7)$$

and that of the Jerusalem cross AIS as,

$$Z_g^{TE}(\theta) = Z_g(0), \quad Z_g^{TM}(\theta) = Z_g(0) \cos^2(\theta). \quad (4.8)$$

In [26], Equation (4.8) and (4.7) were obtained by solving the fields of an infinite array of infinite long wires. Because of the $\cos^2 \theta$ term in Equations (4.7) and (4.8), we refer to this model as the $\cos^2 \theta$ model in this thesis. This model is the same as the constant grid impedance model with TM incidence for the patch AIS, and with TE incidence for the Jerusalem cross AIS.

In the following, the accuracy of the constant grid impedance model is tested. In section 4.1.1, grid impedance of the patch and Jerusalem cross AIS, obtained using this model, are compared with full-wave simulation results and results of the grid impedance model in [26], the $\cos^2 \theta$ model. In section 4.1.2, reflection coefficients of both AIS are computed using the constant grid impedance model and the results are again compared with full-wave simulation results.

4.1.1 Grid Impedance Test

In this section, the grid impedance of the patch and Jerusalem cross AIS (with single unit cell dimensions shown in Figure 4.2) are obtained using the constant grid impedance model and the $\cos^2 \theta$ model [26], and compared with results obtained from the full-wave simulator, Ansoft HFSS. The simulation results form the benchmark for the model results.

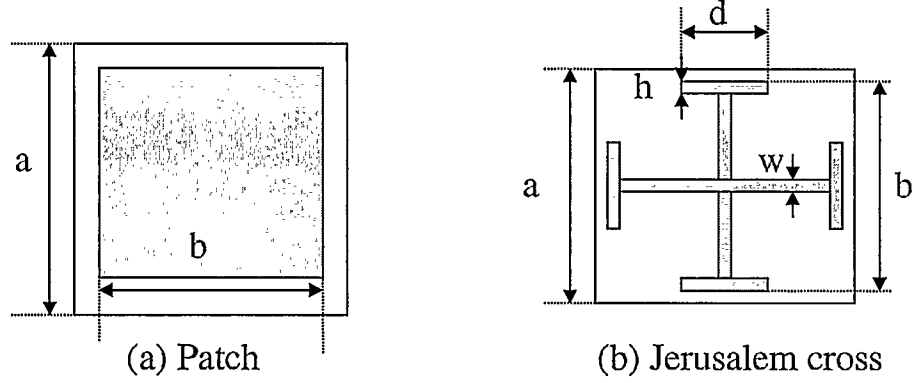


Figure 4.2: The dimensions of a single patch and Jerusalem cross unit cell. (a) patch: $a = 7$ mm, $b = 6$ mm. (b) Jerusalem cross: $a = 5.8$ mm, $b = 5.4$ mm, $h = 0.4$ mm, $w = 0.4$ mm, $d = 2.6$ mm.

Obtaining Model Results

To calculate $Z_g(\theta)$ for both the constant grid impedance model and the $\cos^2\theta$ model, the grid impedance at normal incidence, $Z_g(0)$, is obtained from an HFSS simulation. The simulation setup is shown in Figure 4.3. To simulate an infinite patch or Jerusalem cross array illuminated with a plane wave incident at the normal direction, a single patch or Jerusalem cross unit cell (see Figure 4.2) is surrounded by two Perfect Electric Conductor (PEC) boundaries in the x-direction and two Perfect Magnetic Conductor (PMC) boundaries in the y-direction, shown in Figure 4.3. To satisfy the boundary conditions, the electric field, \mathbf{E} , has to be perpendicular to the PEC boundaries, while the magnetic field, \mathbf{H} , has to be perpendicular to the PMC boundaries. The presence of the dielectric slab in the AIS influences the grid impedance [23], so the unit cell is backed by a dielectric half-space in the HFSS simulations. Wave ports are used to produce a normally incident plane wave and compute the reflection coefficient, $\Gamma_{grid}(0)$, of the patch and Jerusalem cross array.

With $\Gamma_{grid}(0)$, the grid impedance at normal incidence, $Z_g(0)$, can be calculated with

$$Z_{s,grid}(0) = Z_0(0) \frac{1 + \Gamma_{grid}(0)}{1 - \Gamma_{grid}(0)}, \quad Z_g(0) = \frac{Z_d(0)Z_{s,grid}(0)}{Z_d(0) - Z_{s,grid}(0)}, \quad (4.9)$$

where $Z_d(0) = Z_0(0)/\sqrt{\epsilon_r}$ and ϵ_r is the relative permittivity of the dielectric. Application of Equation (4.6) provides $Z_g(\theta)$ for the constant grid impedance model. Similarly, grid impedance results of the $\cos^2 \theta$ model can be obtained with Equations (4.7) and (4.8).

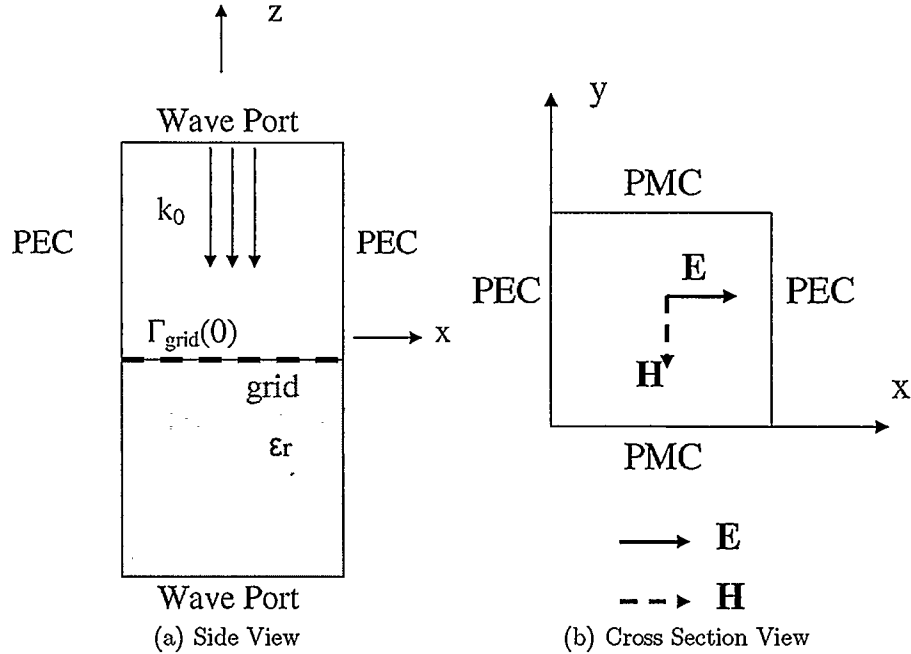


Figure 4.3: HFSS simulation setup for grid impedance calculation at normal incidence.

Obtaining Simulation Results

To evaluate the two grid impedance models, we need to obtain the grid impedance for oblique incident plane waves in HFSS full-wave simulations as well. In order for proper computation of the infinite patch and Jerusalem cross array at oblique incidence, another HFSS simulation setup is used. This simulation is setup as shown in Figure 4.4(a). Here, the patch or Jerusalem cross unit cell is surrounded by periodic boundaries (PBC) to model an infinite structure. The unit cell is backed by a dielectric half-space to include interactions between the array and the dielectric slab. Perfect Matching Layer boundaries (PML) above and below the simulation space are used to absorb reflections. In order to compute $\Gamma_{grid}(\theta)$, total electric fields are obtained at five testing points in this simulation

as well as a reference simulation. The reference simulation setup is shown in Figure 4.4(b). In the reference simulation, there is only air between the two PML boundaries. More than one testing point was used to ensure the accuracy of the simulation results. From the simulations, the scattered fields of the patch or Jerusalem cross array can be obtained from,

$$E_{grid}^{scat}(\theta) = \frac{E_{grid}^{tot}(\theta) - E_{ref}^{tot}(\theta)}{|E_{ref}^{tot}(\theta)|}. \quad (4.10)$$

Then the amplitude and phase of the reflection coefficients can be calculated with,

$$|\Gamma_{grid}(\theta)| = \frac{\sum^5 (|E_{grid}^{scat}(\theta)|)}{5} \quad (4.11)$$

$$\angle \Gamma_{grid}(\theta) = \frac{\sum^5 (\angle E_{grid}^{scat}(\theta) - \angle E_{ref}^{tot}(\theta) + 2k_0 z \cos \theta)}{5}, \quad (4.12)$$

where k_0 is the free space propagation constant and z is the distance between the testing point and the patch (or Jerusalem cross) array. With $\Gamma_{grid}(\theta)$, $Z_g(\theta)$ can be calculated with,

$$Z_{s,grid}(\theta) = Z_0(\theta) \frac{1 + \Gamma_{grid}(\theta)}{1 - \Gamma_{grid}(\theta)}, \quad Z_g(\theta) = \frac{Z_d(\theta) Z_{s,grid}(\theta)}{Z_d(\theta) - Z_{s,grid}(\theta)}, \quad (4.13)$$

where $Z_0(\theta)$ is calculated from Equations (4.2) and $Z_d(\theta) = Z_0(\theta)/\sqrt{\epsilon_r}$. These grid impedance results, simulated in HFSS, form the benchmark for the constant grid impedance model and the $\cos^2 \theta$ model.

As discussed, the grid impedance of the patch and the Jerusalem cross AIS are computed with the constant grid impedance model and the $\cos^2 \theta$ model. The results are compared with the HFSS simulations at 4 GHz, 5.5 GHz, and 7.7 GHz for both TE and TM incident waves. Figures 4.5 to 4.7 are the grid impedance comparison results for the patch AIS and Figures 4.8 to 4.10 show those of the Jerusalem cross AIS. Since the patch and Jerusalem cross AIS considered in this thesis are lossless, their grid impedance should be only reactive, that is, the real part of Z_g should be equal to 0. However, Z_g obtained from HFSS simulations (shown in Figure 4.4) usually has a small real part. This real part can be used to evaluate the accuracy of $Z_g(\theta)$ obtained from HFSS simulations. The bigger the real part is, the

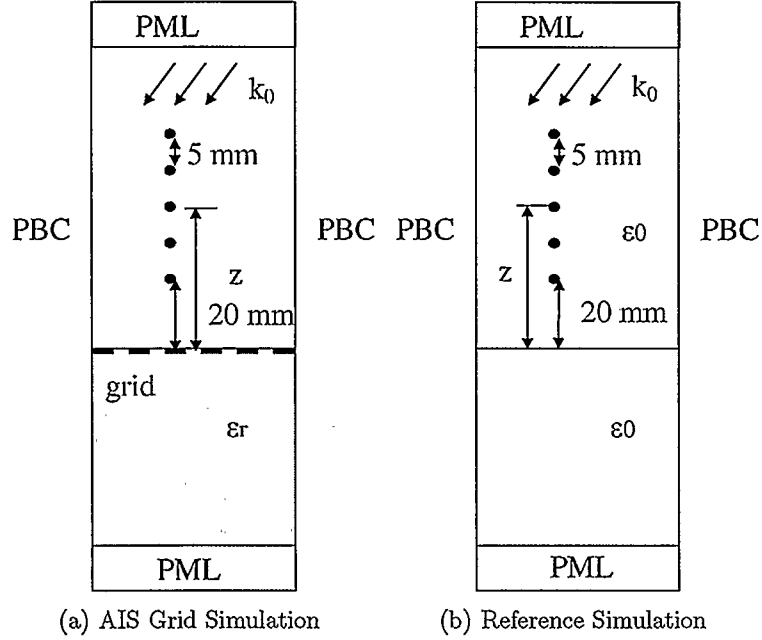


Figure 4.4: HFSS simulation setup for grid impedance calculation at oblique incidence.

less accurate $Z_g(\theta)$ is. In Figure 4.5, the real part of $Z_g^{TE}(\theta)$ and $Z_g^{TM}(\theta)$ obtained from HFSS simulations are shown for the patch AIS at 4 GHz. It is seen that, for the incident angle from 0° to 70° , the real part of $Z_g(\theta)$ is quite small. However, this real part becomes quite big when θ is 80° . This is due to the accuracy limitation of the HFSS simulator at high incident angles. Therefore, the HFSS $Z_g(\theta)$ results at 80° of incident angles are not considered in the following discussions.

It is quite clear that, from these comparison results, the constant grid impedance model provides reasonably accurate grid impedance values for both TE and TM incident waves in case of both AIS surfaces. For the patch AIS, the constant grid impedance model is more accurate for TM incident waves than for TE waves, while for the Jerusalem cross AIS, the constant grid impedance model is quite accurate for both TE and TM incident waves. Compared with the constant grid impedance model, the $\cos^2 \theta$ model does not model $Z_g(\theta)$ well over the full range of incidence angles when it differs from the constant grid impedance model (e.g. $Z_g^{TE}(\theta)$ for the patch AIS and $Z_g^{TM}(\theta)$ for the Jerusalem cross AIS). Therefore,

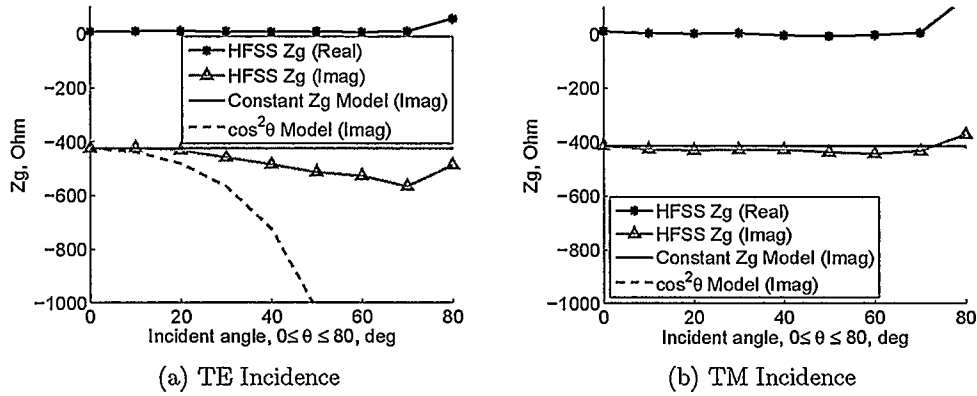


Figure 4.5: $Z_g(\theta)$ comparison of the constant grid impedance model, the $\cos^2 \theta$ model with HFSS simulation results as benchmark for the patch AIS at 4 GHz.

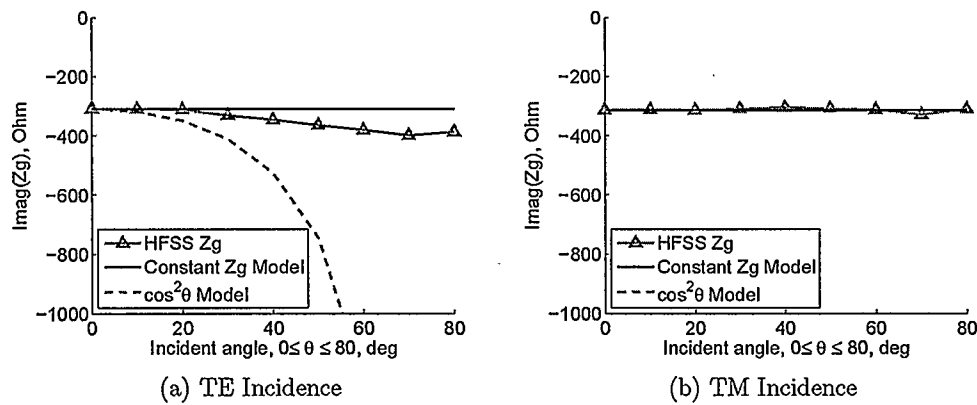


Figure 4.6: $Z_g(\theta)$ comparison of the constant grid impedance model, the $\cos^2 \theta$ model with HFSS simulation results as benchmark for the patch AIS at 5.5 GHz.

the constant grid impedance model, although simpler than the $\cos^2 \theta$ model, provides a more accurate estimation of the grid impedance.

4.1.2 Reflection Coefficient Test

As discussed before, the goal of using the constant grid impedance model is to achieve more efficient reflection coefficient calculation for the AIS. Therefore, it is important to verify the accuracy of $\Gamma(\theta)$ computed with this model. The grid impedance obtained in the previous section using the constant grid impedance model are used in Equation (4.1) to

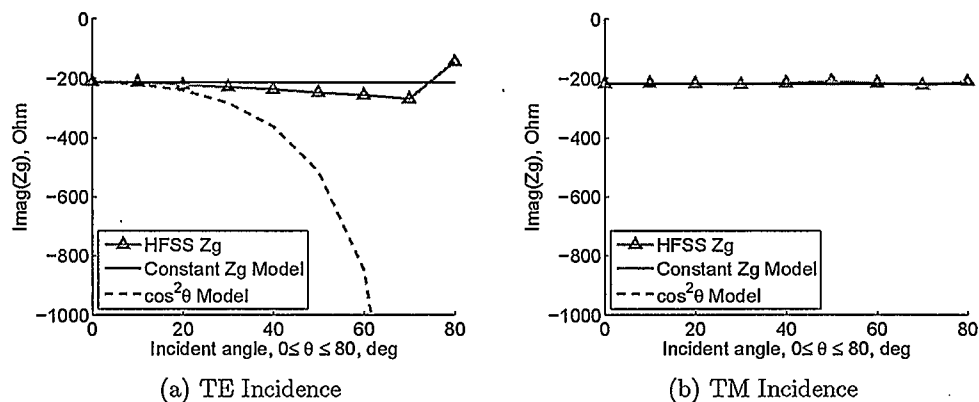


Figure 4.7: $Z_g(\theta)$ comparison of the constant grid impedance model, the $\cos^2 \theta$ model with HFSS simulation results as benchmark for the patch AIS at 7.7 GHz.

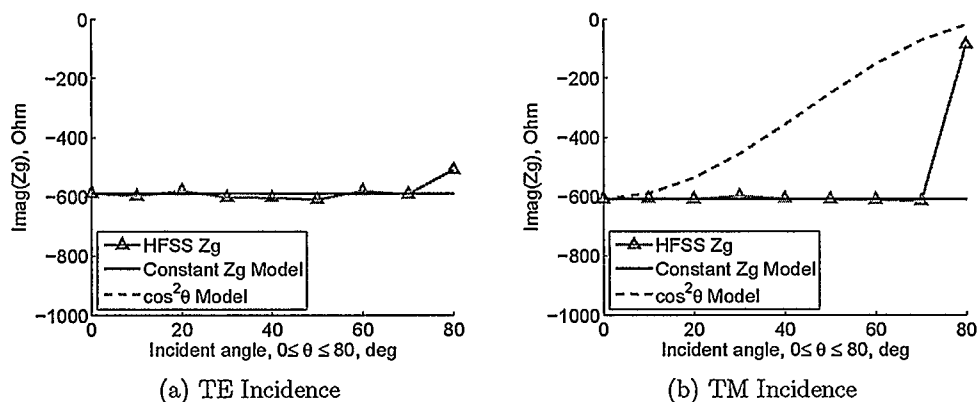


Figure 4.8: $Z_g(\theta)$ comparison of the constant grid impedance model, the $\cos^2 \theta$ model with HFSS simulation results as benchmark for the Jerusalem cross AIS at 4 GHz.

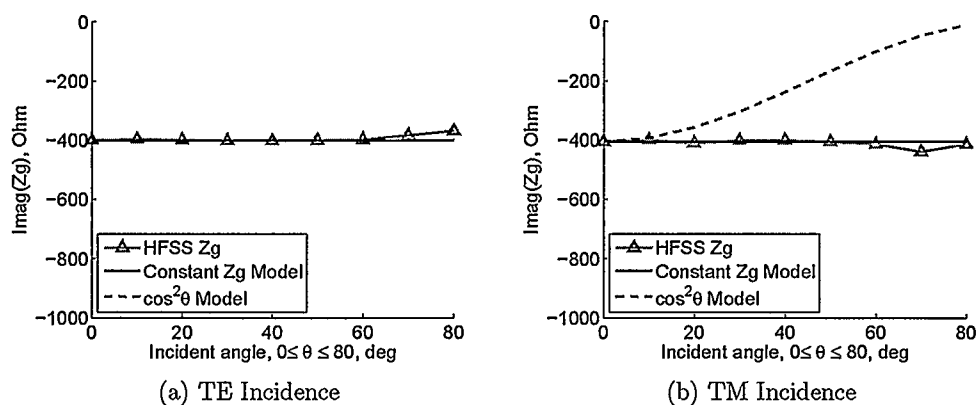


Figure 4.9: $Z_g(\theta)$ comparison of the constant grid impedance model, the $\cos^2 \theta$ model with HFSS simulation results as benchmark for the Jerusalem cross AIS at 5.5 GHz.

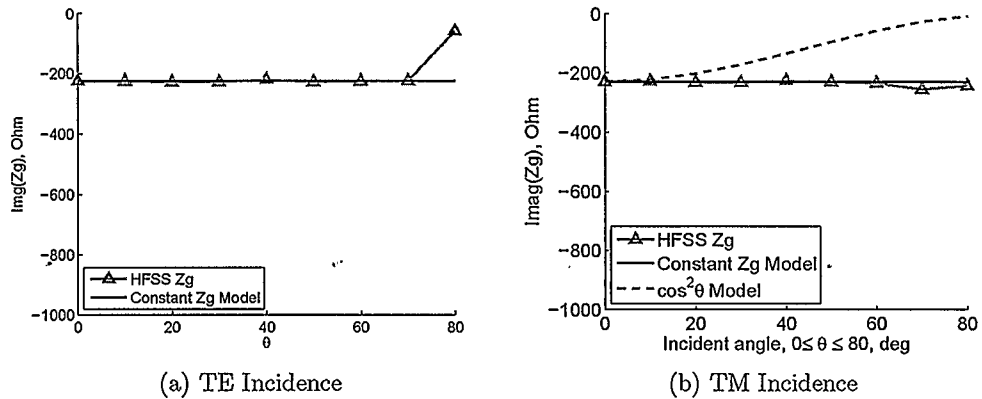


Figure 4.10: $Z_g(\theta)$ comparison of the constant grid impedance model, the $\cos^2\theta$ model with HFSS simulation results as benchmark for the Jerusalem cross AIS at 7.7 GHz.

obtain the reflection coefficients, $\Gamma(\theta)$, of the patch and Jerusalem cross AIS. The presence of the electric conductor at the bottom of each AIS ensures that the magnitude of $\Gamma(\theta)$ is always 1. Therefore, the phases of $\Gamma(\theta)$ values are compared with HFSS full-wave simulation results from Chapter 3. Figures 4.11 to 4.13 show the reflection phase comparison results of the patch AIS and Figures 4.14 to 4.16 show those of the Jerusalem cross AIS at 4 GHz, 5.5 GHz and 7.7 GHz.

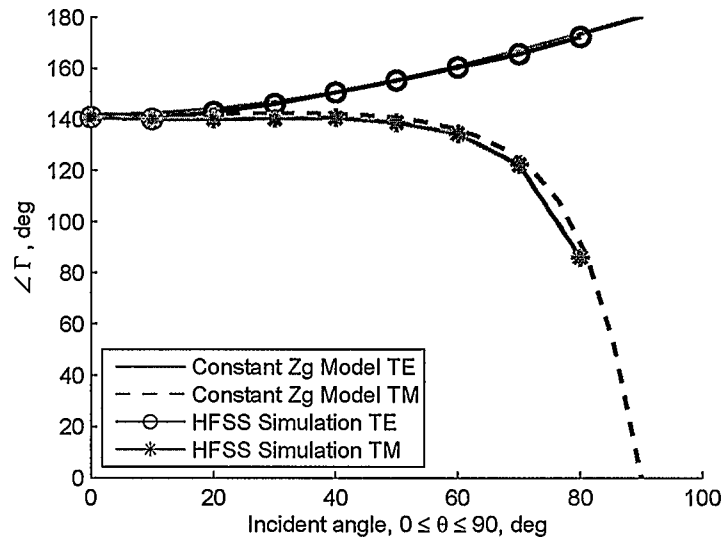


Figure 4.11: Comparison of reflection phase, $\angle\Gamma(\theta)$, calculated with the constant grid impedance model and simulated in HFSS for the patch AIS at 4 GHz.

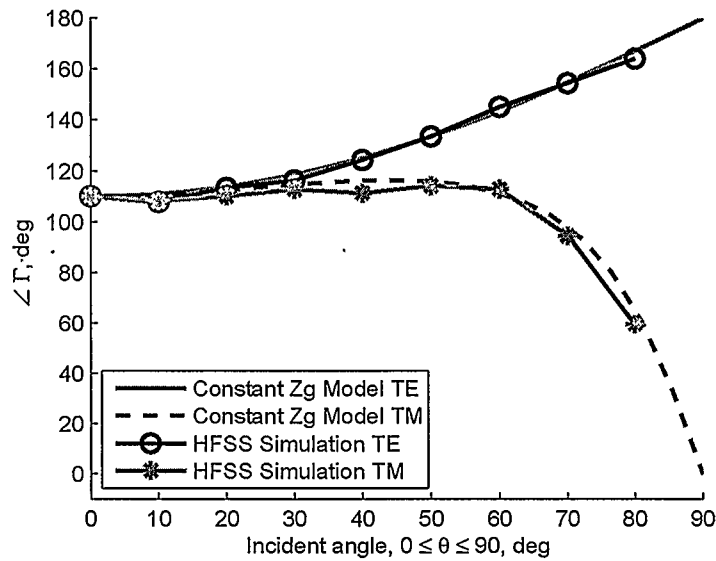


Figure 4.12: Comparison of reflection phase, $\angle\Gamma(\theta)$, calculated with the constant grid impedance model and simulated in HFSS for the patch AIS at 5.5 GHz.

For both the patch and Jerusalem cross AIS, the calculated reflection phase, $\angle\Gamma(\theta)$, match with the simulation results quite well at 4 GHz and 5.5 GHz. At 7.7 GHz, there is an error in the computed $\angle\Gamma^{TE}(\theta)$ of the patch AIS, while $\angle\Gamma^{TM}(\theta)$ matches well with the simulation (Figure 4.13). For the Jerusalem cross AIS, both the computed $\angle\Gamma^{TE}(\theta)$ and $\angle\Gamma^{TM}(\theta)$ match well with simulation results at 7.7 GHz (Figure 4.16).

4.1.3 Constant Grid Impedance Model Summary

In summary, the constant grid impedance model is simple but reasonably accurate for grid impedance and reflection coefficient computations of both the patch and Jerusalem cross AIS. As a grid impedance model, this model is simpler but more accurate than the $\cos^2\theta$ model proposed in [26]. An error, however, is found in the computed reflection coefficient $\Gamma^{TE}(\theta)$ of the patch AIS at the resonant frequency of the AIS.

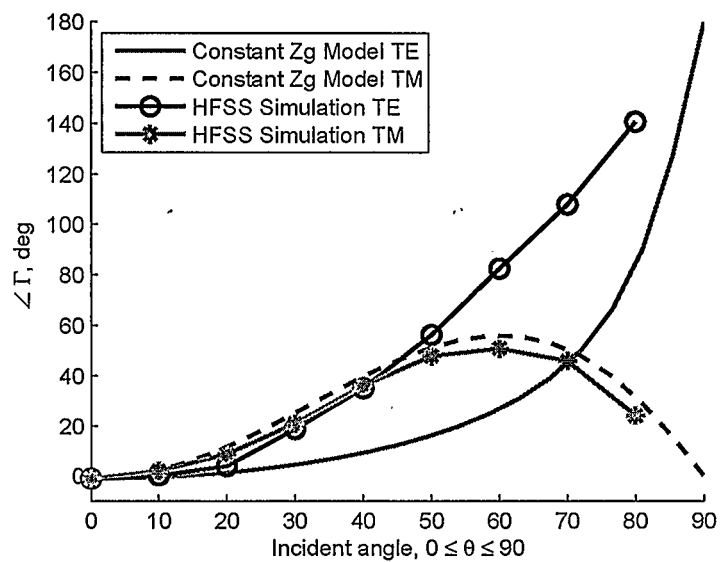


Figure 4.13: Comparison of reflection phase, $\angle \Gamma(\theta)$, calculated with the constant grid impedance model and simulated in HFSS for the patch AIS at 7.7 GHz.

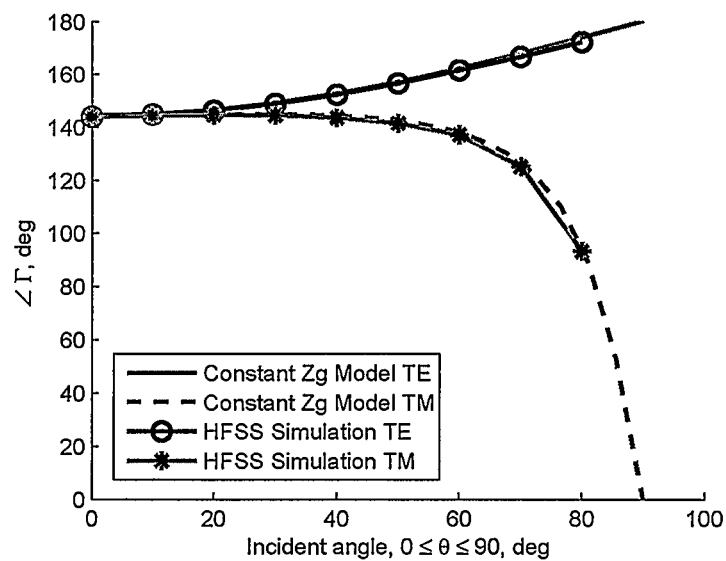


Figure 4.14: Comparison of reflection phase, $\angle \Gamma(\theta)$, calculated with the constant grid impedance model and simulated in HFSS for the Jerusalem cross AIS at 4 GHz.

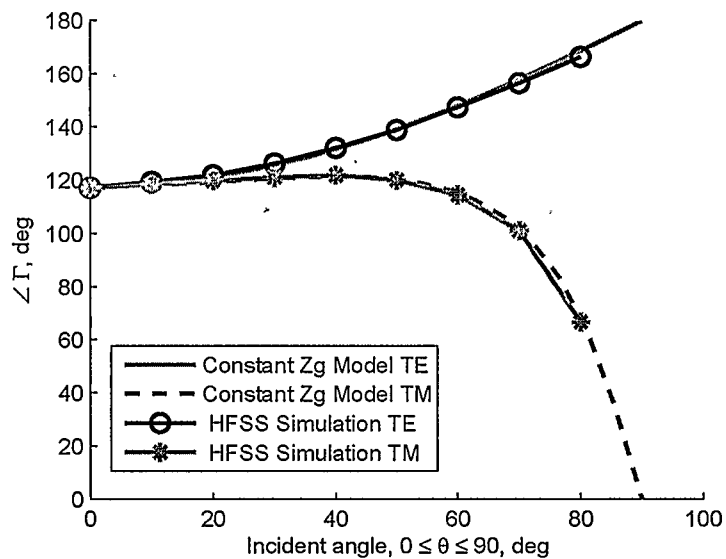


Figure 4.15: Comparison of reflection phase, $\angle \Gamma(\theta)$, calculated with the constant grid impedance model and simulated in HFSS for the Jerusalem cross AIS at 5.5 GHz.

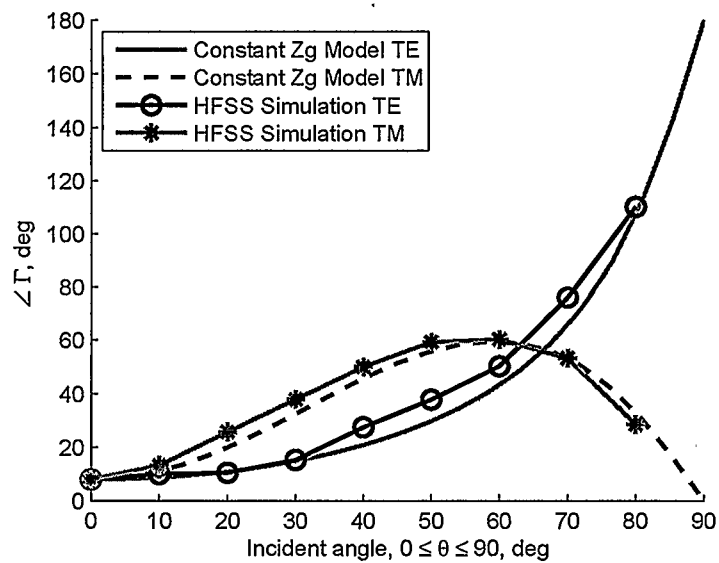


Figure 4.16: Comparison of reflection phase, $\angle \Gamma(\theta)$, calculated with the constant grid impedance model and simulated in HFSS for the Jerusalem cross AIS at 7.7 GHz.

4.2 Reflection Phase Error Analysis

As discussed in the previous section, there is some error in the calculated $\angle\Gamma^{TE}(\theta)$ for the patch AIS at 7.7 GHz, the AIS resonant frequency (see Figure 4.13). The possible sources of this error are the constant grid impedance model and the AIS parallel circuit model. In this section, the accuracy in both models are analyzed in detail.

4.2.1 Error Analysis for the Constant Grid Impedance Model

To help analyze the error in the constant grid impedance model, we define,

$$Z_g^{Error}(\theta) = \left| \frac{Z_g^{HFSS}(\theta) - Z_g^{Constant}(\theta)}{Z_g^{HFSS}(\theta)} \right|, \quad (4.14)$$

where $Z_g^{HFSS}(\theta)$ is the grid impedance obtained from the HFSS simulation shown in Figure 4.4, and $Z_g^{Constant}(\theta)$ is the grid impedance obtained with the constant grid impedance model. Since $Z_g^{Constant}(\theta) = Z_g^{HFSS}(0)$, Equation (4.14) can also be written as,

$$Z_g^{Error}(\theta) = \left| \frac{Z_g^{HFSS}(\theta) - Z_g^{HFSS}(0)}{Z_g^{HFSS}(\theta)} \right|. \quad (4.15)$$

Tables 4.1 and 4.2 show the maximum Z_g^{Error} over the incident angle, (from 0° to 70°), at 4 GHz, 5.5 GHz, and 7.7 GHz for the patch and Jerusalem cross AIS, respectively.

For the patch AIS, it is first noted that, at 7.7 GHz, the maximum Z_g^{Error} in the constant grid impedance model is much larger for TE incident waves (or TE mode) than for TM waves (or TM mode). This explains why the error in the computed $\Gamma^{TE}(\theta)$ is larger than in $\Gamma^{TM}(\theta)$ at this frequency (see Figure 4.13). Then, it is also noted that the maximum Z_g^{Error} for TE incident waves decreases as the frequency increases. This means that the error in the constant grid impedance model is the smallest at 7.7 GHz. However, as observed in Figures 4.11 to 4.13, the error in the computed $\Gamma^{TE}(\theta)$ is the largest at 7.7 GHz. Since the constant grid impedance model is the most accurate at 7.7 GHz, errors in the constant grid impedance model can not explain the error in calculated $\Gamma^{TE}(\theta)$ at 7.7 GHz. Therefore,

Table 4.1: Maximum Z_g^{Error} over Incident Angles for the Patch AIS

Maximum Z_g^{Error}	4GHz	5.5GHz	7.7GHz
TM mode	6.39%	4.62%	2.4%
TE mode	24.94%	22.62%	21%

Table 4.2: Maximum Z_g^{Error} over Incident Angles for the Jerusalem Cross AIS

Maximum Z_g^{Error}	4GHz	5.5GHz	7.7GHz
TM mode	1.67%	7.83%	10.05%
TE mode	3.32%	4.22%	1.92%

it is suspected that, to achieve accurate $\Gamma^{TE}(\theta)$, the circuit model requires a extremely accurate grid impedance model at 7.7 GHz, the resonant frequency of the patch AIS. This phenomenon is referred to as the circuit model sensitivity in this thesis, and is analyzed in section 4.2.2.

For the Jerusalem cross AIS, the maximum Z_g^{Error} is in general much smaller than that of the patch AIS. This indicates that the constant grid impedance model, as a grid impedance model, is a better approximation for the Jerusalem cross AIS. At 5.5 GHz and 7.7 GHz, the maximum Z_g^{Error} of the Jerusalem cross AIS for the TM incident wave is 7.83% and 10.05%, larger than that of the patch AIS (4.62% and 2.4%). However, the computed $\Gamma^{TM}(\theta)$ for the Jerusalem cross AIS at 5.5 GHz and 7.7 GHz match as well with simulation results (Figures 4.15 and 4.16) as for the patch AIS (Figures 4.12 and 4.13). This suggests that the grid impedance error may be less of a concern at the AIS resonant frequency for the TM incidence.

4.2.2 Circuit Model Sensitivity Analysis

To evaluate the circuit model sensitivity, a constant grid impedance, $Z_g(\theta) = Z_g(0)$ for all θ , is used in Equation (4.1), with $Z_{in}(\theta)$ still defined as in Equation (4.3). A constant error in $Z_g(\theta)$ is introduced and the resulting error in the phase of reflection coefficients, $\angle\Gamma$, is observed. The error in $Z_g(\theta)$ is defined as $\Delta Z_g(\theta) = p\%Z_g(0)$ and the error in $\angle\Gamma$, $\angle\Gamma$ Error (θ), is calculated from,

$$\angle\Gamma Error(\theta) = \angle\Gamma^{Error}(\theta) - \angle\Gamma(\theta), \quad (4.16)$$

where $\angle\Gamma^{Error}(\theta)$ and $\angle\Gamma(\theta)$ are the reflection phase with and without the grid impedance error, respectively. We use $Z_g(0) = Z_g^{HFSS, Patch}(0)$ and $p\% = 30\%$ for this analysis. Thus, the resulting $\angle\Gamma$ Error (θ) as a function of frequency are shown in Figures 4.17 to 4.19 for the incident angle of 0° , 40° , and 70° respectively.

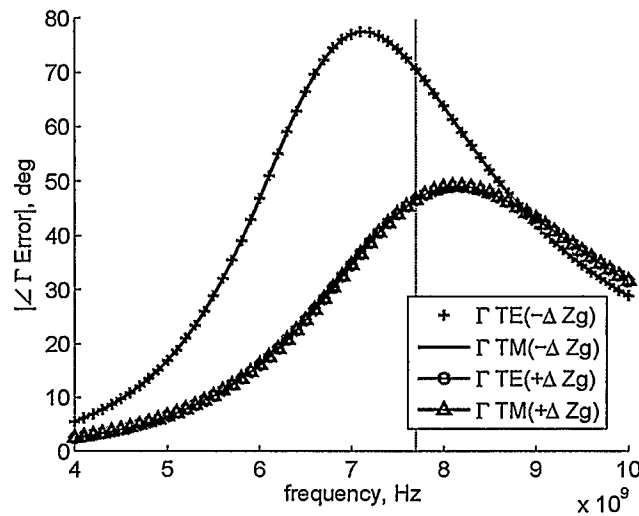


Figure 4.17: Reflection phase error caused by grid impedance error for the patch AIS with incident angle $\theta = 0^\circ$ and grid impedance error $\Delta Z_g(\theta) = 30\%Z_g^{HFSS, Patch}(0)$.

At normal incidence, the TE and TM incident waves are essentially the same, so the absolute $\angle\Gamma$ Error of the TE and TM modes are also the same for this case. Observing Figure 4.17, it is noted, firstly, the reflection phase error, $\angle\Gamma$ Error, are less affected by a

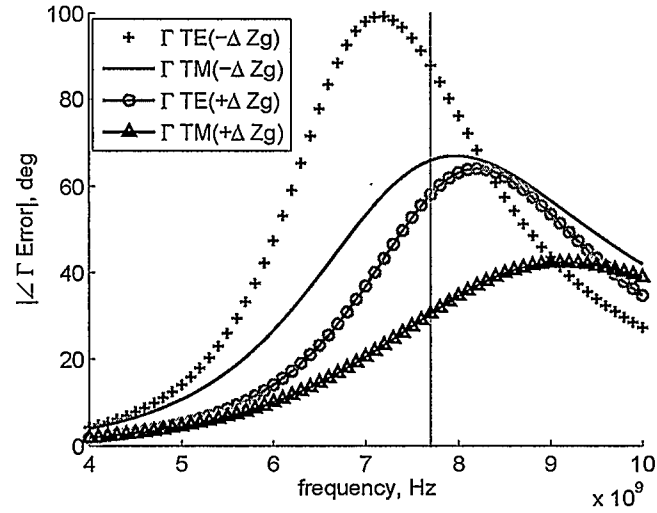


Figure 4.18: Reflection phase error caused by grid impedance error for the patch AIS with incident angle $\theta = 40^\circ$ and grid impedance error $\Delta Z_g(\theta) = 30\%Z_g^{HFSS, Patch}(0)$.

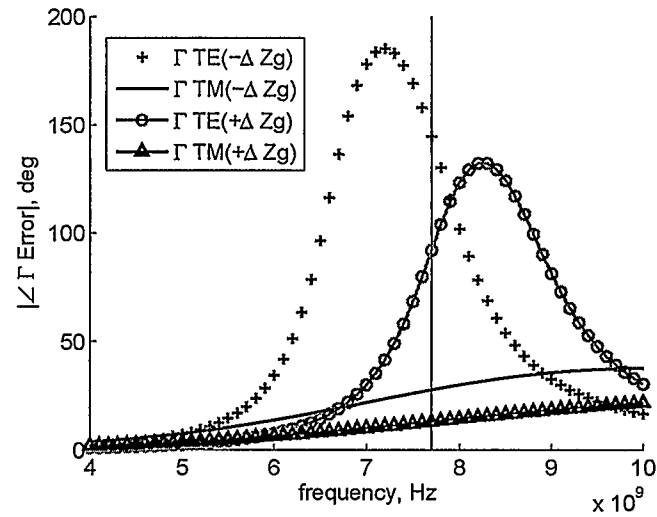


Figure 4.19: Reflection phase error caused by grid impedance error for the patch AIS with incident angle $\theta = 70^\circ$ and grid impedance error $\Delta Z_g(\theta) = 30\%Z_g^{HFSS, Patch}(0)$.

relatively big grid impedance error at frequencies much below 7.7 GHz. For example, at 4 GHz, the reflection phase error caused by $\pm 30\%$ of grid impedance error is only about 2.5° and 5.5° . At 5 GHz, $\angle \Gamma$ Error is still less than 10° and 20° , respectively. Secondly, when we approach the resonant frequency, 7.7 GHz, the reflection phase error increase significantly and the maximum $\angle \Gamma$ Error is found near 7.7 GHz. For example, at 7 GHz, the $\angle \Gamma$ Error, caused by -30% grid impedance error, becomes as large as 75° . When we move above the resonant frequency, the reflection phase error caused by the grid impedance error becomes small again. Thirdly, below 7.7 GHz, the reflection phase error caused by the $+\Delta Z_g$ is in general smaller than that caused by $-\Delta Z_g$.

When $\theta = 40^\circ$ (Figure 4.18), similar phenomena are still observed. At frequencies much below the resonant frequency, say 4 GHz, 5 GHz and 6 GHz, the reflection phase error caused by the grid impedance error becomes even smaller. When approaching 7.7 GHz, the reflection phase error for TE incident waves still increases significantly and a maximum $\angle \Gamma$ Error can be found near 7.7 GHz. For TM incident waves, the maximum $\angle \Gamma$ Error shifts to a higher frequency, so the error in the phase of the reflection coefficient at 7.7 GHz is smaller than at normal incidence. As before, the error caused by $+\Delta Z_g$ is still smaller than that caused by $-\Delta Z_g$ below the resonant frequency.

At 70° of incident angle, (see Figure 4.19), the reflection phase error at frequencies below the resonant frequency, 7.7 GHz, becomes even smaller. Approaching 7.7 GHz, the reflection phase error for TE incident waves still increase dramatically and the maximum $\angle \Gamma$ Error can still found around 7.7 GHz. For TM incident waves, the reflection phase error caused by $\pm \Delta Z_g$ becomes quite small between 4 GHz and 10 GHz and no peaks are found in this range. The same as before, the error caused by $+\Delta Z_g$ is still smaller than that caused by $-\Delta Z_g$ below the resonant frequency.

The above observations explain why the error in the computed $\Gamma^{TE}(\theta)$ of the patch AIS is the largest at 7.7 GHz even though the error in the constant grid impedance model is the

smallest. The maximum Z_g^{Error} shown in Table 4.1 are usually located at higher incident angles. At high incident angles, the grid impedance errors have very little effect on the accuracy of the reflection phase computation for frequencies below the resonant frequency. As a result, although the constant grid impedance model has an error of 24.94% and 22.62% at 4 GHz and 5.5 GHz, the computed $\Gamma^{TE}(\theta)$ are still quite accurate. However, at 7.7 GHz, the reflection phase computation is quite sensitive to the grid impedance error. Therefore, a large error is resulted in $\Gamma^{TE}(\theta)$ at this frequency due to the 21% error in the constant grid impedance model.

By observing Figures 4.17 to 4.19, some general rules for grid impedance models can be found in order to achieve accurate reflection coefficients computation for AIS structures using the circuit model. Here, we assume that the grid impedance model is accurate at normal incidence and errors tend to happen at high incident angles. The frequency range of interest is at and below the AIS resonant frequency. For TE incident waves, the grid impedance model only needs to be extremely accurate at and close to the AIS resonant frequency. For frequencies below the resonance, grid impedance errors are more tolerable. For TM incident waves, the accuracy requirement for the grid impedance model at the resonant frequency is not as high as TE incident waves. In another word, errors in the grid impedance model for the TM incidence are more tolerable at and below the AIS resonant frequency. For both TE and TM incidence, $-\Delta Z_g$ error, meaning the grid impedance model predicts a smaller $Z_g(\theta)$ than the accurate $Z_g(\theta)$, is more harmful than $+\Delta Z_g$, meaning the modeled grid impedance is larger than the accurate $Z_g(\theta)$, at and below the resonant frequency.

4.2.3 Reflection Phase Error Analysis Summary

In summary, it was shown that the error in the calculated $\Gamma^{TE}(\theta)$ of the patch AIS at 7.7 GHz, using the constant grid impedance model, is caused by the circuit model sensitivity. This phenomenon requires the grid impedance model to be extremely accurate

near the AIS resonant frequency for accurate $\Gamma^{TE}(\theta)$ computation. Also, by studying the circuit model sensitivity phenomenon, a general outline for a grid impedance model to achieve accurate $\Gamma(\theta)$ computation is given.

4.3 Circuit Model Analysis

In the previous section, the error in the computed $\Gamma^{TE}(\theta)$ of the patch AIS at 7.7 GHz was analyzed numerically. It was shown that this error is caused by the circuit model sensitivity at the resonant frequency of the patch AIS. Due to the circuit model sensitivity, the reflection phase error, caused by the grid impedance error, increases significantly near the AIS resonant frequency for TE incident waves, shown in Figures 4.17 to 4.19. Observing these figures, however, it is noted that the maximum $\angle\Gamma$ Error is not located exactly at the AIS resonant frequency, 7.7 GHz. Instead, it is slightly below or above the AIS resonance, depending on the sign of the grid impedance error, $\Delta Z_g(\theta) = p\%Z_g(0)$. Also, it was observed that, the maximum $\angle\Gamma$ Error behaves differently for TE and TM incident waves as the incident angle increases. However, the reason was not clear. In order to understand these phenomena better, the circuit model is analyzed analytically in sections 4.3.1 and 4.3.2. In section 4.3.3, after simplifying the $\angle\Gamma$ Error equation at the AIS resonant frequency, it was found that the error in $\Gamma^{TE}(\theta)$ at the AIS resonance can be reduced for AIS with larger dielectric thickness.

4.3.1 Frequency Location of the Maximum $\angle\Gamma$ Error

To find the frequency location of the maximum $\angle\Gamma$ Error, caused by the grid impedance error, the reflection phase error, $\angle\Gamma$ Error (θ), is expressed as

$$\angle\Gamma Error(\theta) = \angle\Gamma^{Error}(\theta) - \angle\Gamma(\theta), \quad (4.17)$$

where,

$$\angle\Gamma^{Error}(\theta) = -\pi - 2 \tan^{-1} \left[\frac{\text{Imag}(Z_s^{Error}(\theta))}{Z_0(\theta)} \right], \quad (4.18)$$

$$\angle\Gamma(\theta) = -\pi - 2 \tan^{-1} \left[\frac{\text{Imag}(Z_s(\theta))}{Z_0(\theta)} \right]. \quad (4.19)$$

The function $\text{Imag}(x)$ takes the imaginary part of the complex variable x . The surface impedances, $Z_s^{\text{Error}}(\theta)$ and $Z_s(\theta)$, are computed by,

$$Z_s^{\text{Error}}(\theta) = \frac{Z_{in}(\theta)Z_g^{\text{HFSS,Error}}(0)}{Z_{in}(\theta) + Z_g^{\text{HFSS,Error}}(0)}, \quad (4.20)$$

and,

$$Z_s(\theta) = \frac{Z_{in}(\theta)Z_g^{\text{HFSS}}(0)}{Z_{in}(\theta) + Z_g^{\text{HFSS}}(0)}, \quad (4.21)$$

respectively. As before, $Z_{in}(\theta)$ and $Z_0(\theta)$ are given by Equations (4.3) and (4.2); $Z_g^{\text{HFSS}}(0)$ is the grid impedance obtained from HFSS at normal incidence, and $Z_g^{\text{HFSS,Error}}(0)$ is the grid impedance with the constant grid impedance error $\Delta Z_g(\theta) = p\%Z_g^{\text{HFSS}}(0)$.

To find the maximum $\angle\Gamma$ Error, the derivative of Equation (4.17) is taken [44] over Z_{in} ,

$$\frac{d(\angle\Gamma^{\text{Error}})}{dZ_{in}} = \frac{d(\angle\Gamma^{\text{Error}})}{dZ_{in}} - \frac{d(\angle\Gamma)}{dZ_{in}}. \quad (4.22)$$

With the help of Matlab, we obtain,

$$\frac{d(\angle\Gamma^{\text{Error}})}{dZ_{in}} = \frac{2Z_g^2(1+p\%)^2Z_0}{Z_{in}(Z_g^2(1+p\%)^2 + Z_0^2) + Z_{in}(2Z_0^2Z_g(1+p\%)) + Z_0^2Z_g^2(1+p\%)^2}, \quad (4.23)$$

and,

$$\frac{d(\angle\Gamma)}{dZ_{in}} = \frac{2Z_g^2Z_0}{Z_{in}(Z_g^2 + Z_0^2) + Z_{in}(2Z_0^2Z_g) + Z_0^2Z_g^2}. \quad (4.24)$$

For $\angle\Gamma$ Error to reach its maximum value, Equation (4.22) = 0. Hence,

$$Z_{in} = -\frac{2(1+p\%)}{(2+p\%)}Z_g, \quad (4.25)$$

is obtained after simplification. Note that, for $p > 0$,

$$1 < \frac{2(1+p\%)}{(2+p\%)} < (1+p\%), \quad (4.26)$$

and for $p < 0$,

$$(1+p\%) < \frac{2(1+p\%)}{(2+p\%)} < 1. \quad (4.27)$$

Equations (4.26) and (4.27) indicate that the maximum $\angle\Gamma$ Error caused by the constant grid impedance model is always located between the frequencies where the resonance condition $Z_{in}(\theta) = -Z_g^{HFSS}(0)$ or $Z_{in}(\theta) = -Z_g^{HFSS,Error}(0) = -(1 + p\%)Z_g$ is satisfied. These two resonance conditions are close to each other in frequency. The smaller the grid impedance error ($p\%$) is, the closer in frequency these two resonance conditions are.

4.3.2 $\angle\Gamma$ Error Characteristic for TE and TM Incidence

It has been shown the maximum $\angle\Gamma$ Error is located between frequencies where the resonance conditions, $Z_{in}(\theta) = -Z_g^{HFSS}(0)$ and $Z_{in}(\theta) = -Z_g^{HFSS,Error}(0)$, are satisfied. In our analysis, $Z_g^{HFSS}(0)$ and $Z_g^{HFSS,Error}(0)$ are set for a chosen grid impedance error, so the frequency location of the maximum $\angle\Gamma$ Error completely depends on the values of $Z_{in}(\theta)$. When $Z_{in}(\theta)$ increases with the increase of θ , these resonance conditions are satisfied at lower frequencies; when $Z_{in}(\theta)$ decreases, they are satisfied at higher frequencies. The difference between $Z_{in}^{TE}(\theta)$ and $Z_{in}^{TM}(\theta)$ with the increase of θ results in the different frequency locations of the maximum $\angle\Gamma$ Error for TE and TM incident waves.

For TE incident waves, $Z_{in}(\theta)$ is expressed as,

$$Z_{in}^{TE}(\theta) = j \frac{Z_d}{\cos \alpha} \tan(k_d d \cos \alpha), \quad (4.28)$$

or,

$$Z_{in}^{TE}(\theta) = j \frac{Z_0}{\sqrt{\epsilon_r} \cos \alpha} \tan(\sqrt{\epsilon_r} \frac{2\pi}{\lambda_0} d \cos \alpha), \quad (4.29)$$

since $Z_d = Z_0/\sqrt{\epsilon_r}$ and $k_d = k_0\sqrt{\epsilon_r}$. Here, Z_0 and λ_0 are the free space impedance and wavelength; ϵ_r is the relative permittivity of the dielectric slab of the AIS; and α is the transmitted angle in the dielectric slab which is related to the incident angle θ by Snell's Law [43]. Since the dielectric thickness of the AIS considered in this thesis is relatively small compared to the free space wavelength (for example, $d/\lambda = 0.0769$ at 7.7 GHz), $\sqrt{\epsilon_r} \frac{2\pi}{\lambda} d \cos \alpha \ll 1$. Thus, Equation (4.29) can be approximated as,

$$Z_{in}^{TE}(\theta) \approx j Z_0 \frac{2\pi}{\lambda} d. \quad (4.30)$$

This is a constant over the incident angle. Because of this, the maximum $\angle\Gamma$ Error of the TE incident waves are locate at almost the same frequency for all incident angles.

For TM incident waves,

$$Z_{in}^{TM}(\theta) = jZ_d \cos \alpha \tan(k_d d \cos \alpha). \quad (4.31)$$

Following the same procedure, Equation (4.31) can be approximated as,

$$Z_{in}^{TM}(\theta) \approx jZ_0 \frac{2\pi}{\lambda} d \left(1 - \frac{\sin^2 \theta}{\epsilon_r}\right). \quad (4.32)$$

Unlike $Z_{in}^{TE}(\theta)$, $Z_{in}^{TM}(\theta)$ is not independent of frequency. It decreases with the increase of θ . Thus, the maximum $\angle\Gamma$ Error shifts to higher frequencies as θ increases. Therefore, the $\angle\Gamma$ Error of the TM incidence at 7.7 GHz decreases with the increase of θ . As a result, at the AIS resonant frequency, the reflection coefficients $\Gamma^{TM}(\theta)$ are less affected by the grid impedance errors.

4.3.3 Decreasing $\Gamma^{TE}(\theta)$ Error at AIS Resonance

As already discussed, a large error in $\angle\Gamma^{TE}(\theta)$ can be caused by a small grid impedance error near the AIS resonant frequency for all incident angles. In order to decrease $\angle\Gamma^{TE}(\theta)$ Error at the AIS resonant frequency, Equation (4.17) is studied. Note that, when $Z_{in}(\theta) + Z_g^{HFSS}(0) = 0$, Equation (4.17) can be simplified as,

$$\angle\Gamma Error(\theta) = \pi - 2 \tan^{-1} \left[\frac{1 \pm p\% \text{Imag}(Z_{in}(\theta))}{\pm p\% \frac{Z_0(\theta)}{Z_0(\theta)}} \right]. \quad (4.33)$$

As discussed in section 4.3.2, the condition $Z_{in}(\theta) + Z_g^{HFSS}(0) = 0$ is approximately satisfied at the AIS resonant frequency at all incident angles for TE incident waves. Therefore, by using Equation (4.28), Equation (4.33) can be written as,

$$\angle\Gamma Error(\theta) = \pi - 2 \tan^{-1} \left[\frac{1 \pm p\% \cos \theta}{\pm p\% \frac{\cos \theta}{\sqrt{\epsilon_r} \cos \alpha}} \tan(k_d d \cos \alpha) \right], \quad (4.34)$$

for TE incident waves. Observing Equation (4.34), it is noted that $\angle\Gamma$ Error is a function of the dielectric thickness, d . When d is increased, $\angle\Gamma$ Error decreases ($\rightarrow 0$); when d is

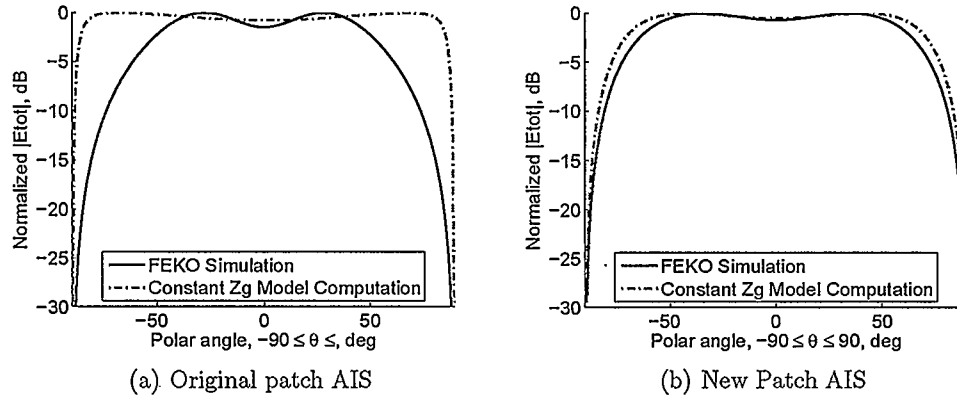


Figure 4.20: H-plane far-field Pattern comparisons for a Hertzian dipole over two Patch AIS at 7.7GHz. (a) Original patch AIS: dielectric thickness, 3 mm; patch size, 6 mm. (b) New patch AIS: dielectric thickness, 6 mm; patch size, 3 mm. Both AIS resonate at 7.7GHz.

decreased, $\angle \Gamma$ Error increases ($\rightarrow \pi$). Therefore, by increasing the dielectric thickness, the errors in computed $\Gamma^{TE}(\theta)$ using the constant grid impedance model at the AIS resonance can be decreased.

Since the accuracy of $\Gamma^{TE}(\theta)$ determines the accuracy of the H-plane far-field pattern computed from the far-field model, the calculated far-field patterns of the patch AIS with thicker dielectric are expected to match better with simulation results. Figures 4.20 compare the calculated H-plane pattern of the original patch AIS and a new patch AIS with simulation at 7.7 GHz. The dielectric thickness of the new AIS is 6 mm while that of the original patch AIS is 3 mm. For comparison, we need to design the new AIS such that it resonates at the same frequency as the old AIS, e.g. 7.7 GHz. With the increased dielectric thickness, the new AIS has a larger Z_{in} (inductance). Thus, for the new AIS to resonate at 7.7 GHz, the gaps between patches of the AIS need to be increased, which is equivalent to a smaller capacitance between the patches (Z_g). It is found that when the single patch size is reduced to 3 mm while the gap between patches is increased to 4 mm, the new patch AIS resonant at 7.7 GHz. Observing Figure 4.20, it is clearly seen that the calculated far-field pattern of the thicker patch AIS is much more accurate.

4.3.4 Circuit Model Analysis Summary

The behavior of the circuit model is summarized here for the AIS with small dielectric thickness relative to free space wavelength. For TE incident waves, the circuit model requires an accurate grid impedance model near the AIS resonant frequency for all incident angles. However, it is found that the errors in $\Gamma^{TE}(\theta)$, caused by the grid impedance error, at the AIS resonant frequency can be reduced by increasing dielectric thickness, d . For TM incident waves, the requirement for accurate grid impedance models at the AIS resonant frequency is not as high as the TE incidence. Below the AIS resonant frequency, the circuit model is quite insensitive to grid impedance errors.

4.4 Modified Constant Z_g Model for Patch AIS

As shown in the previous sections, the constant grid impedance model, as a simple first-order approximation, can be used to calculate the reflection coefficients of the patch and Jerusalem cross AIS. For the Jerusalem cross AIS, this model approximates the AIS grid impedance quite well at all test frequencies. Thus, reflection coefficients obtained using this model are quite accurate. For the patch AIS, the constant grid impedance model can be used for accurate reflection coefficients computation at all test frequencies except the $\Gamma^{TE}(\theta)$ computation at the AIS resonant frequency. In this section, the constant grid impedance model is modified for the patch AIS so that both $\Gamma^{TE}(\theta)$ and $\Gamma^{TM}(\theta)$ can be computed accurately at and below the AIS resonant frequency for both TE and TM incidence.

4.4.1 Model Description

The constant grid impedance model is accurate except at the AIS resonant frequency for TE incident waves, so it needs to be modified at 7.7 GHz (the patch AIS resonant frequency) for TE incident waves. Therefore, a curve fitting technique is used at this frequency to obtain the modified grid impedance function. For this, we first note that $Z_g^{TE}(\theta)$ is a function

of the grid impedance at normal incidence $Z_g(0)$. This is evident from the HFSS results in Figure 4.5 to 4.7. Also, we assume that $Z_g^{TE}(\theta)$ is related to a trigonometric function, since the electric and magnetic fields are related to the incident angle with such a function. At last, we expect $Z_g^{TE}(\theta)$ can be expanded into a series of trigonometric functions to the power of n . Based on these ideas, a model for the patch AIS can be expressed as

$$Z_g^{TE}(\theta) = Z_g(0)(1 + K_1 \sin \theta + K_2 \sin^2 \theta + K_3 \sin^3 \theta + \dots + K_n \sin^n \theta), \quad (4.35)$$

where, $K_n (n = 1, 2, 3, \dots)$ are the empirical fitting parameters. At 7.7 GHz, it is found that, when $K_3 = 0.3$, all other K_n can be reduced to 0. Therefore, Equation (4.35) is simplified to,

$$Z_g^{TE}(\theta) = Z_g(0)(1 + 0.3 \sin^2 \theta). \quad (4.36)$$

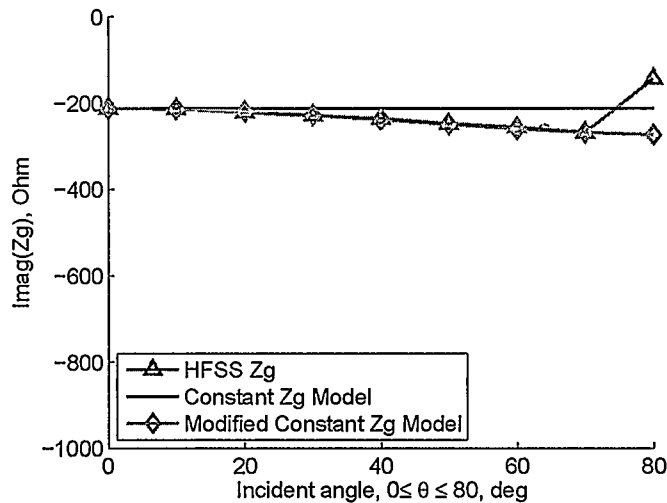


Figure 4.21: Patch AIS grid Impedance comparison between the HFSS simulation, the constant grid impedance model, and the modified grid impedance model at 7.7 GHz for the TE incidence.

Figure 4.21 compares the grid impedance calculated using Equation (4.35), using the constant grid impedance model and HFSS simulation. As before, the grid impedance results obtained from HFSS simulations at 80° should be ignored. Clearly, the calculated $Z_g^{TE}(\theta)$ is quite accurate with the empirical formula. As for the $\Gamma^{TE}(\theta)$ results, the calculated

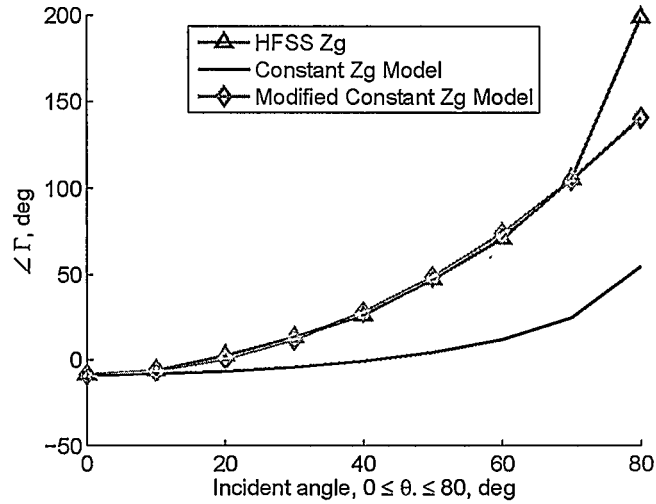


Figure 4.22: Patch AIS reflection phase comparison between the HFSS simulation, the constant grid impedance model, and the modified grid impedance model at 7.7 GHz for the TE incidence.

$Z_g^{TE}(\theta)$ is used in the circuit model to obtain the results shown in Figure 4.22. Also shown here are the results from the HFSS simulation, the constant grid impedance model. It is obvious that the modified empirical formula provides results that are in close agreement with the simulation. In the next section (section 4.4.2), Equation (4.36) is tested at 4 GHz and 5.5 GHz.

4.4.2 Model Verification

To test the accuracy of the modified constant grid impedance model, $Z_g^{TE}(\theta)$ and $\Gamma^{TE}(\theta)$ are calculated for the patch AIS at 4 GHz and 5.5 GHz. Results are shown in Figures 4.23 to 4.26. Clearly, the modified constant grid impedance model approximates both the grid impedance, $Z_g^{TE}(\theta)$, and reflection coefficients, $\Gamma^{TE}(\theta)$, quite well at 4GHz and 5.5GHz.

To better illustrate the performance of this modified grid impedance model, the maximum Z_g^{Error} over θ of the modified model are compared with that of the constant Z_g model for the patch AIS in Table 4.3. Only results for TE incident waves are shown. Results

Table 4.3: Comparing the Constant Z_g Model and the modified Z_g Model (Maximum Z_g^{Error} over incident angles for the Patch AIS)

Maximum Z_g^{Error}	4GHz	5.5GHz	7.7GHz
Modified Z_g Model	5.07%	2.13%	1.42%
Constant Z_g Model	24.94%	22.62%	21%

indicate that Equation (4.36) is accurate not just at 7.7 GHz, but at other frequencies below that as well.

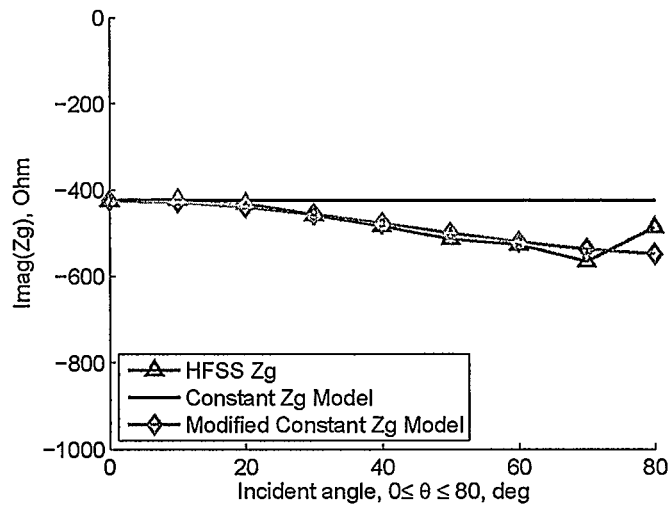


Figure 4.23: Patch AIS grid impedance comparison between the HFSS simulation, the constant grid impedance model, and the modified grid impedance model at 4 GHz for the TE incidence.

4.4.3 Model Application

Based on the above discussion, the modified constant grid impedance model for the patch AIS can expressed as

$$Z_g^{TE}(\theta) = Z_g(0)(1 + 0.3 \sin^2 \theta), \quad (4.37)$$

$$Z_g^{TM}(\theta) = Z_g(0), \quad (4.38)$$

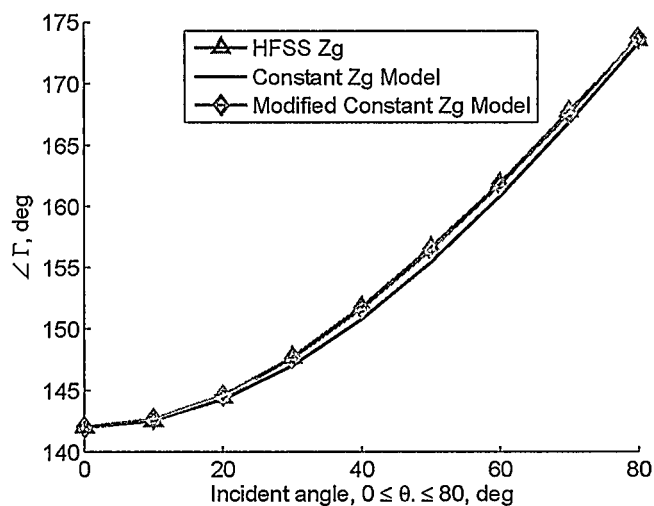


Figure 4.24: Patch AIS reflection phase comparison between the HFSS simulation, the constant grid impedance model, and the modified grid impedance model at 4 GHz for the TE incidence.

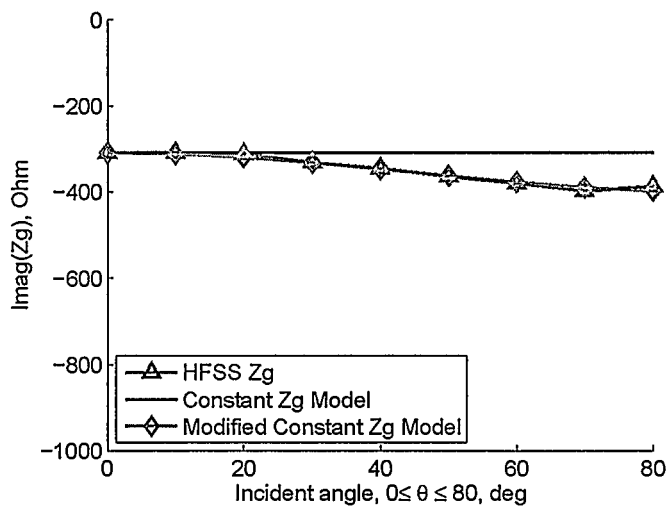


Figure 4.25: Patch AIS grid impedance comparison between the HFSS simulation, the constant grid impedance model, and the modified grid impedance model at 5.5 GHz for the TE incidence.

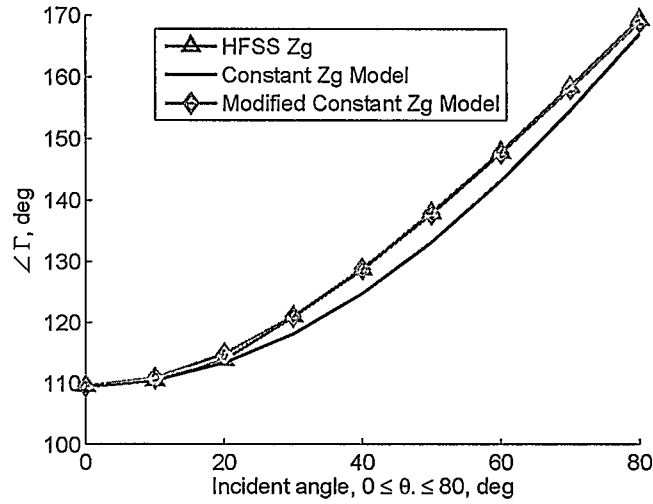


Figure 4.26: Patch AIS reflection phase comparison between the HFSS simulation, the constant grid impedance model, and the modified grid impedance model at 5.5 GHz for the TE incidence.

for TE and TM incident waves, respectively. Since Equation (4.37) is obtained empirically for the patch AIS with dimensions shown in Figures 3.12 and 4.2, it is interesting to see if it applies for patch AIS of different dimensions. Here, grid impedance of three other patch AIS are obtained using Equations (4.37) and (4.38) and compared with HFSS simulation results.

For comparison, the resonant frequency of these three patch AIS is set at 7.7 GHz. Since AIS with thin AIS are more desirable for low-profile antenna applications, the patch size, gap between patches and the dielectric thickness of these patch AIS are chosen as: 1) 6.3 mm X 6.3 mm, 1.4 mm and 2.45 mm; 2) 6.6 mm X 6.6 mm, 0.9 mm and 1.95 mm; 3) 6.9 mm X 6.9 mm, 0.2 mm and 1.26 mm. Each patch AIS is tested at 4 GHz, 5.5 GHz and 7.7 GHz. Comparison results are shown in Figures 4.27 to 4.35. The maximum Z_g^{Error} of the modified model is also shown in Tables 4.4 to 4.6 for these three patch AIS. Here, Z_g^{Error} is defined as,

$$Z_g^{Error}(\theta) = \left| \frac{Z_g^{HFSS}(\theta) - Z_g^{Model}(\theta)}{Z_g^{HFSS}(\theta)} \right|, \quad (4.39)$$

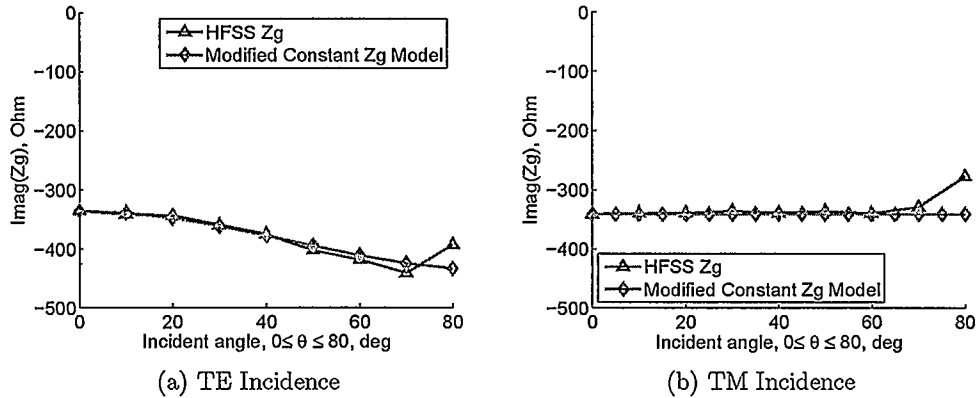


Figure 4.27: $Z_g(\theta)$ comparison of modified constant grid impedance model with HFSS simulation results as benchmark for a patch AIS at 4 GHz. The dimensions of the single patch is 6.3 mm X 6.3 mm.

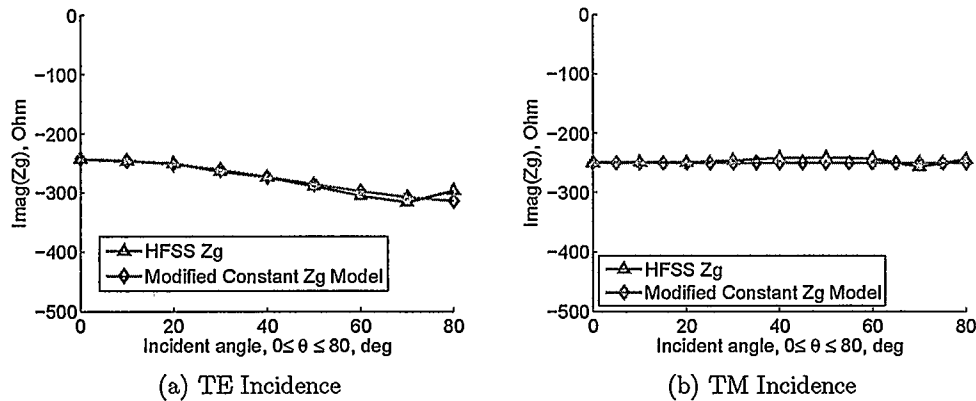


Figure 4.28: $Z_g(\theta)$ comparison of modified constant grid impedance model with HFSS simulation results as benchmark for a patch AIS at 5.5 GHz. The dimensions of the single patch is 6.3 mm X 6.3 mm.

where $Z_g^{HFSS}(\theta)$ is the grid impedance value obtained from HFSS simulations, and $Z_g^{Model}(\theta)$ is obtained from the modified constant grid impedance model as in Equations (4.37) and (4.38).

Observing the comparison results, it is quite clear that Equations (4.37) and (4.38), obtained from a particular patch AIS, can be used to approximate the grid impedance of patch AIS with different patch sizes quite well. This provides us with some insights in predicting the grid impedance behavior of patch AIS.

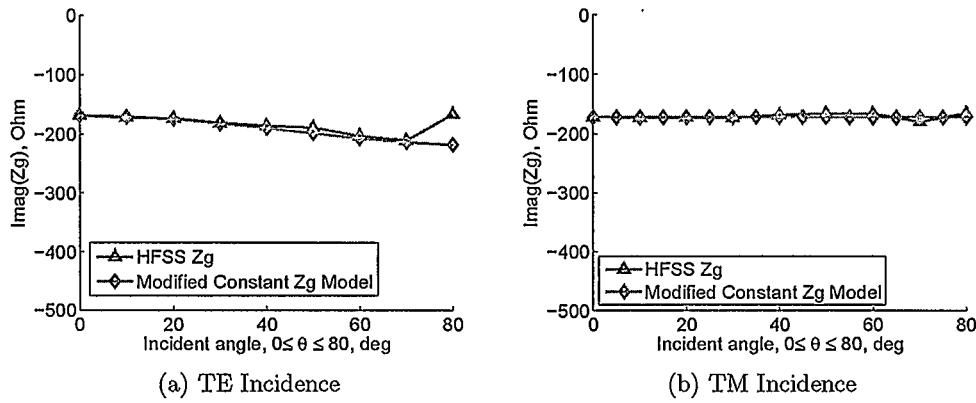


Figure 4.29: $Z_g(\theta)$ comparison of modified constant grid impedance model with HFSS simulation results as benchmark for a patch AIS at 7.7 GHz. The dimensions of the single patch is 6.3 mm X 6.3 mm.

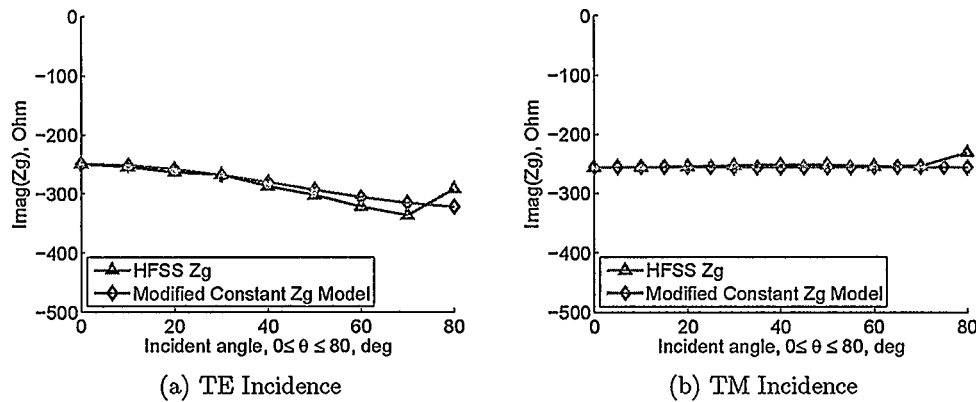


Figure 4.30: $Z_g(\theta)$ comparison of modified constant grid impedance model with HFSS simulation results as benchmark for a patch AIS at 4 GHz. The dimensions of the single patch is 6.6 mm X 6.6 mm.

Table 4.4: Comparing the Modified Z_g Model and the HFSS simulation results (Maximum Z_g^{Error} over incident angles for the Patch AIS with 6.3 mm patch size)

Maximum Z_g^{Error}	4GHz	5.5GHz	7.7GHz
TE mode	3.72%	2.83%	5.07%
TM mode	3.7%	3.42%	4.37%

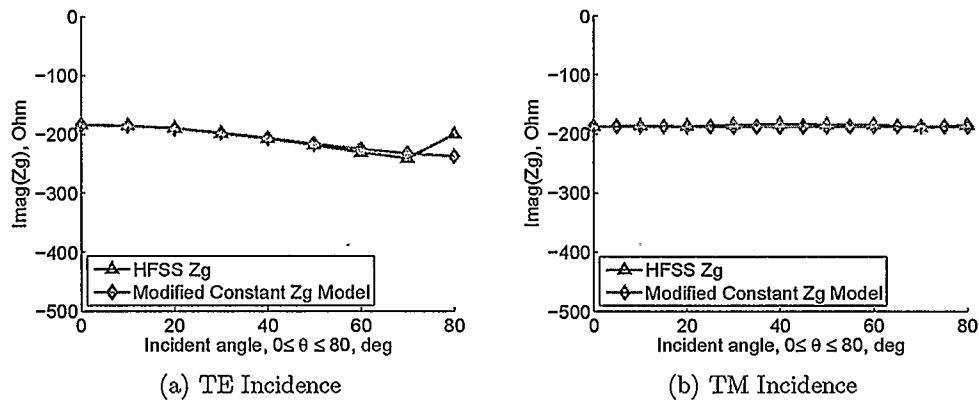


Figure 4.31: $Z_g(\theta)$ comparison of modified constant grid impedance model with HFSS simulation results as benchmark for a patch AIS at 5.5 GHz. The dimensions of the single patch is 6.6 mm X 6.6 mm.

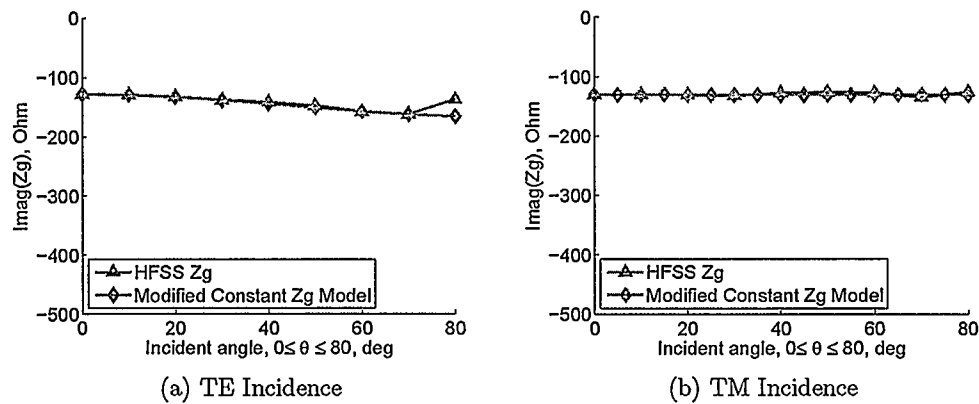


Figure 4.32: $Z_g(\theta)$ comparison of modified constant grid impedance model with HFSS simulation results as benchmark for a patch AIS at 7.7 GHz. The dimensions of the single patch is 6.6 mm X 6.6 mm.

Table 4.5: Comparing the Modified Z_g Model and the HFSS simulation results (Maximum Z_g^{Error} over incident angles for the Patch AIS with 6.6 mm patch size)

Maximum Z_g^{Error}	4GHz	5.5GHz	7.7GHz
TE mode	6.17%	3.79%	2.21%
TM mode	1.86%	2.25%	3.25%

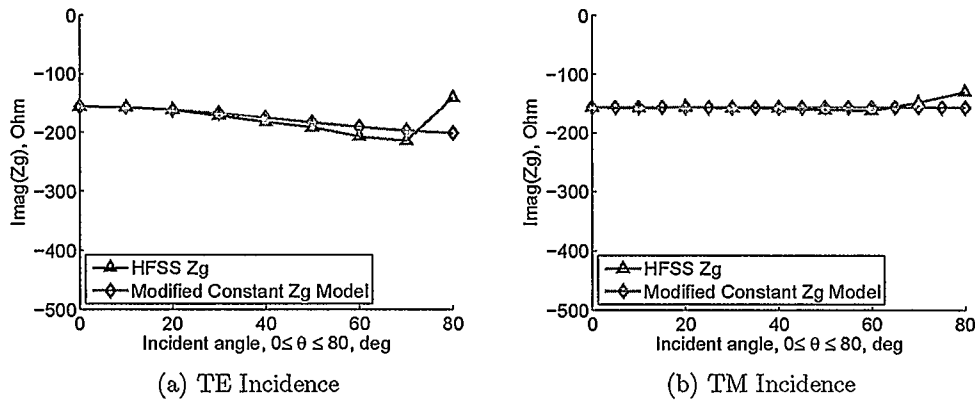


Figure 4.33: $Z_g(\theta)$ comparison of modified constant grid impedance model with HFSS simulation results as benchmark for a patch AIS at 4 GHz. The dimensions of the single patch is 6.9 mm X 6.9 mm.

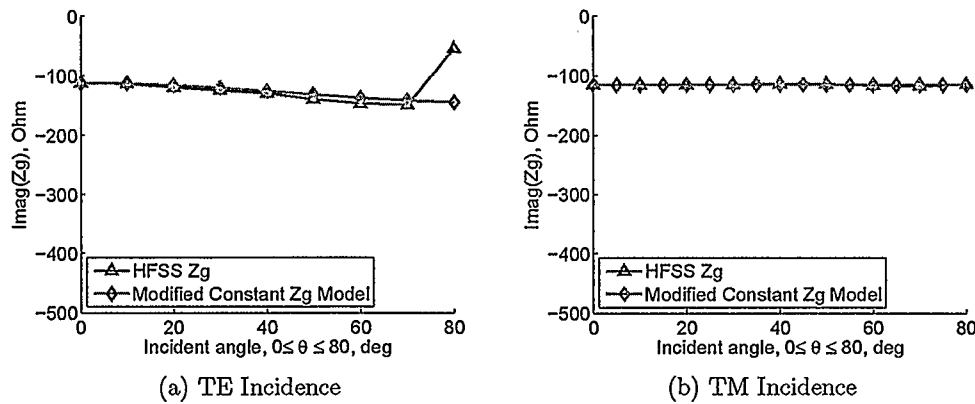


Figure 4.34: $Z_g(\theta)$ comparison of modified constant grid impedance model with HFSS simulation results as benchmark for a patch AIS at 5.5 GHz. The dimensions of the single patch is 6.9 mm X 6.9 mm.

Table 4.6: Comparing the Modified Z_g Model and the HFSS simulation results (Maximum Z_g^{Error} over incident angles for the Patch AIS with 6.9 mm patch size)

Maximum Z_g^{Error}	4GHz	5.5GHz	7.7GHz
TE mode	8.29%	6.5%	5.72%
TM mode	5.70%	1.9%	7.93%

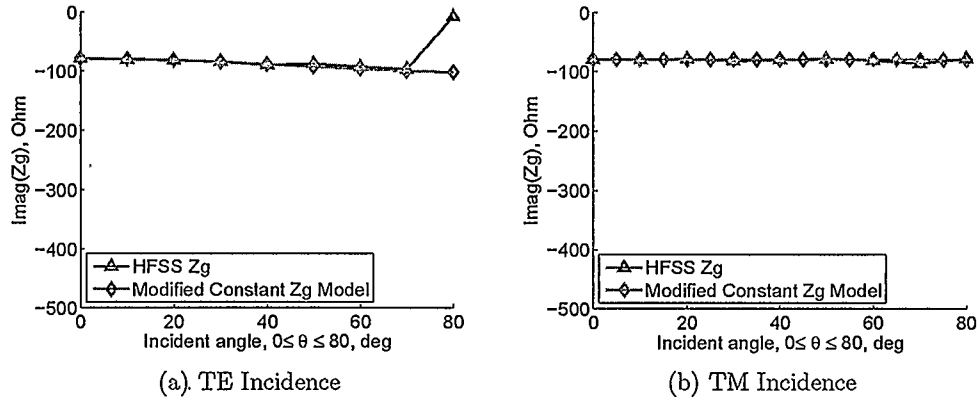


Figure 4.35: $Z_g(\theta)$ comparison of modified constant grid impedance model with HFSS simulation results as benchmark for a patch AIS at 7.7 GHz. The dimensions of the single patch is 6.9 mm X 6.9 mm.

4.5 Summary

In this chapter, a circuit model and a constant grid impedance model were introduced for more efficient computations of the reflection coefficients of the AIS structures for use in the far-field model discussed in Chapter 3. It has been shown that the reflection coefficients calculated from the circuit model and the constant grid impedance model are quite accurate at frequencies below the resonant frequency of a patch and a Jerusalem cross AIS. At the AIS resonant frequency, reflection coefficients of the Jerusalem cross AIS can still be computed accurately. However, an error was found in the calculated $\Gamma^{TE}(\theta)$ of the patch AIS at this frequency.

To analyze this error in the computed $\Gamma^{TE}(\theta)$ for the patch AIS, the accuracy of both the constant grid impedance model and the circuit model were discussed in detail. It was shown that the circuit model requires an extremely accurate grid impedance model near the AIS resonant frequency for accurate $\Gamma^{TE}(\theta)$ computation. On the other hand, grid impedance errors are more tolerable for the $\Gamma^{TE}(\theta)$ calculation below the resonant frequency or for the $\Gamma^{TM}(\theta)$ calculation at frequencies below and at the AIS resonant frequency.

While the constant grid impedance model is reasonably accurate for the Jerusalem cross AIS, a more accurate grid impedance model is required to calculate $\Gamma^{TE}(\theta)$ for the patch AIS at its resonant frequency (7.7 GHz). As a result, the constant grid impedance model was modified for TE incident waves for the patch AIS through a curve fitting technique at 7.7 GHz. This modified constant grid impedance model was verified at 4 GHz as well as 5.5 GHz for the patch AIS and results showed that this model is quite accurate at these test frequencies. It was also found that grid impedance obtained from this modified constant grid impedance model was quite accurate for patch AIS with different patch sizes as well, leading to a broader application of this modified model.

Chapter 5

Conclusion and Future Work

5.1 Conclusion and Thesis Contribution

In this thesis, a far-field model of a Hertzian dipole antenna above an Artificial Impedance Surface (AIS) was developed using a transmitting and a receiving method. With this model, it was clear that far-field patterns of the dipole can be directly computed from TE and TM plane wave reflection coefficients of the AIS structure. This way, one of the most important radiation properties of a Hertzian dipole over an AIS was related with the plane wave reflection properties of the AIS. In order to verify the far-field model, H- and E-plane patterns of the dipole over a patch and a Jerusalem cross AIS were calculated from the far-field model using accurate reflection coefficients, $\Gamma^{TE}(\theta)$ and $\Gamma^{TM}(\theta)$. These were obtained from the full-wave simulator, Ansoft HFSS. The results were compared with simulation results from another commercial full-wave simulator, FEKO. It was shown that, with accurate reflection coefficients, the calculated patterns of the Hertzian dipole were quite accurate in the frequency range of interest, at and below the resonant frequency of the AIS structure.

To shorten computation time even more, a circuit model and a constant grid impedance model were used to approximate the reflection coefficients for the far-field model. Results showed that, as a simple first-order approximation, the constant grid impedance model is quite accurate in predicting the grid impedance and reflection coefficients as functions of incident angle for the patch and the Jerusalem cross AIS. Compared to the $\cos^2 \theta$ grid impedance model introduced in [26], the constant grid impedance model is simpler but more accurate. However, due to sensitivity of the circuit model, a more accurate grid impedance model is required for $\Gamma^{TE}(\theta)$ calculation of the patch AIS near its resonant frequency.

Therefore, the constant grid impedance model was modified at the resonant frequency of the patch AIS through a curve fitting technique. It was shown that this modified grid impedance model approximates the grid impedance and reflection coefficients of the patch AIS quite accurately at all frequencies. It was also shown that this modified constant grid impedance model provides accurate approximation for grid impedances of patch AIS with different patch sizes.

The thesis contribution is divided into two parts: the developing of the far-field model and investigating the constant grid impedance model. The contribution in the first part, developing the far-field model, is summarized as follows.

- Applying the transmitting and receiving methods to analyze antenna's far-fields above an AIS structure is novel. Our work suggests that the receiving method is a simple but accurate way for analyzing far-fields of more complicated antennas above an AIS.
- The simple model equations, obtained from analytical derivation, clearly illustrate the relationship between the dipole's far-field patterns and the plane wave reflection coefficients of the AIS, which was not clear before this work.
- The far-field model is simple yet accurate, for AIS structures with periodicity small compared to free space wavelength. It has been shown that it is more accurate than other models proposed in the literature [3, 22].
- Since obtaining plane wave reflection coefficients in full-wave simulators is much faster than obtaining far-field patterns, our model makes antenna design above a complicated AIS structure much more efficient than before.

The contribution in investigating the grid impedance model is given here.

- The constant grid impedance model is investigated for the AIS structure, and it is found that, as a first-order approximation, the constant grid impedance model can be used along with the circuit model to compute AIS reflection coefficients with good accuracy. This

makes the computation of reflection coefficients of the AIS, and hence the computation of the far-field patterns much faster.

- The detailed circuit model analysis suggests that for accurate reflection coefficients computation, the grid impedance model only needs to be extremely accurate at the AIS resonant frequency for the TE incident waves. This not only leads to our modified grid impedance model, but also provides grid impedance models with a lower accuracy bound for accurate reflection coefficient calculation.
- The constant grid impedance model is modified such that reflection coefficients of the AIS can be computed accurately at all frequencies, including the AIS resonant frequency.

5.2 Future Work

Since Artificial Impedance Surfaces are complicated structures, it is difficult to fully understand how antennas interact with these structures, especially when the antenna and the AIS are in close proximity. The work in this thesis only provides a first step in understanding the properties of an antenna above an AIS. Much more work needs to be done. In this section, possible future work is discussed.

In Chapter 3, a far-field model was derived for a Hertzian dipole antenna over an AIS. As discussed, a couple simplifications were made in the derivation. Firstly, a Hertzian dipole, or an infinitesimal dipole was used. Since the dipole is infinitely small, its current will not be changed by any waves reflected by the periodic surface of the AIS. Thus, in the model analysis, only the primary reflected waves were considered while all the higher-order evanescent modes were ignored. For a real dipole, this will not be the case. For example, the current on a half-wave length dipole will be influenced by propagating or evanescent waves reflected by the AIS. As a result, higher-order modes and transmission lines corresponding to these modes should be taken into consideration. Secondly, an infinite AIS was considered in the derivation, which makes the derivation much simpler than using a finite AIS. This is

because surface waves will not be radiated and influence far-field patterns of an antenna on an infinite AIS. On a finite AIS, however, surface waves will radiate and change the far-field patterns. Therefore, more surface wave analysis is needed for a finite AIS structure as an antenna reflector.

In Chapter 4, a constant grid impedance model was used and modified for accurate computation of the reflection coefficient. By obtaining grid impedances, $Z_g(\theta)$, of patch and Jerusalem cross AIS from HFSS full-waves simulation, it was found that the $Z_g^{TM}(\theta)$ of the patch AIS, and $Z_g^{TE}(\theta)$ and $Z_g^{TM}(\theta)$ of the Jerusalem cross AIS are almost constant over the incident angle while $Z_g^{TE}(\theta)$ of the patch AIS is a function of $Z_g(0)$, the grid impedance at normal incidence, and the trig function $\sin^2 \theta$. However, the reasons for these phenomena are not clear yet. In [32], it was suggested that the grid impedance of an AIS is related to the current patterns on the center element of the periodic metal surface of the AIS. Observing the current patterns on the center patch and Jerusalem cross in the AIS when incident by a TE and a TM plane wave, it is clear that the currents on the patch vary more with the incident angle than those on the Jerusalem cross. It is suspected that this is because the Jerusalem cross has less metal area than the patch, confining the currents on the Jerusalem cross to a smaller area. However, it is still not clear why currents induced by a TE and a TM plane wave are different on a patch AIS. Moreover, the modified grid impedance model found through the curve fitting technique at 7.7 GHz for one certain patch AIS, (6mm X 6mm patch, 1mm gap between patches), also works well for patch AIS with different patch sizes. These phenomena will be interesting to investigate in the future.

Bibliography

- [1] C. Simovski, P. Maagt, S. Tretyakov, M. Paquay, and A. Sochava, "Angular stabilisation of resonant frequency of artificial magnetic conductors for TE-incidence," *Electronics Letters*, vol. 40, pp. 92–93, January 2004.
- [2] L. Akhoondzadeh-Asl, P. Hall, J. Nourinia, and C. Ghobadi, "Influence of angular stability of EBG structures on low profile dipole antenna performance," *IEEE International Workshop on Antenna Technology Small Antennas and Novel Material, 2006*, pp. 253–256, March 2006.
- [3] C. Tretyakov and C. Simovski, "Wire antennas near artificial impedance surface," *Microwave and Optical Technology Letters*, vol. 27, no. 1, pp. 46–50, October 2000.
- [4] C. Lewis, "Emerging trends in medical device technology: Home is where the heart monitor is," *FDA Consumer magazine, U.S. Food and Drug Administration*, May-June 2001.
- [5] R. Collin, *Field Theory of Guided Waves, 2nd ed.* IEEE Press, New York, 1991.
- [6] F. Zucker, *Antenna Theory, Part2, Chapter 21.* McGraw-Hill Book Company, 1969.
- [7] D. Sievenpiper, L. Zhang, R. Jimenez, N. Alexopolous, and E. Yablonovitch, "High-impedance electromagnetic surfaces with a forbidden frequency band," *IEEE Transactions on Microwave Theory and Techniques*, vol. 47, no. 11, pp. 2059–2074, November 1999.
- [8] F. Yang and Y. Rahmat-Samii, "A low-profile circularly polarized curl antenna over an electromagnetic bandgap (EBG) surface," *Microwave and Optical Technology Letters*, vol. 31, no. 4, pp. 264–267, November 2001.

- [9] M. Rahman and M. Stuchly, "Circularly polarized patch antenna with periodic structure," *IEE Proceeding on Microwave Antennas and Propagation*, vol. 149, no. 3, pp. 141–146, June 2002.
- [10] J. Vardaxoglou, A. Eresidis, and G. Goussetis, "Recent advances on ebg and amc surfaces with applications in terminal and high gain antennas," *7th International Conference on Telecommunications in Modern Satellite, Cable and Broadcasting Services, 2005*, vol. 1, pp. 3–6, September 2005.
- [11] W. McKinzie and R. Fahr, "A low profile polarization diversity antenna built on an artificial magnetic conductor," *IEEE Antennas and Propagation Society International Symposium, 2002*, vol. 1, pp. 762–765, June 2002.
- [12] S. Rogers, J. Marsh, W. Mckinzie, and J. Scott, "An AMC-based 802.11ab antenna for laptop computers," *IEEE Antennas and Propagation Society International Symposium, 2003*, vol. 2, pp. 10–13, June 2003.
- [13] R. J. Broas, D. Sivenpiper, and E. Yablonovitch, "A high-impedance ground plane applied to a cellphone handset geometry," *IEEE Transactions on Microwave Theory and Techniques*, vol. 49, no. 7, pp. 1262–1265, July 2001.
- [14] F. Tavakkol-Hamedani, L. Shafai, and G. Rafi, "Comparison of PBG and Perfect Magnetic Conductor surface effects on the performance of finite microstrip antennas," *IEEE Antennas and Propagation Society International Symposium, 2002.*, vol. 3, pp. 748–751, June 2002.
- [15] R. Coccioli, F. Yang, K. Ma, and T. Itoh, "Aperture-coupled patch antenna on UC-PBG substrate," *IEEE Transactions on Microwave Theory and Techniques*, vol. 47, no. 11, pp. 2123–2130, November 1999.

- [16] Y. Zhang, J. Hagen, and W. Wiesbeck, "Patch array as artificial magnetic conductors for antenna gain improvement," *Microwave and optical technology letters*, vol. 35, no. 3, pp. 172–175, November 2002.
- [17] Y. Zhang, J. Hagen, M. Younis, C. Fischer, and W. Wiesbeck, "Planar artificial magnetic conductors and patch antennas," *IEEE Transactions on Antennas and Propagations*, vol. 51, no. 10, pp. 2704–2711, October 2003.
- [18] S. Rogers, W. Mckinzie, and G. Mendolia, "An AMC-based 802.11ab antenna for laptop computers," *IEEE International Antennas and Propagation Symposium, 2003*, vol. 2, pp. 411–414, June 2003.
- [19] A. Feresidis, G. Goussetis, S. Wang, and J. Vardaxoglou, "Artificial magnetic conductor surfaces and their application to low-profile high-gain planar," *IEEE Transactions on Antennas and Propagations*, vol. 53, no. 1, pp. 209–214, January 2005.
- [20] A. Monorchio, S. Genovesi, U. Serra, and G. Manara, "Optimal design of artificial magnetic conductors including angular response," *IEEE Antennas and Propagation Society International Symposium.*, pp. 1931–1934, July 2006.
- [21] D. V. Labek, D. Gerard, B. Guizal, and F. Baida, "An angle-independent frequency selective surface in the optical range," *Optics Express*, vol. 14, no. 25, pp. 11 945–11 951, December 2006.
- [22] R. Hansen, "Effects of a high-impedance screen on a dipole antenna," *IEEE Antenna and Wireless Propagation Letters*, vol. 1, pp. 46–49, 2002.
- [23] S. Tretyakov and C. Simovski, "Dynamic model of artificial reactive impedance surfaces," *Journal of Electromagnetic Waves and Application*, vol. 17, no. 1, pp. 131–145, 2003.

- [24] D. Sievenpiper, "High impedance electromagnetic surface," Ph.D. thesis, University of California, Los Angeles, Los Angeles, CA, 1999.
- [25] H. Mosallaei and K. Sarabandi, "Antenna miniaturization and bandwidth enhancement using a reactive impedance substrate," *IEEE Transaction on Antennas and Propagation*, vol. 52, no. 9, pp. 2403–2414, September 2004.
- [26] C. Simovski, P. Maagt, and I. Melchakova, "High-impedance surfaces having stable resonance with respect to polarization and incidence angle," *IEEE Transactions on Antennas and Propagation*, vol. 53, no. 3, pp. 908–914, March 2005.
- [27] T. Zhao, D. Jackson, J. Williams, and A. Oliner, "General formulas for 2-D leaky-wave antennas," *IEEE Transaction on Antennas and Propagation*, vol. 53, pp. 3525–3533, 11 2005.
- [28] C. Balanis, *Antenna Theory, Analysis, and Design*. John Wiley and Sons, New York, 1997.
- [29] R. Harrington, *Time-Harmonic Electromagnetic Fields*. IEEE Press, John Wiley and Sons, 2001.
- [30] A. Aminian, F. Yang, and Y. Rahmat-Samii, "In-phase reflection and em wave suppression characteristics of electromagnetic band gap ground planes," *IEEE Antennas and Propagation Society International Symposium, 2003*, vol. 4, pp. 430–433, June 2003.
- [31] D. Kern, M. Wilhelm, D. Werner, and P. Werner, "A novel design technique for ultra-thin tunable EBG AMC surface," *IEEE Antennas and Propagation Society International Symposium, 2004*, vol. 2, pp. 1167–1170, June 2004.
- [32] B. Munk, *Frequency Selective Surfaces, Theory and Design*. John Wiley and Sons, New York, 2000.

- [33] F. Yang, K. Ma, Y. Qian, and T. Itoh, "A novel TEM waveguide using uniplanar compact photonic-bandgap (UC-PBG) structure," *IEEE Transactions on Microwave Theory and Techniques*, vol. 47, no. 11, pp. 2092–2097, November 1999.
- [34] S. Barbagallo, A. Monorchio, and G. Manara, "Frequency selective surfaces with reduced periodicity and enhanced bandwidth performance, journal =."
- [35] I. Lindell, *Methods for Electromagnetic Field Analysis*. IEEE Press, New York, 1995.
- [36] N. Marcuvitz, *Waveguide Handbook*. London, U.K.: Peter Peregrinus, 1986.
- [37] A. Hessel, *Antenna Theory, Part 2, Chapter 19, Appendix*. McGraw-Hill Book Company, 1969.
- [38] C. Balanis, *Advanced Engineering Electromagnetics*. John Wiley and Sons, New York, 1989.
- [39] J. Kraus, *Antennas, 2nd edition*. McGraw Hill Companies, 1988.
- [40] R. Remski, "Analysis of photonic bandgap structure using Ansoft HFSS," *Microwave Journal*, September 2000.
- [41] I. Bardi and Z. Cendes, "New directions in HFSS for designing microwave devices," *Microwave Journal*, August 1998.
- [42] A. Taflove and S. Hagness, *Computational Electrodynamics: The Finite-Difference Time-Domain Method, 3rd ed.* Norwood, MA: Artech House, 2005.
- [43] B. Guru and H. Hiziroglu, *Electromagnetic Field Theory Fundamentals*. China Machine Press, 2008.
- [44] R. Adams, *Calculus, 3rd edition*. Addison-Wesley Publishers Limited, 1995.

Appendix A

The Steepest Decent Method

The method of steepest decent, or the saddle point method, is used to evaluate the integral of the form,

$$I(\beta) = \int_P F(w)e^{\beta f(w)} dw, \quad (\text{A.1})$$

where β is large, positive and real; $f(w)$ is an analytic function; P is the path of integration in the complex w plane as shown in Figure A.1.

The philosophy of the steepest descent method is that, after contour deformation, a new path is chosen such that only a small segment of the path attributes most of contributions to the integral. This way, the integrand in equation (A.1) can be approximated by a simpler function over the important parts of the path. This new path is referred to as the steepest descent path, shown in Figure (A.1). If a pole is encountered during deformation, residues must be added. Thus, equation (A.1) can be written as a combination of the steepest descent part and the residue part.

$$I(\beta) = I_{SDP} + I_{residue}. \quad (\text{A.2})$$

The key to solve for the steepest descent part, I_{SDP} , is to find the steepest descent path. The steepest descent path passes through the saddle point of $f(w)$. A saddle point is neither a maximum nor minimum. To find the saddle point of $f(w)$, write the analytical function $f(w)$ as

$$f(w) = U(w) + jV(w) \quad (\text{A.3})$$

with $U(\xi, \eta)$ and $V(\xi, \eta)$ being real functions. The first-order saddle points w_s can be obtained by solving

$$\left. \frac{f(w)}{dw} \right|_{w=w_s} \equiv f'(w_s) = 0 \quad f''(w_s) \neq 0. \quad (\text{A.4})$$

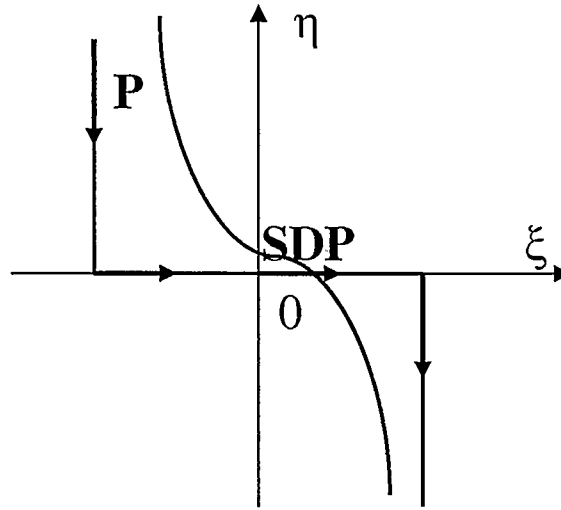


Figure A.1: The original path (P) and steepest decent path (SDP).

Thus, at the saddle point w_s , the following properties can be obtained

$$\frac{\partial U}{\partial \xi} = \frac{\partial V}{\partial \eta} = \frac{\partial U}{\partial \eta} = \frac{\partial V}{\partial \xi}, \quad (\text{A.5})$$

and

$$\frac{\partial^2 U}{\partial \xi^2} = -\frac{\partial^2 U}{\partial \eta^2} \quad \frac{\partial^2 V}{\partial \eta^2} = -\frac{\partial^2 V}{\partial \xi^2}. \quad (\text{A.6})$$

By observing Equations (A.5) and (A.6), at w_s , either $U(\xi, \eta)$ moves the most rapidly while $V(\xi, \eta)$ remains constant. Since β is real and positive, the exponential $\exp \beta U(\xi, \eta)$ will decrease rapidly with distance from the saddle point and only a small portion of the integration path, including the saddle point, will make any significant contributions to the values of the entire integral.

The steepest decent path is found forming a function,

$$f(w) = f(w_s) - s^2, \quad (\text{A.7})$$

where w_s is the saddle point and s is real ($-\infty \leq s \leq \infty$). Using Equation (A.7), we can write,

$$U(w) = U(w_s) - s^2, \quad V(w) = V(w_s). \quad (\text{A.8})$$

Since $V(w_s)$ remains a constant while $U(w_s)$ attains maximum at the saddle point w_s and decrease for other w , Equations (A.8) describes the path of the steepest decent.

Expanding $f(w)$ by a truncated Taylor series at the saddle point,

$$f(w) \approx f(w_s) + \frac{1}{2}(w - w_s)^2 f''(w_s), \quad (\text{A.9})$$

with the assumption that the higher derivatives of $f(w)$ at w_s are negligible, I_{SDP} in Equation (A.1) can be written as,

$$I_{SDP} = \int_{SDP} F(w) e^{\beta f(w)} dw \approx e^{\beta f(w_s)} \int_{SDP} F(w) e^{(\beta/2)(w-w_s)^2 f''(w_s)} dw, \quad (\text{A.10})$$

Assuming that $F(w)$ is a slow varying function in the neighbourhood of the saddle point, Equation (A.10) can be simplified to,

$$I_{SDP} \approx \sqrt{\frac{2\pi}{-\beta f''(w_s)}} F(w_s) e^{\beta f(w_s)}. \quad (\text{A.11})$$

where $f''(w_s)$ is the second-derivative of $f(w)$ at the saddle point w_s .